



1. Report No. NASA CR-120981	2. Government Accession No.	3. Recipient's Catalog No.	
4. Title and Subtitle EXPERIMENTAL QUIET ENGINE PROGRAM AERODYNAMIC PERFORMANCE OF FAN C		5. Report Date August 1972	6. Performing Organization Code
		8. Performing Organization Report No.	
7. Author(s) Giffin, R.G., Parker, D.E., and Dunbar, L.W.		10. Work Unit No.	
9. Performing Organization Name and Address General Electric Company Aircraft Engine Group Cincinnati, Ohio 45215		11. Contract or Grant No. NAS3-12430	
		13. Type of Report and Period Covered Contractor Report	
12. Sponsoring Agency Name and Address National Aeronautics and Space Administration Washington, D.C. 20546		14. Sponsoring Agency Code	
		15. Supplementary Notes Project Manager, E. W. Conrad, V/STOL & Noise Division NASA Lewis Research Center, Cleveland, Ohio	
16. Abstract  This report presents the aerodynamic component test results of Fan C, a high-bypass-ratio, low-aerodynamic-loading, 1550 feet per second (472.4 m/sec), single-stage fan, which was designed and tested as part of the NASA Experimental Quiet Engine Program. The fan was designed to deliver a bypass pressure ratio of 1.60 with an adiabatic efficiency of 84.2% at a total fan flow of 915 lb/sec (415.0 kg/sec). It was tested with and without inlet distortion. A bypass total-pressure ratio of 1.61 and an adiabatic efficiency of 83.9% at a total fan flow of 921 lb/sec (417.8 kg/sec) were actually achieved. An operating margin in excess of 14.6% was demonstrated at design speed.			
17. Key Words (Suggested by Author(s)) Fan, Compressor, Inlet Flow Distortion, Aerodynamic Performance		18. Distribution Statement Unclassified - Unlimited	
19. Security Classif. (of this report) Unclassified	20. Security Classif. (of this page) Unclassified	21. No. of Pages	22. Price* <del>92.00</del> 9.75

TABLE OF CONTENTS

<u>Section</u>	<u>Page</u>
1.0 SUMMARY	1
2.0 INTRODUCTION	2
3.0 DESCRIPTION OF TEST FAN	3
4.0 TEST SET-UP AND PROCEDURE	8
4.1 Test Facility	8
4.2 Overall Performance Instrumentation	8
4.3 Bypass Ratio Schedule	10
4.4 Vehicle Configuration for Test	10
5.0 RESULTS AND DISCUSSION	12
5.1 Presentation of Overall Results	12
5.2 Undistorted Flow Performance	12
5.2.1 Fan Bypass Region	12
5.2.2 Fan Core Performance	15
5.3 Distorted Flow Performance	30
6.0 SUMMARY OF RESULTS	39
7.0 REFERENCES	40
APPENDIX I - Instrumentation	41
APPENDIX II - Computation of Overall Fan Performance	47
APPENDIX III - Overall Performance Data for Builds 1 and 2	53
APPENDIX IV - Rotor Tip Pressure Patterns	89
APPENDIX V - Aeromechanical Characteristics of Fan C Based on Fan Component Testing	109
LIST OF SYMBOLS	145

Preceding page blank

## LIST OF ILLUSTRATIONS

Figure		Page
1	Fan C Component Test Vehicle Layout.	5
2	Full-Scale Compressor and Fan Test Facility.	9
3	Clean Inlet Flow Test Bypass Ratio Schedule.	11
4	Fan C Performance Characteristics in the Bypass Region.	13
5	Fan C Performance Characteristics in the Core Region.	14
6	Radial Efficiency Profile at Discharge.	17
7	Radial Profiles.	18
8	Radial Profiles.	19
9	Radial Profiles.	20
10	Variation of Element Properties with Throttling, Design Stream Function = 0.059 (Bypass OD).	21
11	Variation of Element Properties with Throttling, Design Stream Function = 0.303.	22
12	Variation of Element Properties with Throttling, Design Stream Function = 0.548.	23
13	Variation of Element Properties with Throttling, Design Stream Function = 0.787 (Bypass ID).	24
14	Variation of Element Properties with Throttling, Design Stream Function = 0.855 (Core OD).	25
15	Variation of Element Properties with Throttling, Design Stream Function = 0.885.	26
16	Variation of Element Properties with Throttling, Design Stream Function = 0.919.	27
17	Variation of Element Properties with Throttling, Design Stream Function = 0.953.	28
18	Variation of Element Properties with Throttling, Design Stream Function = 0.984 (Core ID).	29
19	Inlet Flow Distortion Level.	31
20	Tip Radial Distortion Inlet Pressure Profile.	32
21	Crosswind Distortion Pattern.	33
22	One/Rev Distortion Pattern.	34
23	Inlet Pressure Recovery Contour, Crosswind Distortion.	35
24	Fan C Performance Map, Tip Radial Inlet Distortion.	36

LIST OF ILLUSTRATIONS (Continued)

<u>Figure</u>		<u>Page</u>
25	Fan C Performance Map, Crosswind Inlet Distortion.	37
26	Fan C Performance Map, One/Rev Inlet Distortion.	38
27	Fan C Test Vehicle Instrumentation Location.	43
28	Inlet Boundary Layer Description.	44
29	Typical Inlet Duct Pressure Profiles.	49
30	Build 1 Bypass Performance Map.	54
31	Build 2 Bypass Performance Map.	55
32	Radial Efficiency Profile for Builds 1, 2, and 3 (Near Design Point).	58
33	Radial Efficiency Profile for Builds 1, 2, and 3 (Throttled Above Design Point).	59
34	Rotor Tip Wall Static Profile Vs. Speed for Build 1.	60
35	Rotor Tip Wall Static Profile Vs. Speed for Build 2.	61
36	Rotor Tip Wall Static Profile Vs. Speed for Build 3.	62
37	Traverse Radial Profiles, Radius Vs. Total Pressure Ratio (Bypass).	63
38	Traverse Radial Profiles, Radius Vs. Corrected Total Temperature Rise (Bypass).	64
39	Traverse Radial Profiles, Radius Vs. Adiabatic Efficiency (Bypass).	65
40	Traverse Radial Profiles, Radius Vs. Absolute Air Angle (Bypass).	66
41	Traverse Radial Profiles, Radius Vs. Relative Air Angle (Bypass).	67
42	Traverse Radial Profiles, Radius Vs. Total Pressure Ratio (Core).	68
43	Traverse Radial Profiles, Radius Vs. Corrected Total Temperature Rise (Core).	69
44	Traverse Radial Profiles, Radius Vs. Adiabatic Efficiency (Core).	70
45	Traverse Radial Profiles, Radius Vs. Absolute Air Angle (Core).	71
46	Bypass Ratio Excursion, Bypass Performance.	73
47	Bypass Ratio Excursion, Core Performance.	74

LIST OF ILLUSTRATIONS (Continued)

<u>Figure</u>		<u>Page</u>
48	Variation of Element Properties with Bypass Ratio, Design Stream Function = 0.059 (Bypass OD).	75
49	Variation of Element Properties with Bypass Ratio, Design Stream Function = 0.303.	76
50	Variation of Element Properties with Bypass Ratio, Design Stream Function = 0.548.	77
51	Variation of Element Properties with Bypass Ratio, Design Stream Function = 0.787 (Bypass ID).	78
52	Variation of Element Properties with Bypass Ratio, Design Stream Function = 0.855 (Core OD).	79
53	Variation of Element Properties with Bypass Ratio, Design Stream Function = 0.953.	80
54	Variation of Element Properties with Bypass Ratio, Design Stream Function = 0.984 (Core ID).	81
55	Effect of Bypass Ratio on Rotor Hub Total Pressure Profile.	83
56	Effect of Bypass Ratio on Splitter Wall Static Pressure.	84
57	Effects of OGV Setting Angle on Bypass Performance.	86
58	Comparison of OGV Loss Coefficient Between Builds 1 and 3.	87
59	Typical Data Record of Kulite Trace.	90
60	Readings Taken for Rotor Tip Static Pressure Contours.	91
61	Rotor Static Pressure Distribution.	92
62	Rotor Static Pressure Distribution.	93
63	Rotor Static Pressure Distribution.	94
64	Rotor Static Pressure Distribution.	95
65	Rotor Static Pressure Distribution.	96
66	Rotor Static Pressure Distribution.	97
67	Rotor Static Pressure Distribution.	98
68	Rotor Static Pressure Distribution.	99
69	Rotor Static Pressure Distribution.	100
70	Rotor Static Pressure Distribution.	101
71	Comparison of Build 1 and Build 3 Kulite Traces at 100% and 105% $N/\sqrt{\theta}$ .	106
72	Comparison of Build 1 and Build 3 Shock Swallowing Process as Speed Increases.	108

## LIST OF ILLUSTRATIONS (Concluded)

Figure		Page
73	Engine Gage Locations.	114
74	Mod. II Steady-State Stress Distribution at 5200 rpm.	115
75	Mod. II Blade Root Stress Distribution at 5200 rpm.	116
76	Mod. II Blade Scope Limits as a Function of Speed (First Three Modes).	119
77	Mod. II Typical Vibratory Response on the Operating Line with a Clean Inlet.	120
78	Mod. II Campbell Diagram.	122
79	Inlet Distortion Magnitudes.	124
80	Campbell Diagram and Scope Limits, Bypass OGV.	130
81	Campbell Diagram and Scope Limits, Forward Inner OGV.	131
82	Campbell Diagram and Scope Limits, Aft Inner OGV.	132
83	Bypass OGV Strain Gage Location.	133
84	Forward Inner OGV Strain Gage Location.	134
85	Aft Inner OGV Strain Gage Location.	135
86	Goodman Diagram for Scope Limit Calculations.	136
87	Bypass Stator Vane Vibration Summary with Clean Inlet.	137
88	Forward Inner Stator Vane Vibration Summary with Clean Inlet.	139
89	Aft Inner Stator Vane Vibration Summary with Clean Inlet.	140

## 1.0 SUMMARY

This report presents the aerodynamic component test results of Fan C, a high-bypass-ratio, low-aerodynamic-loading, 1550 feet per second (472.4 m/sec), single-stage fan, which was designed and tested as part of the NASA Experimental Quiet Engine Program. The fan was tested with an undistorted inlet flow and with circumferential, tip radial, and crosswind distortions. The hub-tip radius ratio was 0.36 at rotor inlet. A flow splitter, immediately downstream of the rotor, separates the fan bypass flow from the fan core flow. An axial distance equal to two rotor chords was employed between the rotor and bypass portion outlet guide vanes (OGV). The vane-number-to-blade-number ratio was 2.3. No inlet guide vanes were employed.

The fan was designed to deliver a bypass total-pressure ratio of 1.60 at a total fan flow of 915 lb/sec (415.0 kg/sec). The design bypass adiabatic efficiency was 84.2%. A bypass portion total-pressure ratio of 1.61 and an adiabatic efficiency of 83.9% at a flow of 921 lb/sec (417.8 kg/sec) were actually achieved. The peak design speed adiabatic efficiency was 85.0% which occurred at a bypass pressure ratio of 1.68 and a total fan flow of 911 lb/sec (413.2 kg/sec). The fan core region was designed to develop a total-pressure ratio of 1.49 at a flow of 152.8 lb/sec (69.3 kg/sec). A fan core portion pressure ratio of 1.54 was actually achieved at its design flow. At this condition, a fan core adiabatic efficiency of 82.3% was measured.

The operational limit line was determined up to 95% corrected speed. Rotating stall was the operational limit at 50% corrected speed. At all corrected speeds from 60 to 95%, high rotor stress was the limit that precluded further increases in back pressure. The facility power limit was reached at 100% corrected speed prior to reaching the operational limit line. At this speed, the facility power limit point corresponded to an operating margin of 14.6% relative to the design operating line at altitude-cruise conditions. At 90% corrected speed, the operating margin was 17.4% relative to the design operating line at sea-level-static conditions.

The fan was tested with one-per-rev circumferential, tip radial, and crosswind distortion screens installed. At 90% corrected speed, the screens were found to produce approximately 15% distortion (maximum minus minimum pressure divided by maximum pressure). The fan demonstrated minimal operating margin loss to all three distortions tested except for the 70% corrected speed region with the tip radial pattern.

1

## 2.0 INTRODUCTION

In the last 20 years, the rapid growth of the commercial aviation industry has demanded large increases in aircraft size and flight frequency. This, coupled with the increased public awareness of the noise pollution problem, has prompted the initiation of an Experimental Quiet Engine Program by the NASA-Lewis Research Center (Contract NAS3-12430). The major objectives of this program are: the demonstration of noise levels produced by turbofan engines which are designed for low noise output and confirmation that predicted noise reduction can be achieved; demonstration of the technology and design innovations which will reduce the production and radiation of noise in high-bypass turbofan engines; and acquisition of experimental acoustic and aerodynamic data for turbofan engines, which are designed for low noise output, to give a basis for correction of acoustic theory and experiment, and to give a better understanding of the noise production mechanisms in fans, compressors, turbines, and nozzles.

Observations of past trends indicate that as tip speed increases, at constant aerodynamic loading, fan broadband noise increases. Also, at constant tip speed, a reduction in aerodynamic loading is observed to decrease fan pure tone noise. Hence, for given mission requirements, the minimum fan noise configuration requires consideration of the weighted sum of the two types of noise. In order to confirm acoustic noise predictions and to acquire acoustic and aerodynamic data for typical high-bypass fans, two low-speed fans, designated Fan A and Fan B, and one low-aerodynamic-loading fan, designated Fan C, were designed.

The aerodynamic performance of the three fans has been determined in the General Electric Large Fan Test Facility in Lynn, Massachusetts. Upon completion of the aerodynamic testing, each fan, in turn, is to be tested in the NASA-Lewis Acoustic Test Facility.

Fan A, one of the low-speed fans, and the low-aerodynamic-loading Fan C are to be mated with a TF39/CF6 engine core. The complete full-scale high-bypass fan engines will then be tested at the General Electric Remote Test Site at Peebles, Ohio, to determine their overall aeroacoustic performance as well as thrust and specific fuel consumption.

This report presents the aerodynamic component test results on Fan C with uniform inlet flow and with tip radial, crosswind, and one-per-rev circumferential distortion of the inlet flow. Details of the design of Fan C, and the other fans evaluated in this test series, are given in Reference 1. The aerodynamic component test results of Fan B and Fan A are given in References 2 and 3, respectively.

### 3.0 DESCRIPTION OF TEST FAN

The aerodynamic design point for this low-aerodynamic-loading fan was selected at the altitude cruise condition, a flight Mach number of 0.82 at an altitude of 36,000 feet (10.97 km). At this condition, the corrected tip speed is 1550 ft/sec (472.4 m/sec) with an average fan bypass total pressure ratio of 1.60 and an average fan core total pressure ratio of 1.49. The design corrected fan flow of 915 lb/sec (415.0 kg/sec), with a hub tip radius ratio of 0.36 and a specific flow of 41.3 lb/sec/ft<sup>2</sup> (197.0 kg/sec/m<sup>2</sup>) of annulus area, results in a tip diameter of 68.30 inches (1.633 m). The design flow for the fan core, corrected to fan inlet, was 152.8 lb/sec (69.3 kg/sec) resulting in a bypass ratio of 5.0.

Figure 1 shows a meridional view of the Fan C component test vehicle. Immediately downstream of the rotor, a flow splitter is located which separates the fan bypass flow from the fan core flow. The axial distance between the rotor and bypass outlet guide vane (OGV), expressed in number of rotor chords, is a minimum of 2.0. The axial distance between the rotor and fan core OGV, expressed in number of rotor chords, is 1.25. No inlet guide vanes were incorporated in the configuration. The moderate aspect ratio (2.09) part-span shrouded rotor contained 26 blades. The rotor tip and hub solidities were 1.40 and 2.45, respectively. Sixty vanes were incorporated for both the outer and inner OGV's for a vane-number-to-blade-number ratio of 2.3.

The design rotor tip relative Mach number is 1.52. The rotor blade employs a profile shape that, according to past experience, would minimize excessive shock losses on the suction surface and still be compatible from a throat area and energy addition standpoint. The blade meanline shape and point of maximum thickness vary radially. The blade is similar to a double circular arc profile in the hub region. Profile shapes at other radii are generally similar in appearance to the NASA multiple-circular arc profiles.

The profile shapes for the bypass OGV, which operates at moderate conditions of inlet Mach number and diffusion factor, were designed with a modified NASA 65 series thickness distribution on a circular arc meanline. The fan core OGV, which operates in a relatively high inlet Mach number environment when considering the turning requirement and diffusion factor level, was a tandem vane row wherein the profile shapes were specifically tailored to minimize suction surface Mach numbers and, therefore, prevent shock losses and minimize diffusion losses.

Tabulated below are some of the pertinent Mach numbers and diffusion factors for the rotors and OGV's:

		<u>Outlet Guide Vanes</u>		
		<u>Rotor</u>	<u>Bypass</u>	<u>Core</u>
Inlet Mach Number	OD	1.52	0.67	0.72
	ID	0.80	0.67	0.83
Diffusion Factor	OD	0.324	0.410	0.403
	ID	0.454	0.350	0.520



PRECEDING PAGE BLANK NOT FILMED

Complete design details are presented in Reference 1.

The estimated average running rotor tip clearance at 100% speed was 0.015 inch (0.38 mm).

## 4.0 TEST SET-UP AND PROCEDURE

### 4.1 TEST FACILITY

Performance tests of this fan were conducted in General Electric's Large Fan Test Facility, at Lynn, Massachusetts. The general aspects of the test vehicle facility installation are shown in Figure 2. The test fan draws air vertically downward from the atmosphere through a throttling device, which is located at the top of the inlet stack. Testing for this fan was performed with an open-inlet throttle except for the high-power extraction points where the facility power became limiting. The air then passes through a cascade of turning vanes and proceeds horizontally to a foreign object damage (FOD) protection screen and accelerates through an area ratio 7.0 into the fan inlet. Downstream of the fan rotor, the flow is split into a fan bypass portion and a fan core portion. The bypass flow is ducted from the vehicle discharge through an adapter into the facility where the bypass discharge valve is located. This air is collected and exhausted vertically into the atmosphere. The fan core flow is ducted from the vehicle discharge through an adapter into the facility where the main discharge valve is located. This air is collected and passed through a pipe containing a flow measurement system and is finally discharged vertically into the atmosphere. Dial indicators are attached to each of the discharge valves to indicate the relative valve position; zero indicates fully closed and 100 indicates fully open.

Power to drive the test fan is provided by a steam turbine rated at 30,000 horsepower (22.4 Mw).

### 4.2 OVERALL PERFORMANCE INSTRUMENTATION

Overall fan performance was determined from measurement of fan inlet and fan discharge total temperatures and total pressures. At fan inlet, the total pressure was measured by four six-element rakes located in the cylindrical section of the inlet duct between the bellmouth and the fan inlet. Twenty-four thermocouples attached to the inlet FOD screen were used for determining inlet total temperatures. The pressure and temperature sensors were located approximately on centers of equal area. At fan discharge, the total temperature and total pressure were measured by circumferential arc rakes. Seven 12-element arc rakes were located behind the fan bypass OGV's, and five seven-element arc rakes were located behind the fan core OGV's. In the bypass, the elements were circumferentially spaced so as to span one OGV passage for the two outermost rakes and two OGV passages for the remainder. In the fan core, the elements were circumferentially spaced to span two OGV passages. Radially, the arc rakes were located on centers of equal design mass flow of the fan bypass and fan core, respectively. A more detailed description of this and the other vehicle instrumentation is contained in Appendix I.

# FULL SCALE COMPRESSOR & LARGE FAN TEST FACILITY

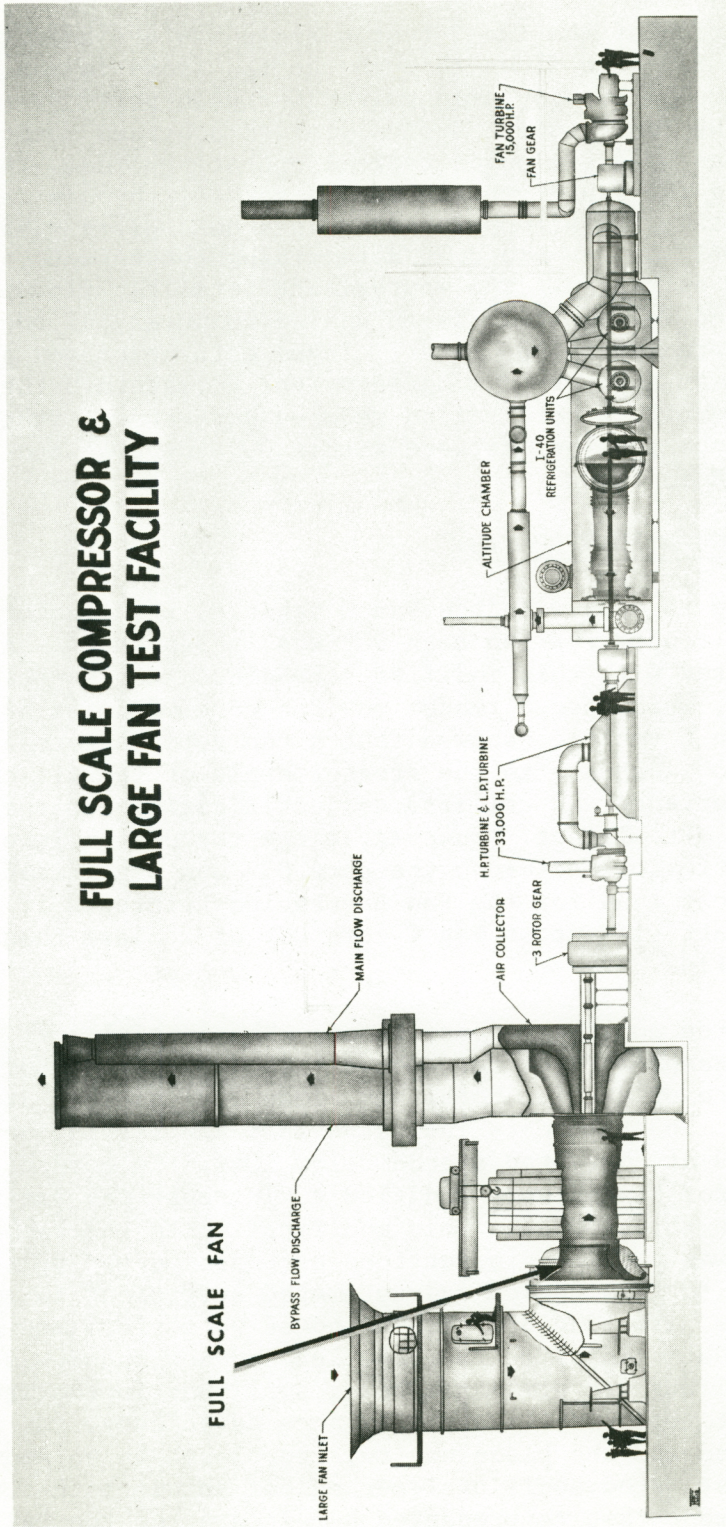


Figure 2. Full-Scale Compressor and Fan Test Facility.

#### 4.3 BYPASS RATIO SCHEDULE

The configuration of the Fan C test vehicle was designed to simulate the fan bypass and fan core flows through the fan frame region with independently controllable discharge valves for each portion. Cycle calculations for the Fan C engine system yielded a bypass ratio migration, as a function of fan speed, along a typical operating line. The procedure adopted for testing the Fan C vehicle was to set this bypass ratio, as a function of fan speed, for all operating points on a given speed line except those specific points aimed at determining the effects of bypass ratio swing on fan operation. The approximate total fan flow and fan core flow were calculated in real time by an analog computer and continuously displayed in the Data Recording Center. These data were used as a guide in setting the bypass and core discharge valves to maintain the desired bypass ratio. Generally, the detailed reduced data showed that the bypass ratios for the test points were within 0.2 count of the desired values, as is shown in Figure 3.

#### 4.4 VEHICLE CONFIGURATION FOR TEST

Prior to going to test with the Fan C vehicle, the stagger angle of the aft element of the tandem row fan core OGV was increased  $4^\circ$ . All Fan C testing was conducted with this modified schedule. Test experience on Fan B, Reference 2, which had a tandem row fan core OGV similar to that employed on the Fan C vehicle, showed that a fan core performance gain was achieved by a  $6^\circ$  increase to the stagger angle of the aft core OGV element. This experience was utilized as justification for the closure of the Fan C core OGV aft element. However, since the design level of inlet Mach number and diffusion factor on the core OGV was significantly lower for the Fan C vehicle than for the Fan B vehicle, Reference 1, a stagger angle adjustment to the aft element of Fan C core OGV of  $2^\circ$  less than for Fan B was believed justified.

There were three configurations tested. The initial test (Build 1) was as designed, except as indicated above. The testing on Build 1 revealed that the performance of the fan rotor was below expectations at corrected speeds below 104%. The test data indicated that the leading bow shock was not being swallowed at corrected speeds below 104%. To correct this apparent deficiency, the rotor blades were modified to increase the external compression and to increase the throat area. This modification to the camber line shape, known as Build 2, was confined to sections outboard of the part-span shroud since modification to this region was estimated sufficient to solve the performance problem. Testing of Build 2 showed no performance gain relative to Build 1. Test data indicated that the leading bow shock was moved aft relative to Build 1 but was still not being swallowed in the manner expected. In a second attempt to correct the performance deficiency, the part-span shrouds were removed and the blade was twisted closed by an amount slightly greater than the estimated additional mechanical untwist; this modification was Build 3. All test results presented herein are for the Build 3 configuration except as specifically noted.

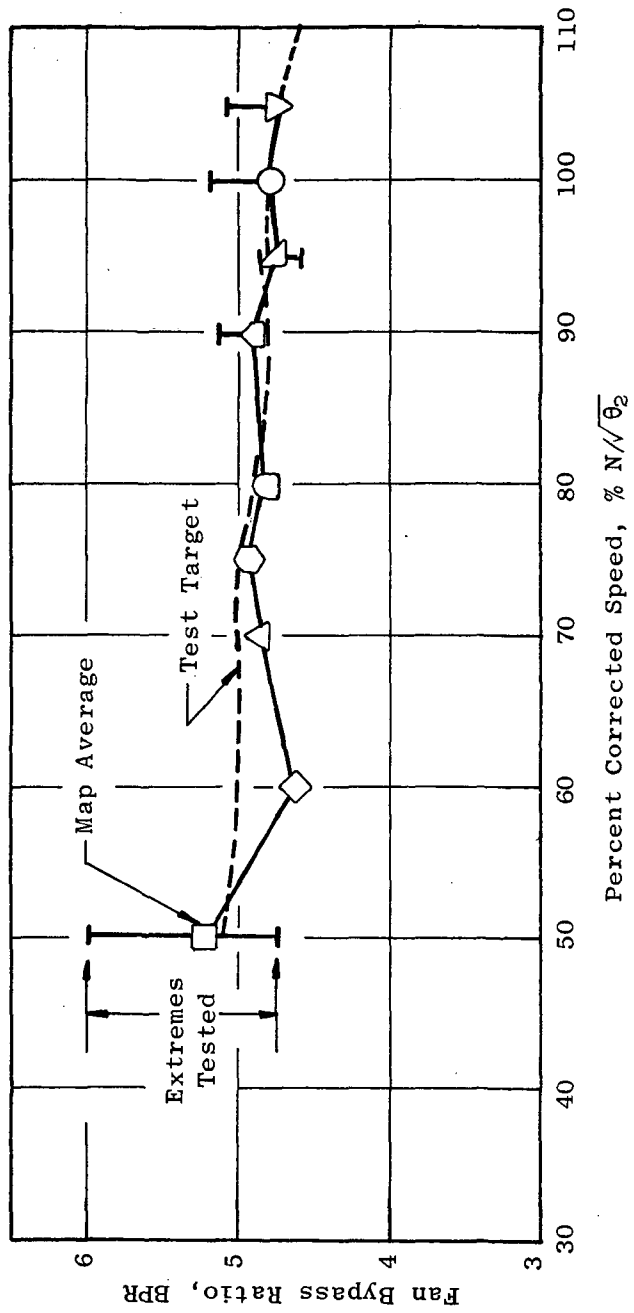


Figure 3. Clean Inlet Flow Test Bypass Ratio Schedule.

## 5.0 RESULTS AND DISCUSSION

### 5.1 PRESENTATION OF OVERALL RESULTS

The basic design of Fan C incorporates radial variations in discharge total pressure and total temperature. Additionally, deviations from design intent and the migration of the fan to other operating conditions will produce differing radial variations. Accurate cycle representation of the fan component requires recognition of these variations. Accordingly, the overall fan performance is presented in the form of two maps to distinguish the performance characteristics in the fan bypass and fan core regions. One map presents fan bypass total pressure ratio and efficiency versus total fan flow. The second map presents fan core total pressure ratio and efficiency versus fan core flow. The utilization of total fan flow, rather than bypass flow, on the bypass map is somewhat arbitrary but does serve the purpose of providing an overall maximum flow constraint, at a given speed, when these maps are incorporated into the cycle performance calculations.

Presentation of the fan performance by two separate maps tends to imply that the results are independent, as would be the case if the splitter between the bypass flow and fan core flow extended forward through the rotor. This is not the case for the configuration employed by Fan C; a definite performance interdependence exists between the two streams. Although it is an oversimplification, it is meaningful to consider the case where the leading edge of the flow splitter is located aft of a single OGV which spans the entire annulus. In such a case, the OGV discharge pressure is largely controlled by the bypass discharge valve by virtue of the high bypass ratio for the fan. At fixed bypass discharge valve settings, a change to the fan core discharge valve will directly affect its flow rate but not significantly affect the delivery pressure to the fan core flow. Also, at fixed fan core discharge valve setting, a change to the bypass discharge valve will affect the delivery pressure into the fan core duct and, thereby, also affects its flow rate. The actual configuration with the splitter behind the rotor is more complex than either of the two extremes because of the influence of the splitter on the operation of the core region and the off-incidence and loading conditions forced onto the OGV's. Accordingly, for each value of bypass ratio, a separate and distinct pair of performance maps will result. A series of test points were recorded to investigate the effects of off-design bypass ratio operation during the Build 2 testing. The results are presented in Appendix III along with the other Build 2 results.

### 5.2 UNDISTORTED FLOW PERFORMANCE

#### 5.2.1 Fan Bypass Region

The measured performance of the Fan C stage is shown in Figures 4 and 5. The measured flow at the design bypass pressure ratio of 1.60 was 922 lb/sec (418.2 kg/sec), which is 0.76% greater than the design value of

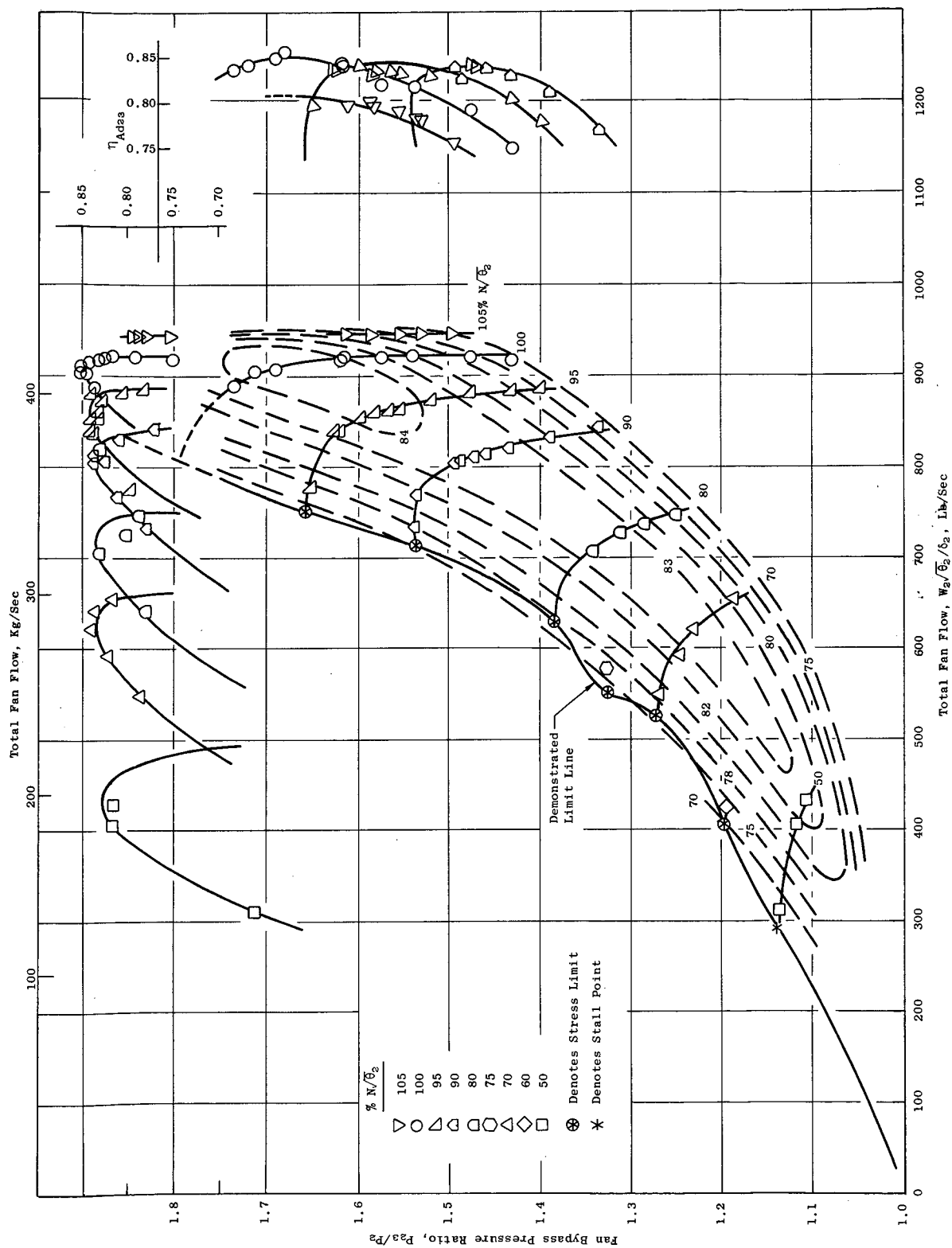


Figure 4. Fan C Performance Characteristics in the Bypass Region.

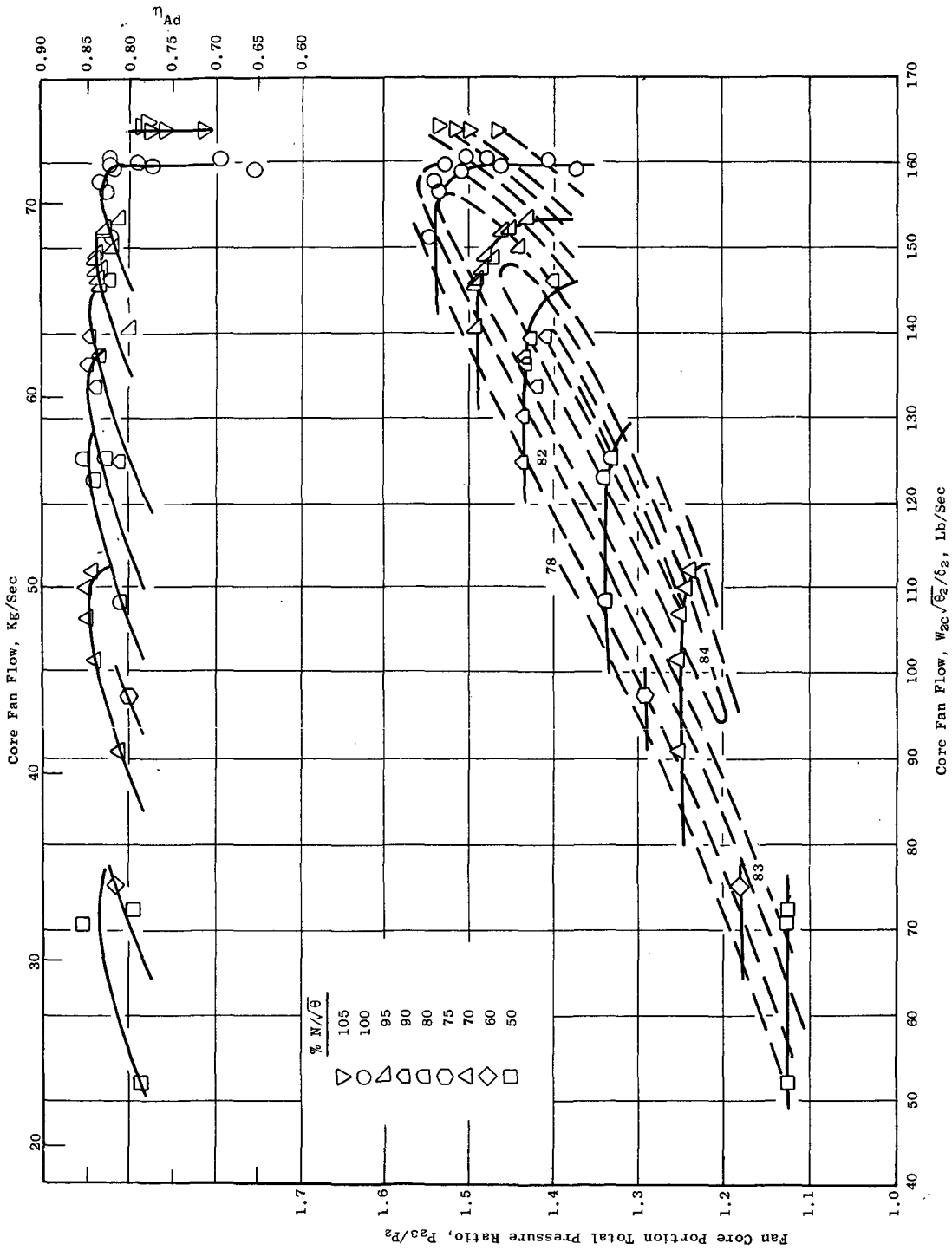


Figure 5. Fan C Performance Characteristics in the Core Region.

915 lb/sec (415.0 kg/sec). The bypass adiabatic efficiency was 83.7%, 0.5 point below objective value. The peak efficiency at design speed was 85.0% at a bypass pressure ratio of 1.68 and a total fan flow of 911 lb/sec (413.2 kg/sec). At 105% corrected speed, a flow of 946 lb/sec (429.1 kg/sec) was achieved, a specific flow of 42.7 lb/sec/ft<sup>2</sup> (208.0 kg/sec/m<sup>2</sup>) of annulus area.

The operational limit line was determined up to, and including, 95% corrected speed. Rotating stall was the operational limit at 50% corrected speed. At all corrected speeds from 60 to 95%, high rotor stress was the limit that precluded further increases in back pressure. The facility power limit was reached at 100% corrected speed prior to reaching the operational limit line. At this speed the facility power limit point corresponded to an operating margin of 14.6% relative to the design operating line at altitude cruise conditions. At 90% corrected speed, the operating margin was 17.4% relative to the design operating line at sea level static conditions.\*

### 5.2.2 Fan Core Performance

The fan was designed to deliver a core pressure ratio of 1.49 at a core flow of 152.8 lb/sec (69.3 kg/sec). The proper selection of the map point for comparison with the design objectives is less obvious for the fan core performance than for the bypass performance since the match point for the core depends upon the overall engine operating characteristics. Selecting the objective core flow at 100% corrected speed, a core pressure ratio of 1.54 was achieved. At this condition, the core adiabatic efficiency was 82.3%. A peak adiabatic efficiency of 84.5% was achieved in the 70 to 90% corrected-speed range.

The terminations of the constant speed lines on the low-flow side were arbitrarily made consistent with the average bypass ratio from Figure 3 and the total fan flow limit from the bypass map. These terminations do not represent an operating limit of the fan core portion map. Furthermore, since it was the intent to maintain a constant bypass ratio at each speed, a vertical bypass speed line results in a vertical fan core speed line. A vertical fan core speed line generated in this manner does not necessarily imply a choke condition in the core stream. The 100% corrected speed line deviates slightly from a "best data fit line" in an attempt to recognize the small variations in bypass ratio from point to point.

The measured design speed fan core adiabatic efficiency was 3.2 points below the design objective level of 85.5%. The moderately high rotor hub loading and the high fan core OGV inlet Mach number and loading are contributing factors. The relatively thick-blade hub profile section that was employed to alleviate a high stress region is also a consideration. For high-bypass-ratio fans in general, a significant portion of the fan core flow is what

$$* \text{ Operating margin} = \left[ \frac{\frac{W}{P_{23}} \text{ at operating line}}{\frac{W}{P_{23}} \text{ at stall}} - 1 \right] \times 100; \% \text{ at constant speed}$$

would normally be classified as the "end wall" flow from the fan blade. For the Fan C configuration, the height of fan core duct expressed as a ratio to the staggered spacing of the fan blade, a significant dimension when analyzing end wall flows, is 1.29. Figure 6 shows the radial efficiency profile at stage discharge as deduced from the discharge arc rake instrumentation. Shown on this figure is an assumed efficiency profile for a redesigned configuration without a splitter. Also shown are the locations of seven arc rakes used for the efficiency evaluation of this hypothetical fan. It is observed that the actual instrumentation density in the fan core tends to emphasize the low efficiency "end wall" flow relative to measurements of the more conventional hypothetical fan.

As a part of the data analysis performed on Fan C, the efficiency, total pressure and temperature, OGV total-pressure-loss, and static-pressure-rise coefficients were computed for each arc rake immersion as described in Appendix II. Radial plots of this information for three points at 100% corrected speed are shown in Figures 7 through 9. Referring to Figure 7, which shows build 3 data for a point near the operating line, the bypass stage efficiency is lower in the end wall region but higher in the free stream region than design. This is consistent with the General Electric design policy which does not design for the entire velocity drop-off which occurs deep within the end wall region but instead tends to distribute these losses across the span. The bypass OGV total-pressure-loss coefficient, related to the difference between rotor and stage efficiency, is relatively consistent with design intent except at the vane ends. It is believed that the larger than design losses at the outside diameter and inside diameter of the OGV are caused by the relatively thick boundary layer entering the vane row as a result of the larger than normal axial spacing between the rotor and OGV, approximately 21 inches (0.53 m). In the fan core region, the rotor exit total temperature profile shows that the design work input was modestly exceeded. The total pressure profile exceeds the design intent by a significant amount, indicating that the work input was accomplished more efficiently than expected. The core OGV total-pressure-loss coefficients are high in the vane end regions. Boundary layer growth along the wall in the 9-inch (0.29 m) axial spacing between the rotor and OGV's is a contributing factor. Also, as previously discussed, the instrumentation density tends to emphasize the low energy "end wall" flow.

The rotor and stage efficiency, OGV total-pressure-loss and static-pressure-rise coefficients are plotted against ideal throttle area for immersions 1, 3, 5, and 7 (which correspond to stream functions of 0.06, 0.30, 0.54, and 0.78, respectively) in the fan bypass and for each of the five immersions in the fan core (which correspond to stream functions of 0.86, 0.89, 0.92, 0.95 and 0.98) in Figures 10 through 18. The bypass throttle area on these figures is the nozzle throat area required to pass the bypass flow, assuming an isentropic expansion from measured discharge total pressure and total temperature, to ambient static pressure. For the bypass, the peak rotor efficiency and minimum OGV total-pressure-loss coefficient for each immersion occurs in the near vicinity of the design throttle area indicating that this portion of the fan is well matched

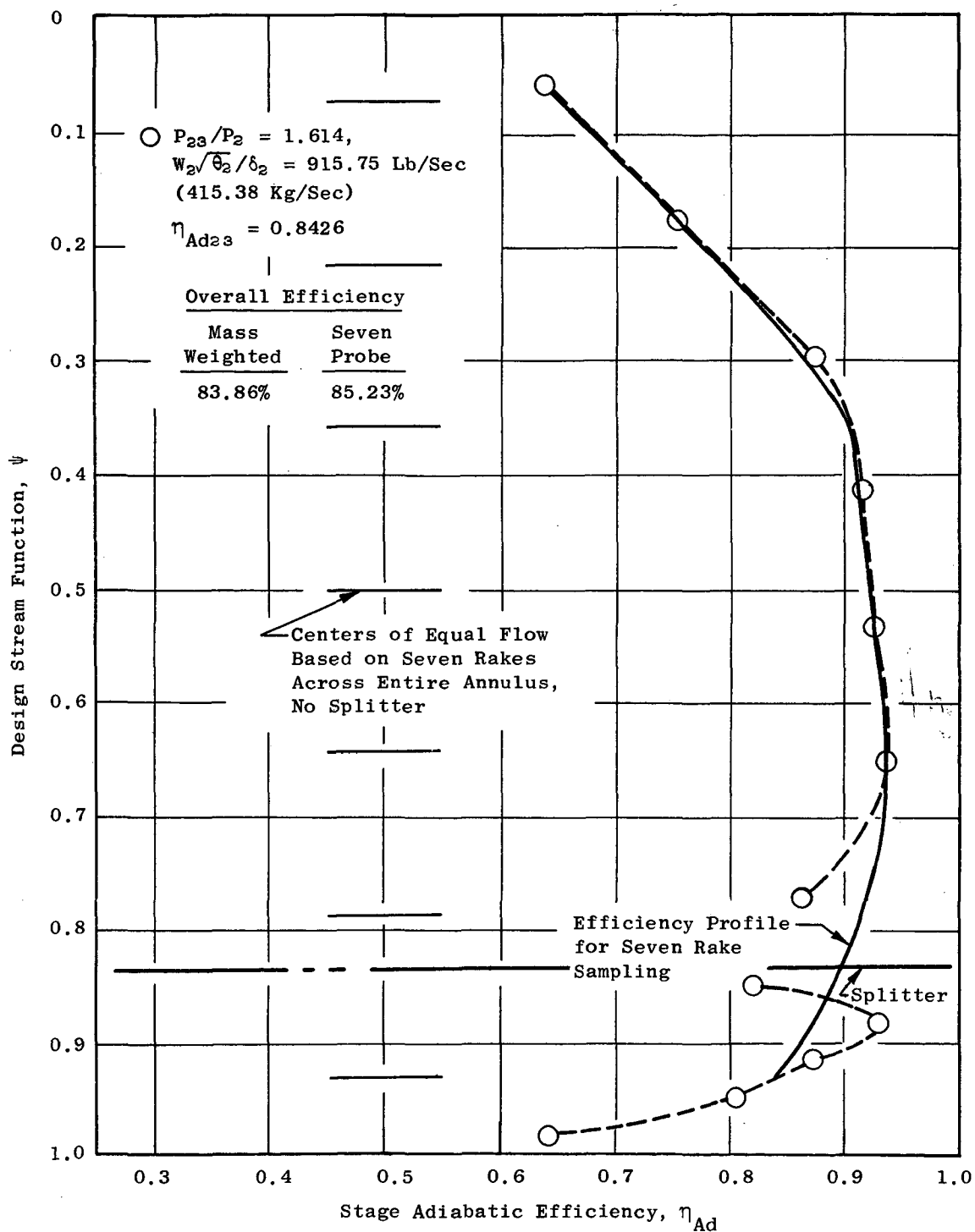


Figure 6. Radial Efficiency Profile at Discharge.

$\% N/\theta_2$  99.96,  $P_{23}/P_2$  1.614,  $P_{24}/P_2$  1.502,  $W_2/\theta_2/\delta_2$  915.75 Lb/Sec  
 $(415.38$  Kg/Sec),  $\eta_{Ad23}$  84.26 %,  $\eta_{Ad24}$  81.98 %

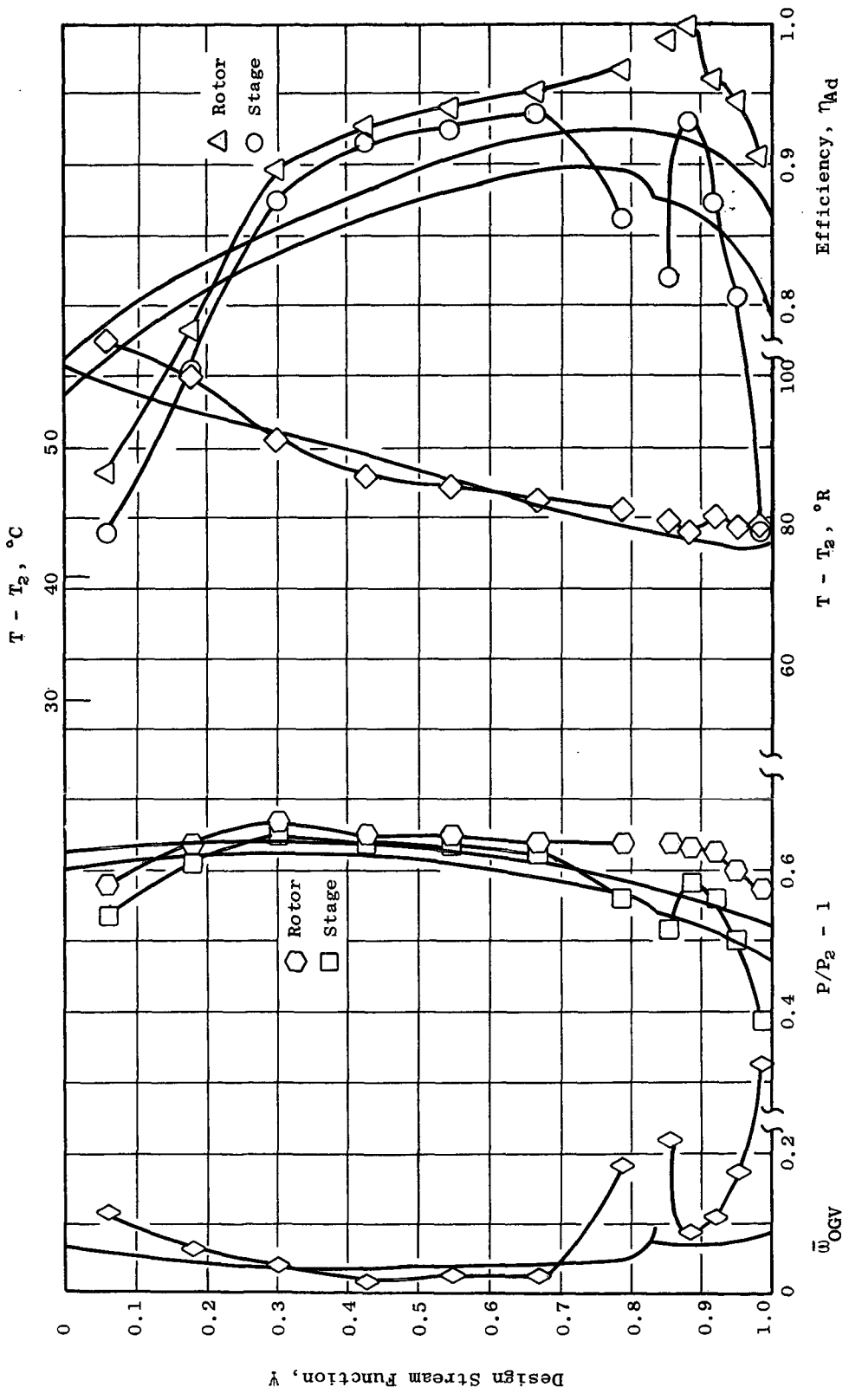


Figure 7. Radial Profiles.

$\% N/\sqrt{\theta_2} \underline{100.02}$ ,  $P_{23}/P_2 \underline{1.678}$ ,  $P_{24}/P_2 \underline{1.528}$ ,  $W_2/\sqrt{\theta_2}/\delta_2 \underline{910.45 \text{ Lb/Sec}}$   
 $(412.97 \text{ Kg/Sec})$ ,  $\eta_{Ad23} \underline{85.04 \%}$ ,  $\eta_{Ad24} \underline{81.95 \%}$

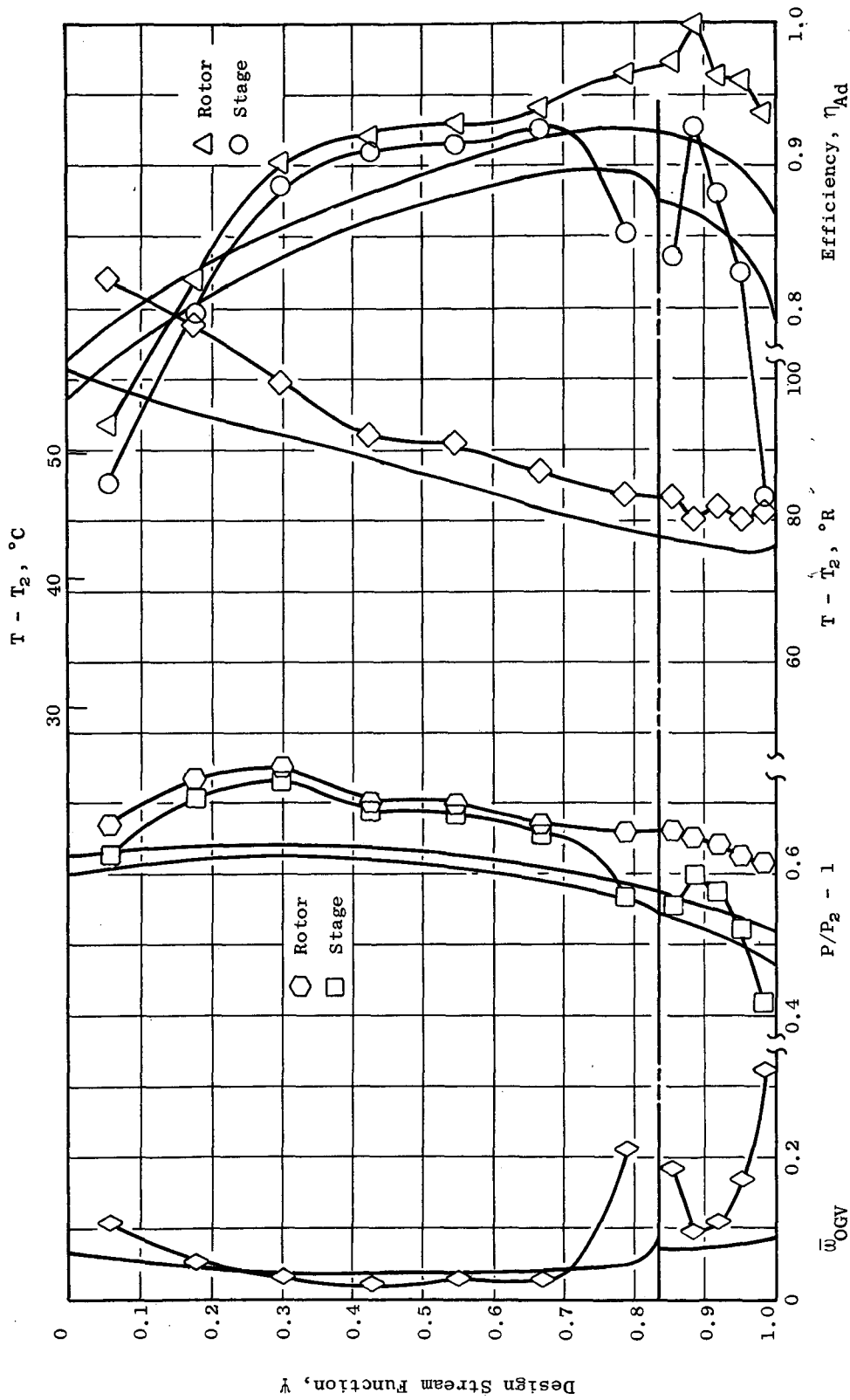


Figure 8. Radial Profiles.

$\% N/\theta_2$  99.97,  $P_{23}/P_2$  1.538,  $P_{24}/P_2$  1.462,  $W_2/\theta_2/b_2$  920.62 Lb/Sec  
 $(417.59$  Kg/Sec),  $\eta_{Ad_{23}}$  81.38 %,  $\eta_{Ad_{24}}$  76.89 %

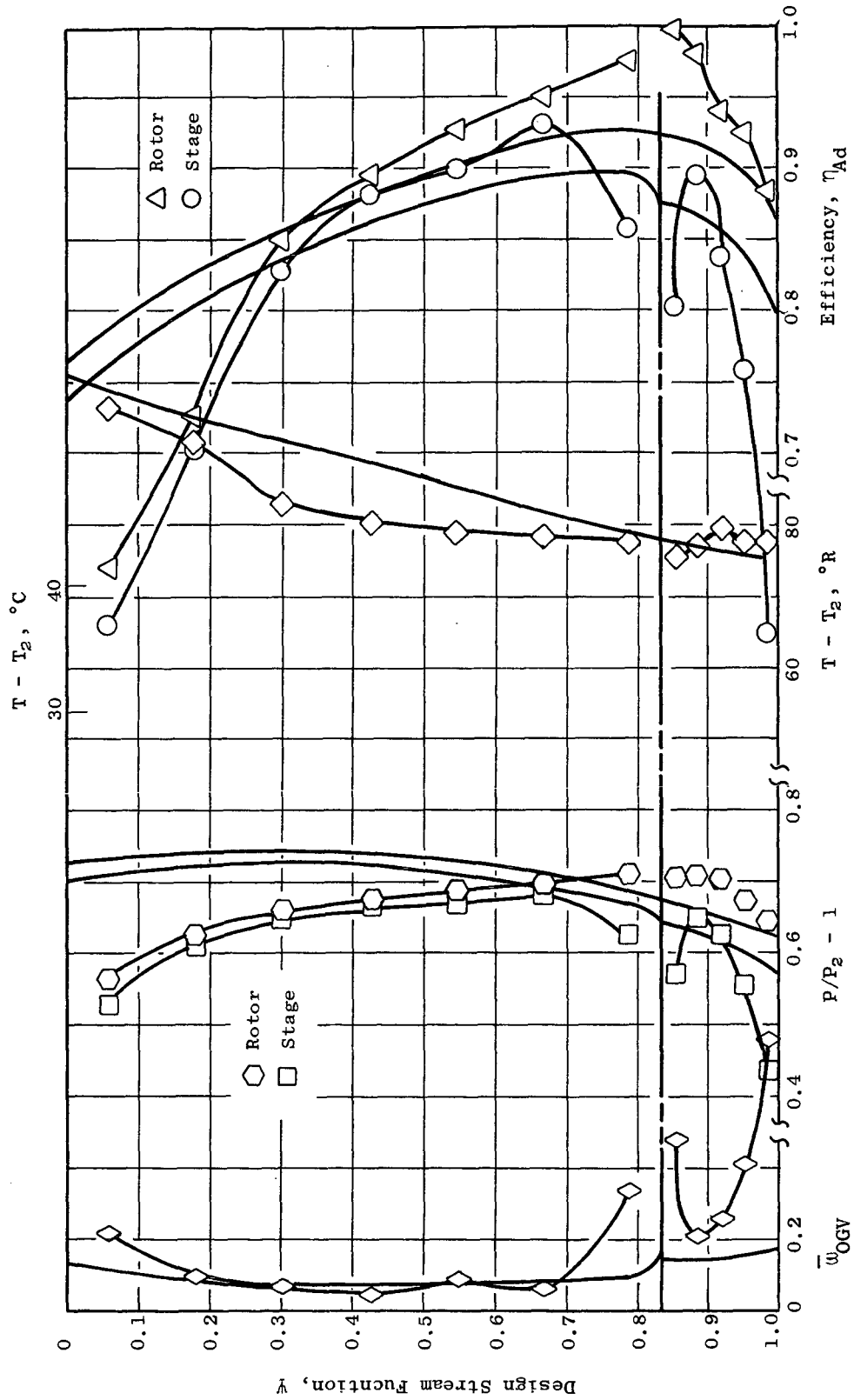


Figure 9. Radial Profiles.

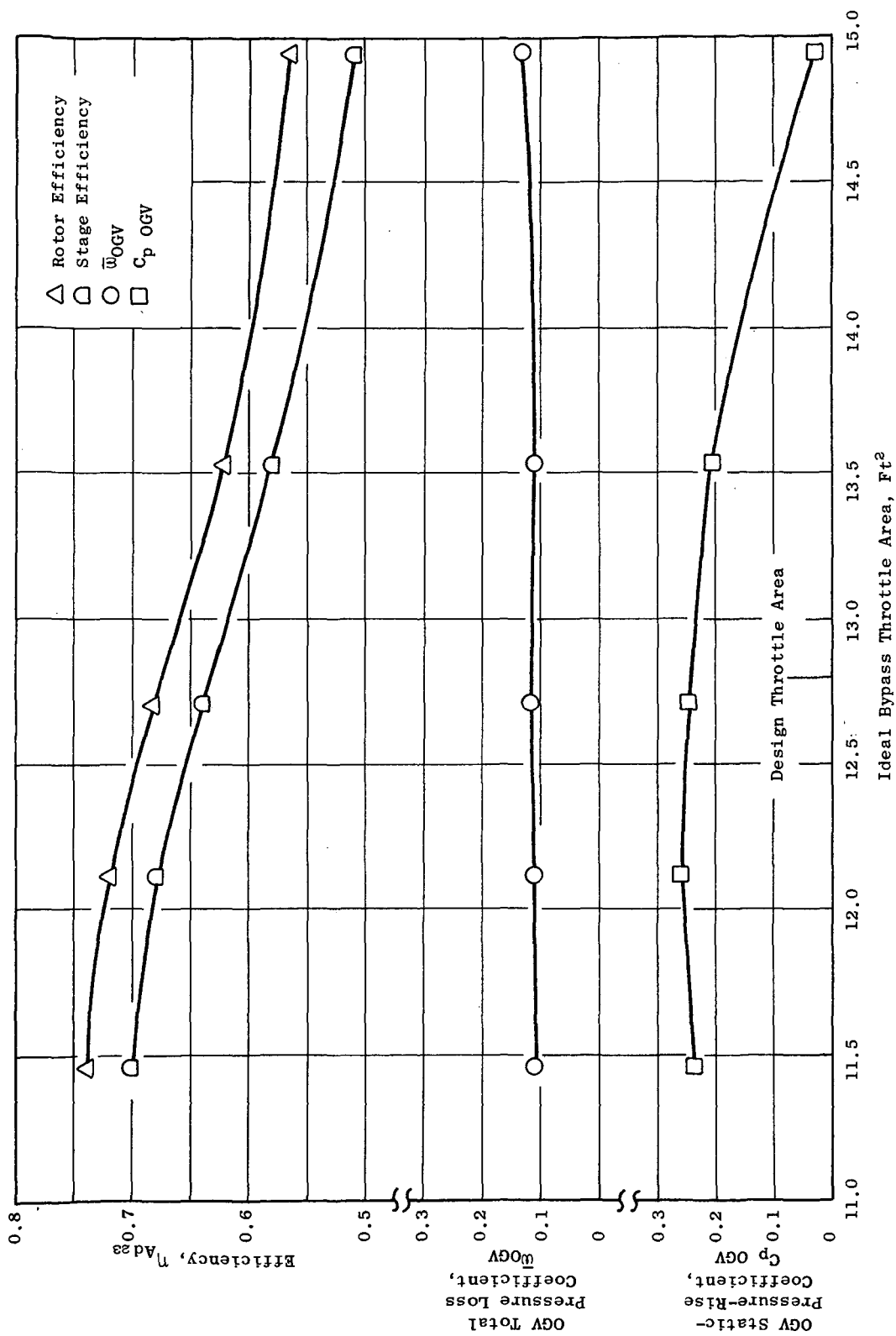


Figure 10. Variation of Element Properties with Throttling, Design Stream Function = 0.059 (Bypass OD).

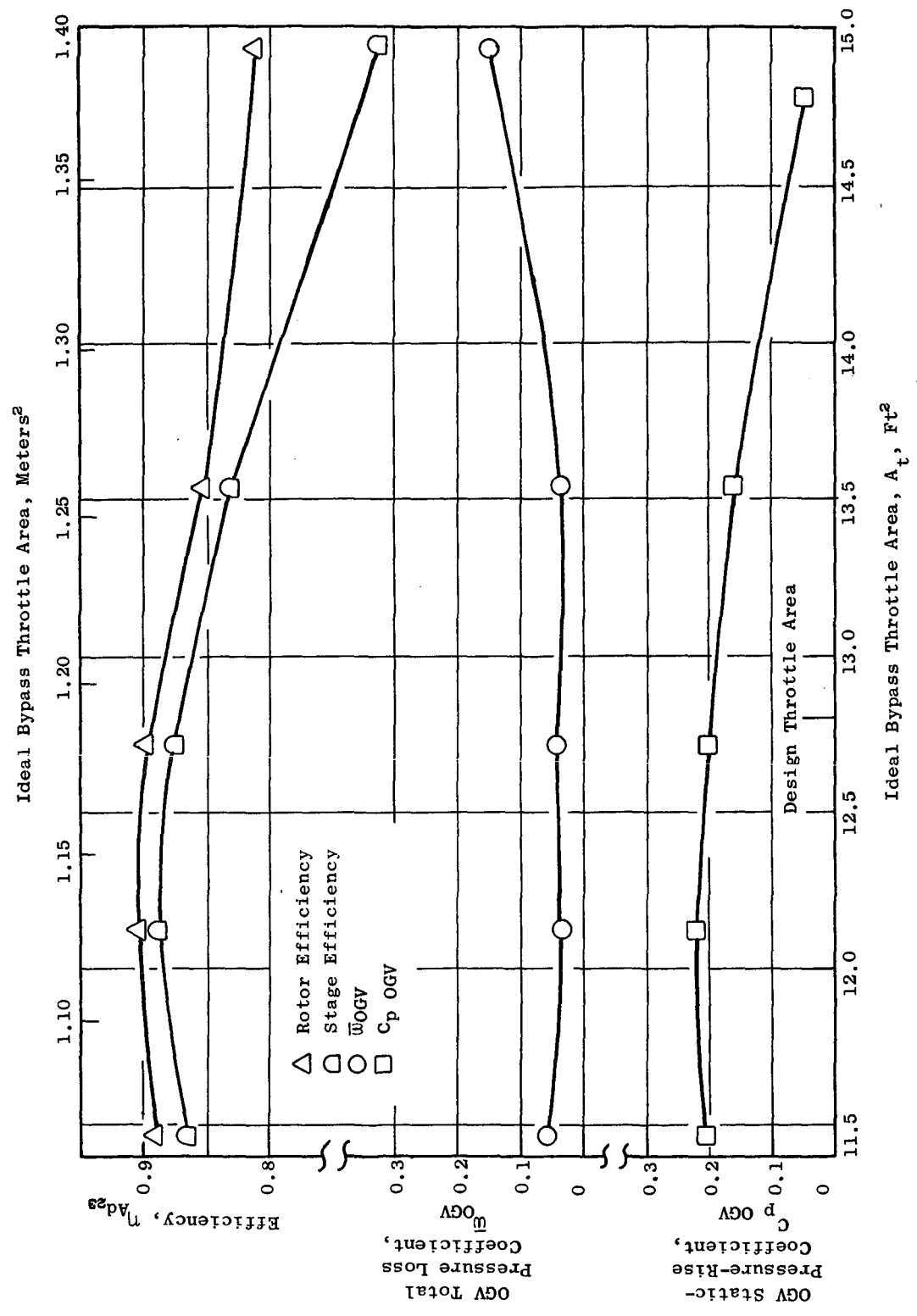


Figure 11. Variation of Element Properties with Throttling, Design Stream Function = 0.303.

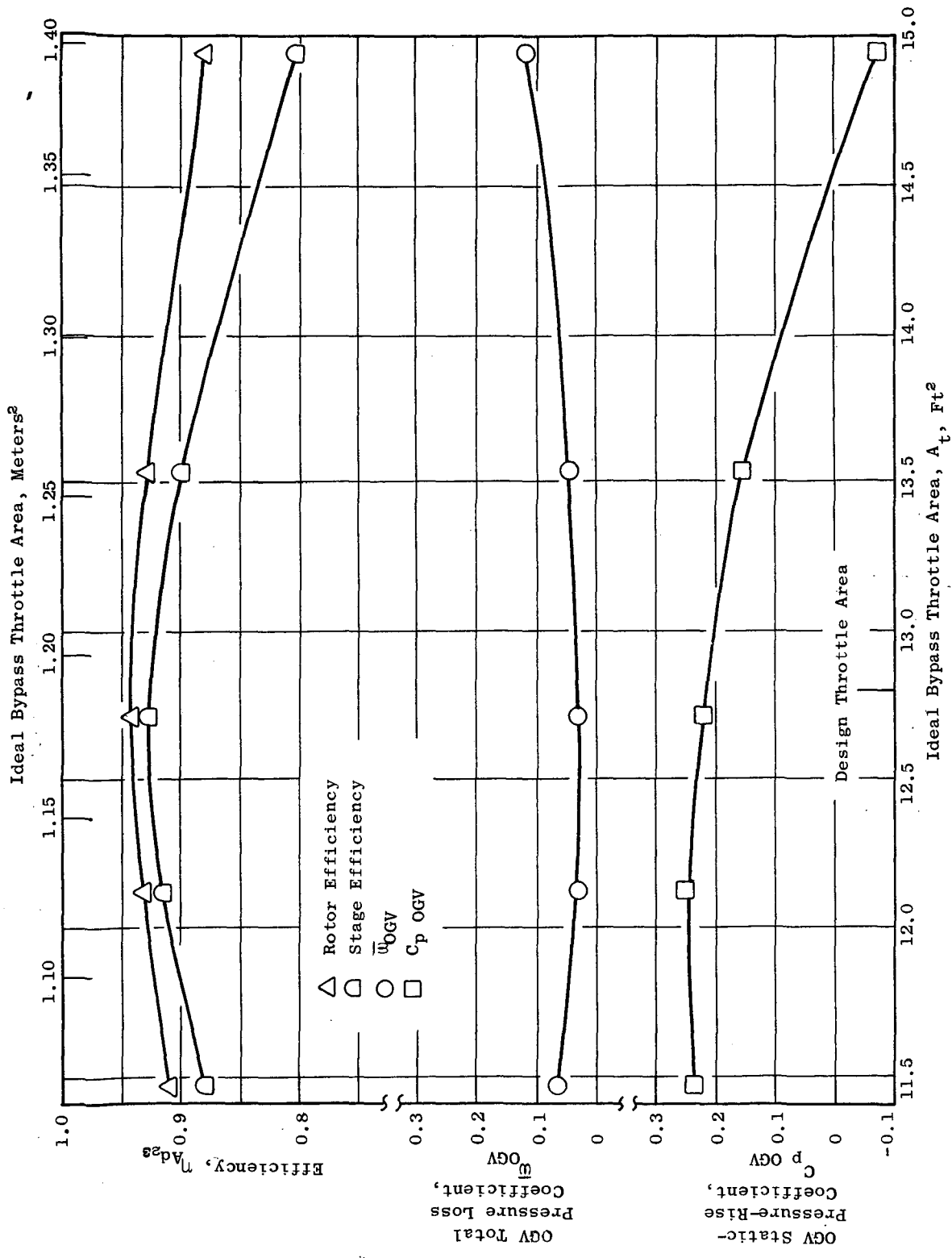


Figure 12. Variation of Element Properties with Throttling, Design Stream Function = 0.548.

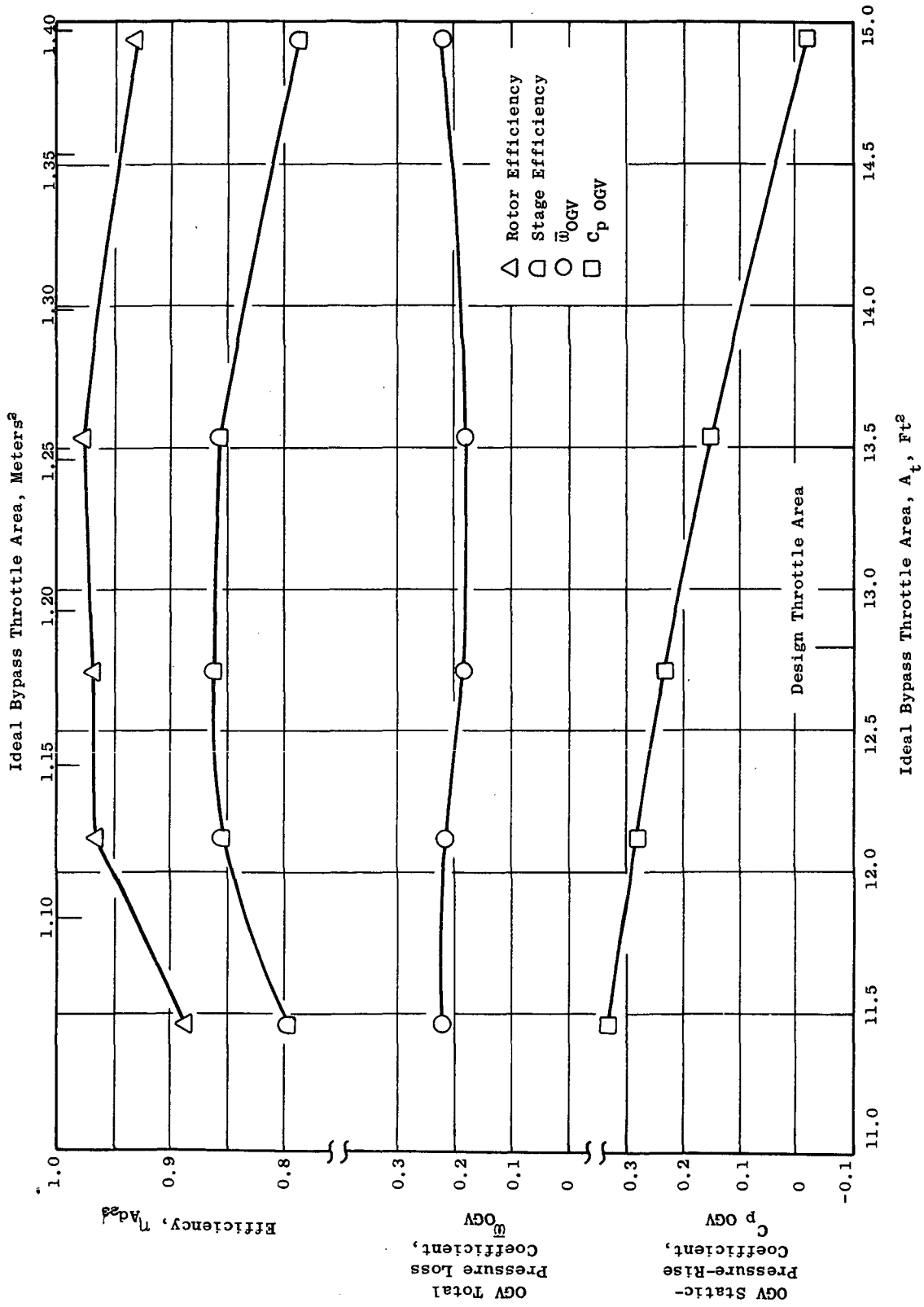


Figure 13. Variation of Element Properties with Throttling, Design Stream Function = 0.787 (Bypass ID).

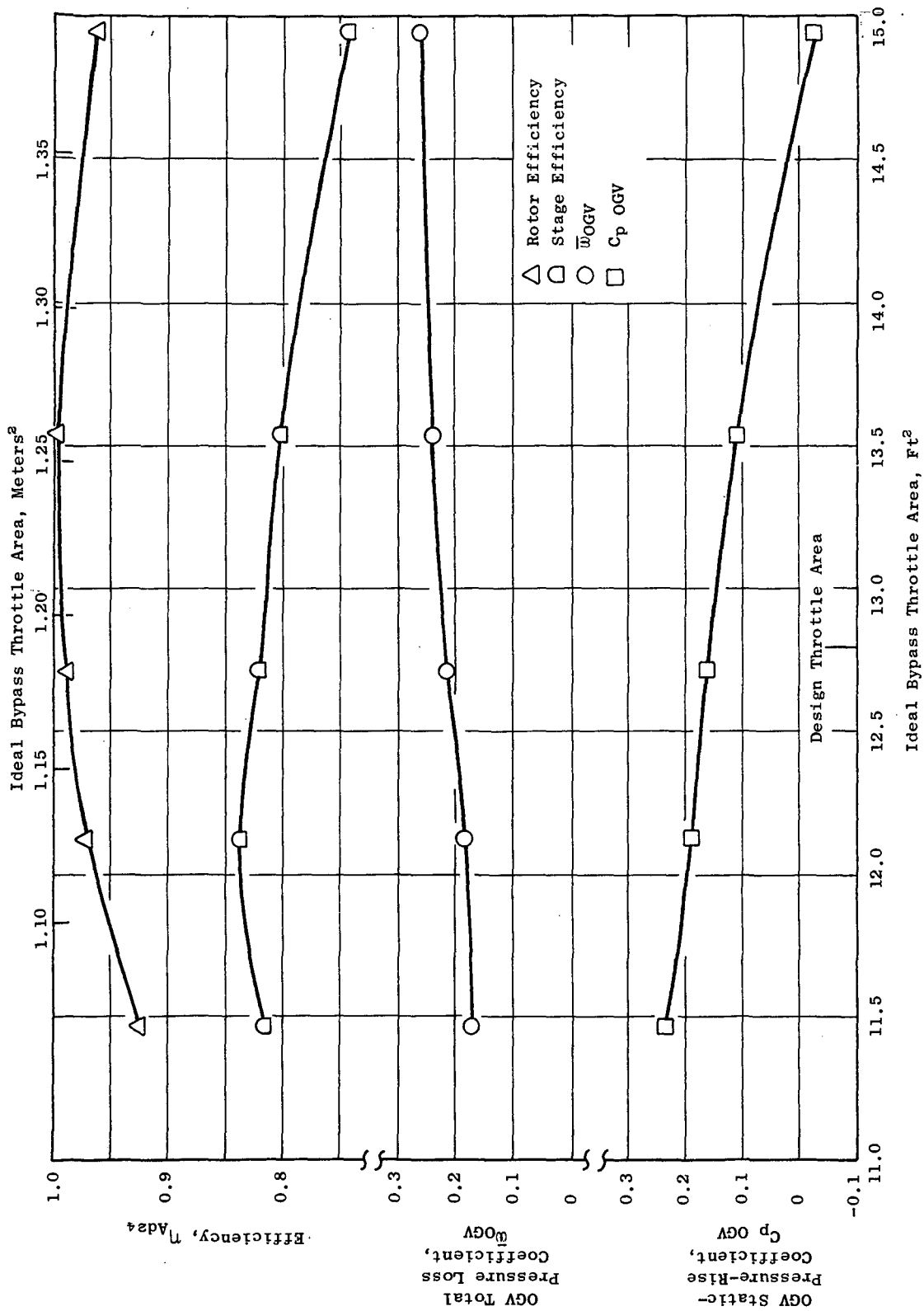


Figure 14. Variation of Element Properties with Throttling, Design Stream Function = 0.855 (Core OD).

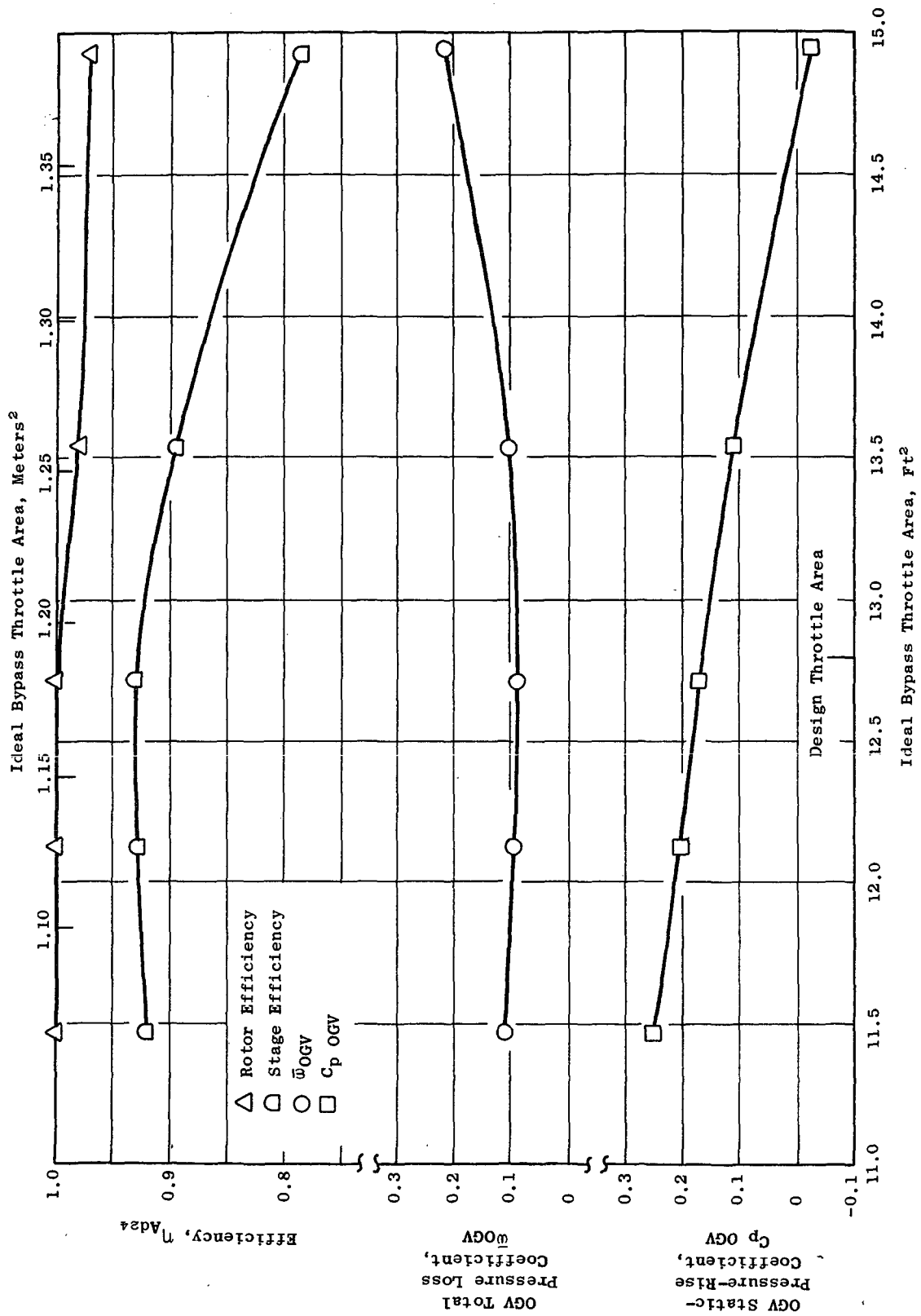


Figure 15. Variation of Element Properties with Throttling, Design Stream Function = 0.885.

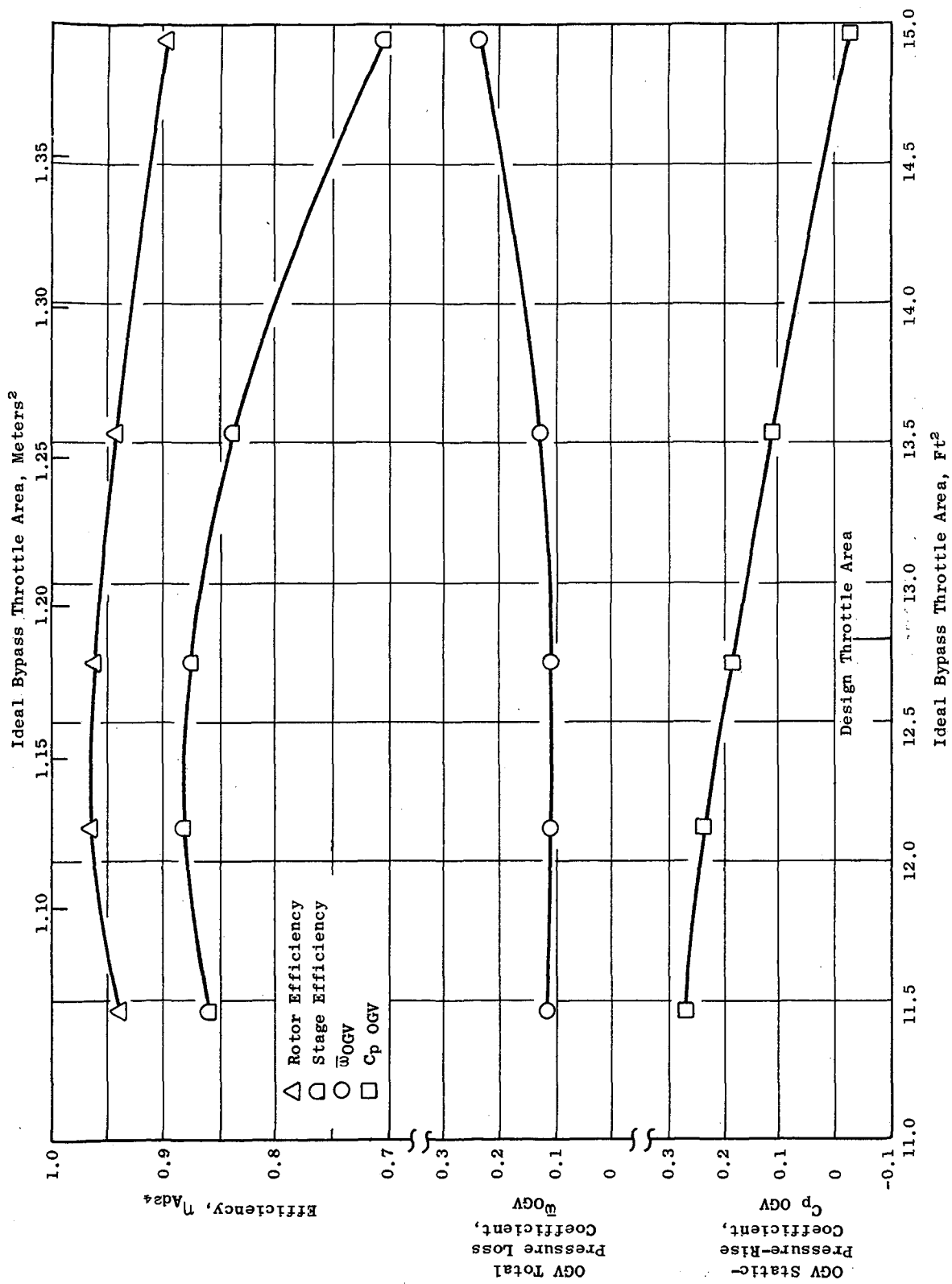


Figure 16. Variation of Element Properties with Throttling, Design Stream Function = 0.919.

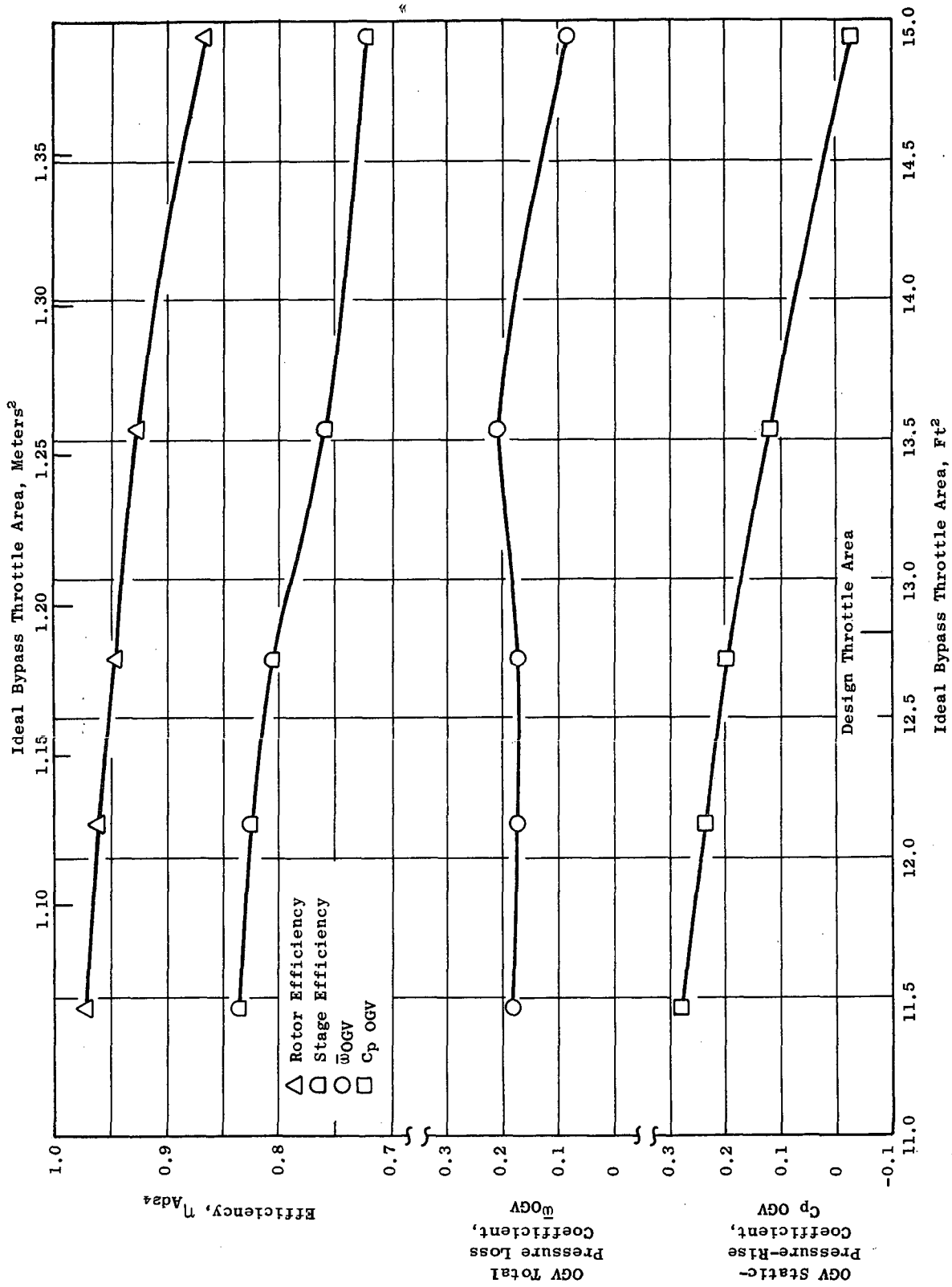


Figure 17. Variation of Element Properties with Throttling, Design Stream Function = 0.953.

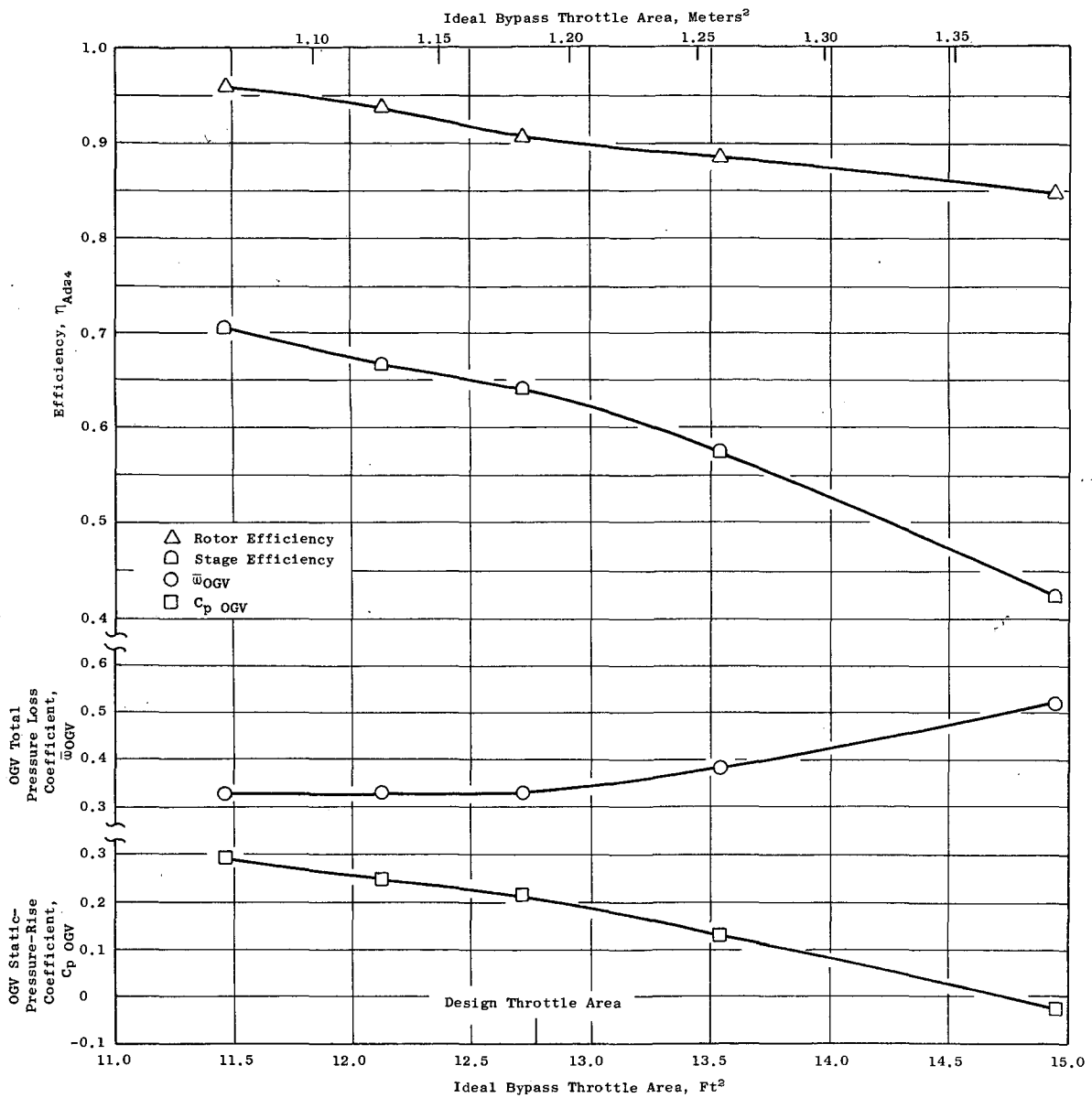


Figure 18. Variation of Element Properties with Throttling, Design Stream Function = 0.984 (Core ID).

radially. The outer three immersions of the fan core behave similarly. The inner two immersions of the fan core show a modest improvement in rotor efficiency with additional throttling.

### 5.3 DISTORTED FLOW PERFORMANCE

The Build 3 Fan C was tested with a tip radial, crosswind, and one-per-rev circumferential inlet distortion. Distortion was generated by screens mounted on a support structure which was located approximately 0.6 fan diameters in front of the rotor. The tip radial distortion generating screens covered the outer 40% of the annulus. The crosswind distortion generating screen had a circumferential extent of  $160^\circ$  and a radial extent covering 30% of the annulus area with the outermost 10% and the innermost 60% of the annulus area being open. The one-per-rev distortion extended over the full annulus height and was  $180^\circ$  in circumferential extent. The distortion levels generated by the screens are shown in Figure 19. Plots of the actual distortion patterns for a relatively closed throttle condition at 90% speed are shown in Figures 20 through 22. A contour plot of the inlet recovery pattern for the crosswind distortion is shown in Figure 23.

The overall performance maps for the distorted flow testing are shown in Figures 24 through 26. Also shown in the background is the clean inlet performance to facilitate comparison. The operational limit line was determined to be high rotor stress for all three distortions except for 50 and 60% corrected speed with the tip radial distortion and 50% corrected speed with the crosswind and one-per-rev circumferential distortions. For these four cases, a rotating stall was encountered. Since high rotor stress also determined the clean inlet operational limit line at corrected speeds higher than 60%, the loss in operating range with distorted inlet flow cannot be compared with other fans where rotating stall was the operational limit. The one-per-rev circumferential distortion resulted in no significant reduction in operating margin. The crosswind distortion resulted in a modest reduction in operating margin at all speeds with the largest reduction occurring at 70% corrected speed where the loss was 7%. The tip radial distortion resulted in a loss in operating margin similar to that observed for the crosswind distortion except in the 70% corrected speed region where the loss was 14%. In the distortion data reduction, no attempt was made to segregate the inlet pressures to account for a lower than average pressure entering the bypass portion with the tip radial and crosswind distortions.

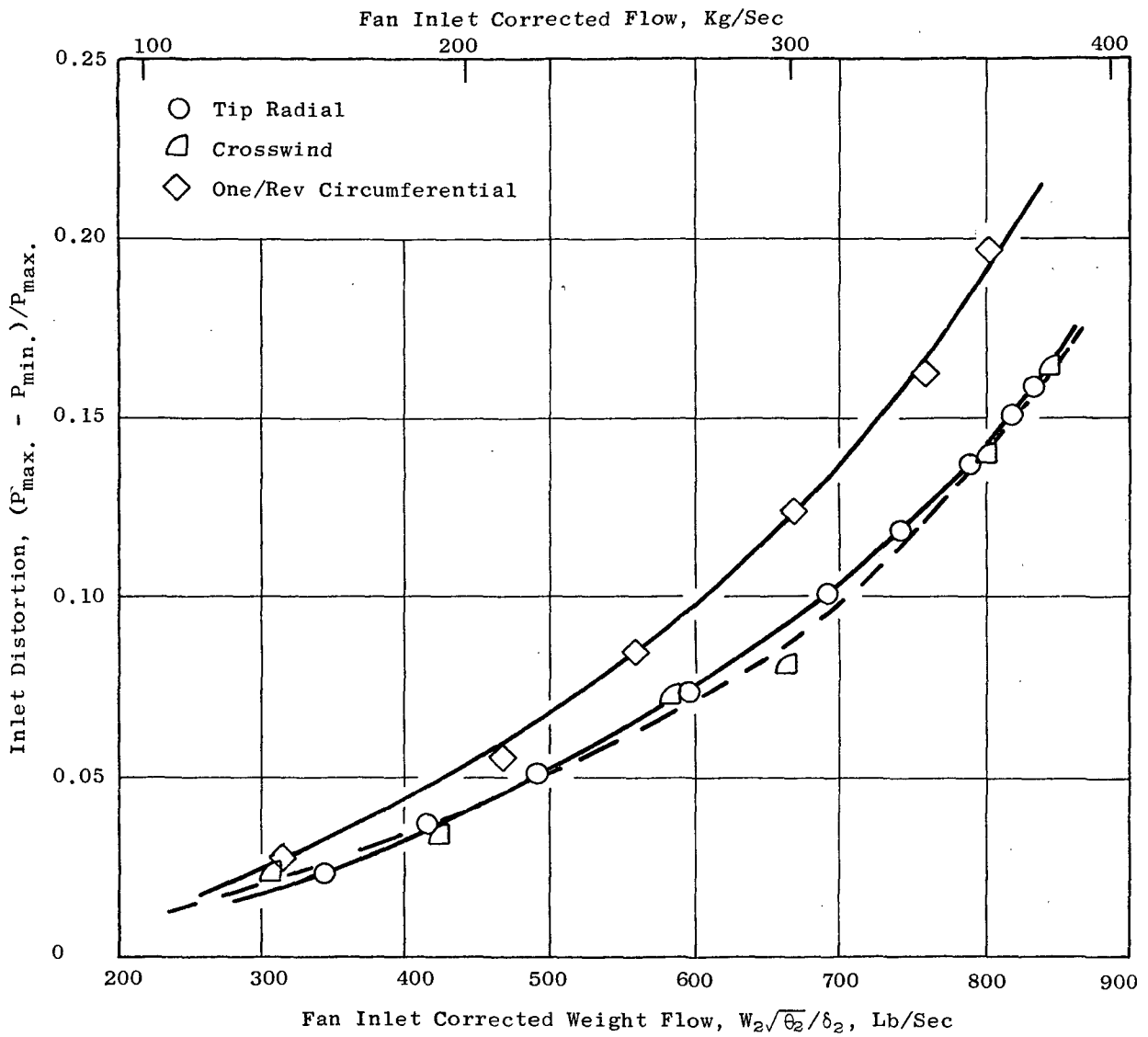


Figure 19. Inlet Flow Distortion Level.

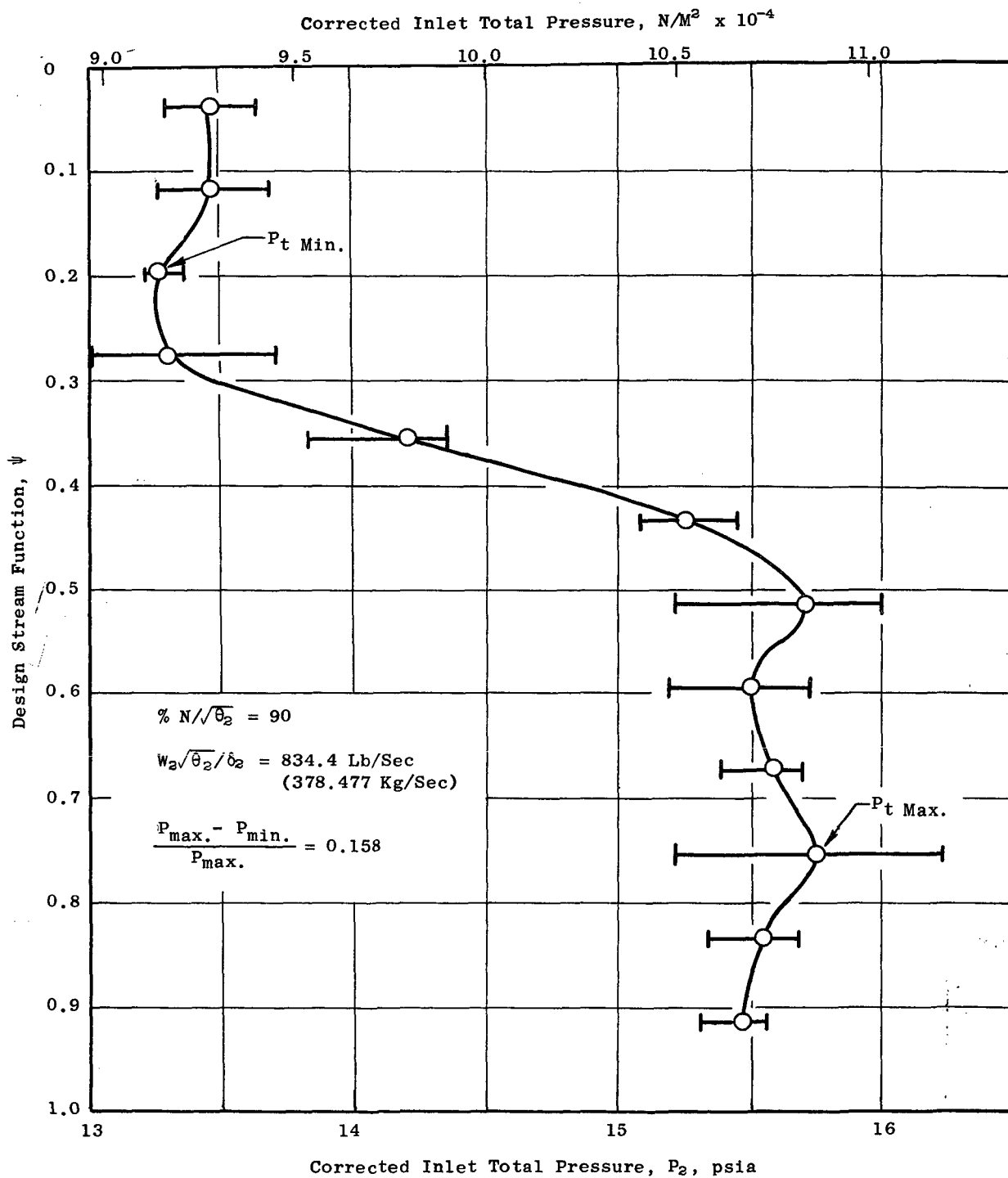


Figure 20. Tip Radial Distortion Inlet Pressure Profile.

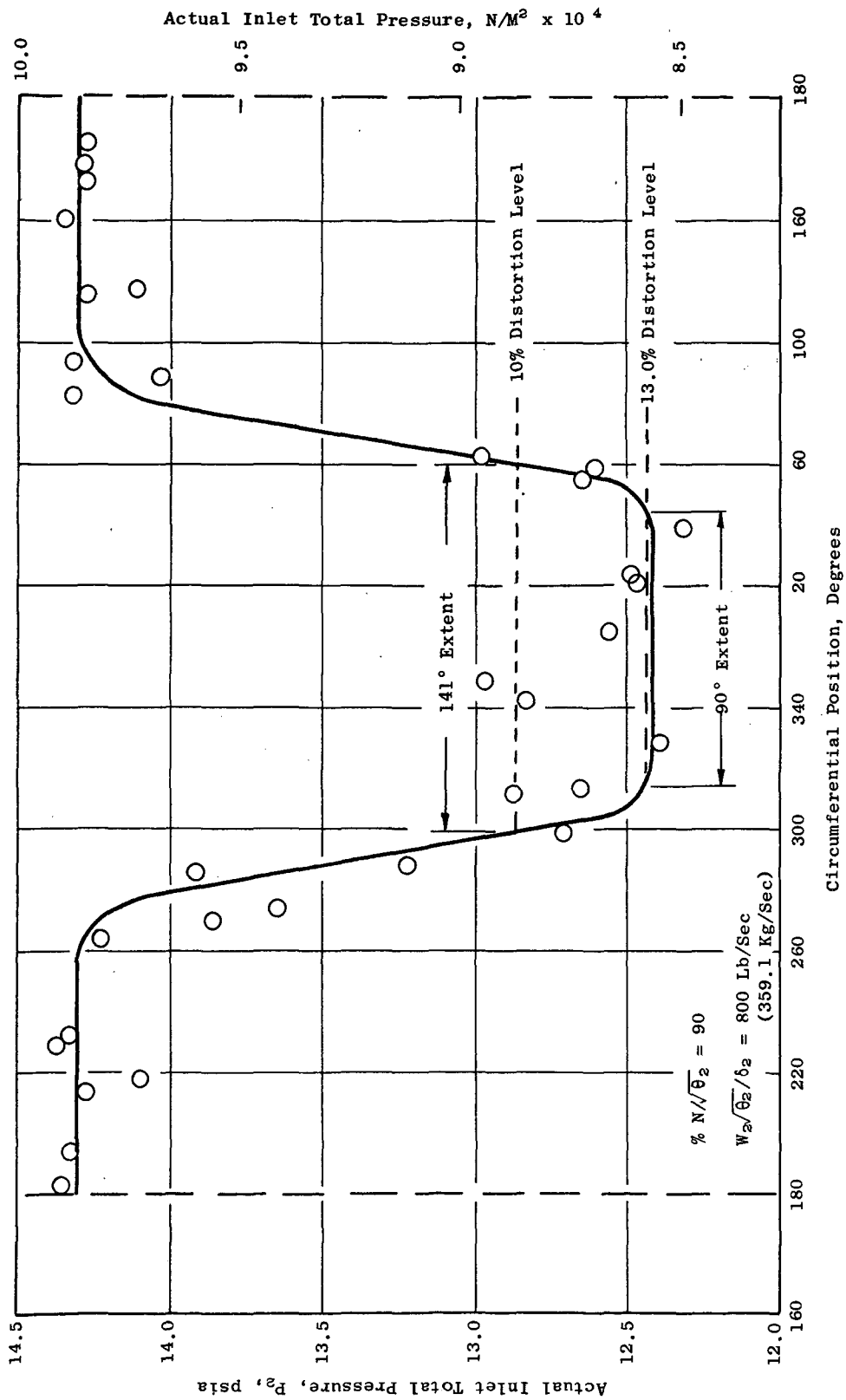


Figure 21. Crosswind Distortion Pattern.

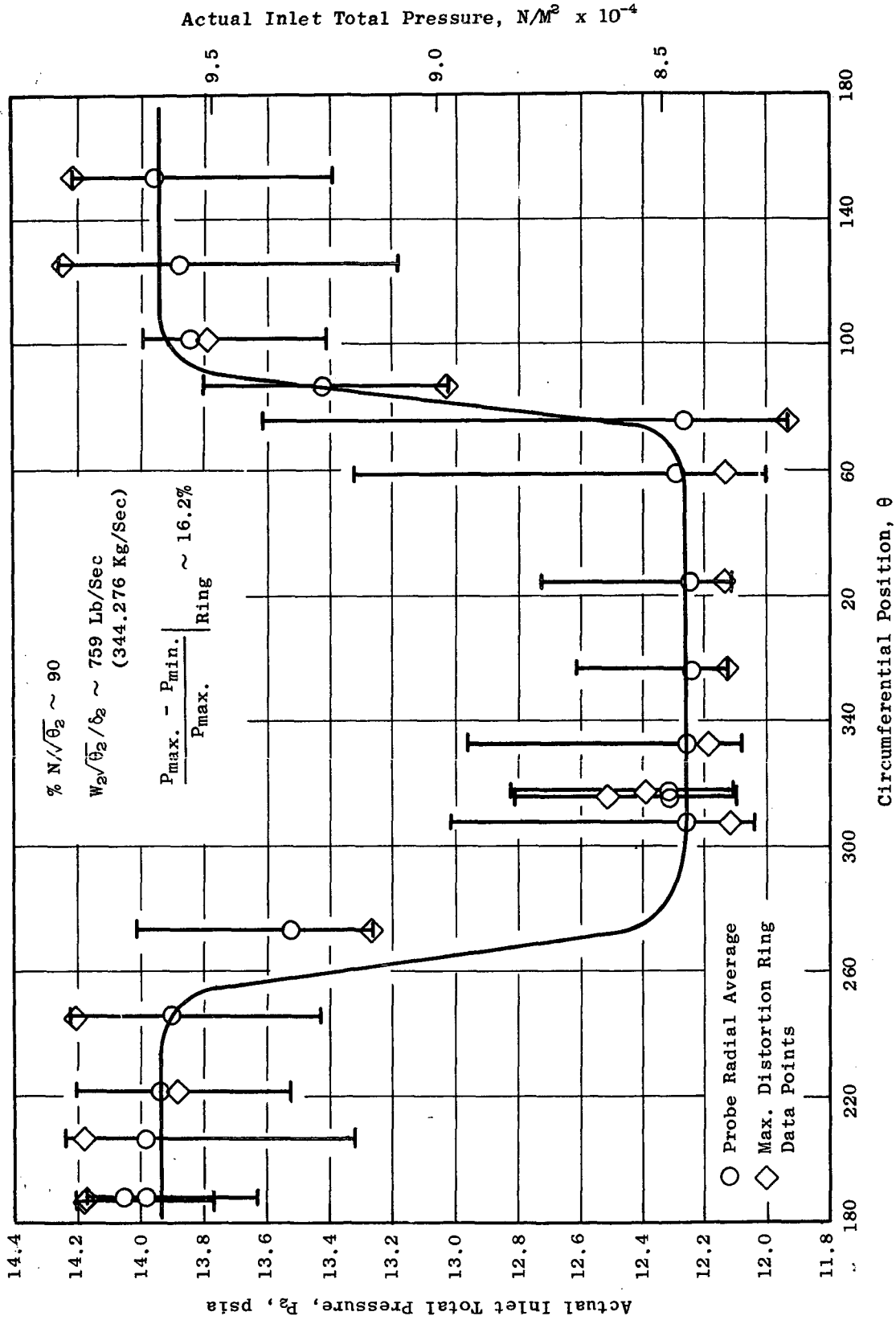


Figure 22. One/Rev Distortion Pattern.

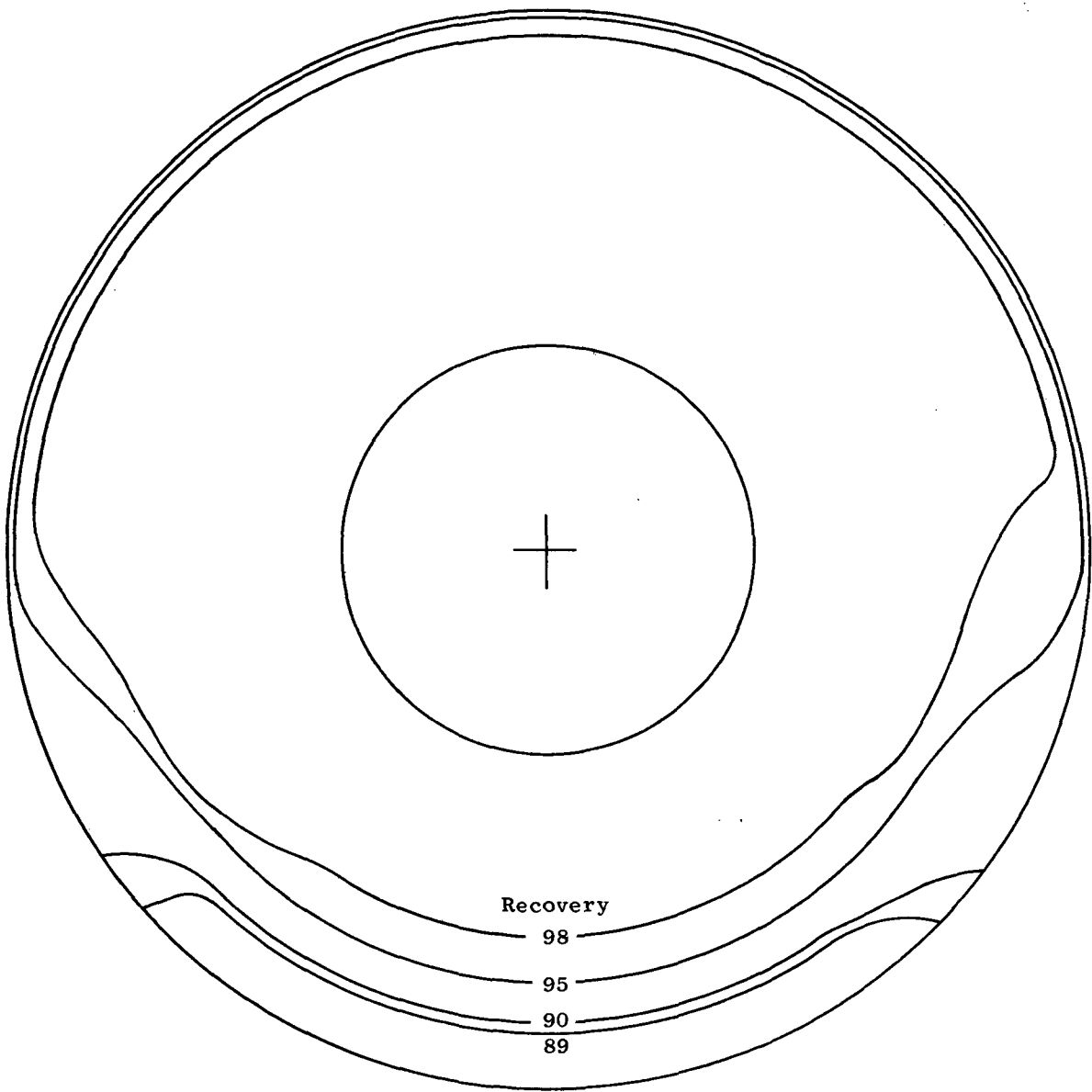


Figure 23. Inlet Pressure Recovery Contour, Crosswind Distortion.

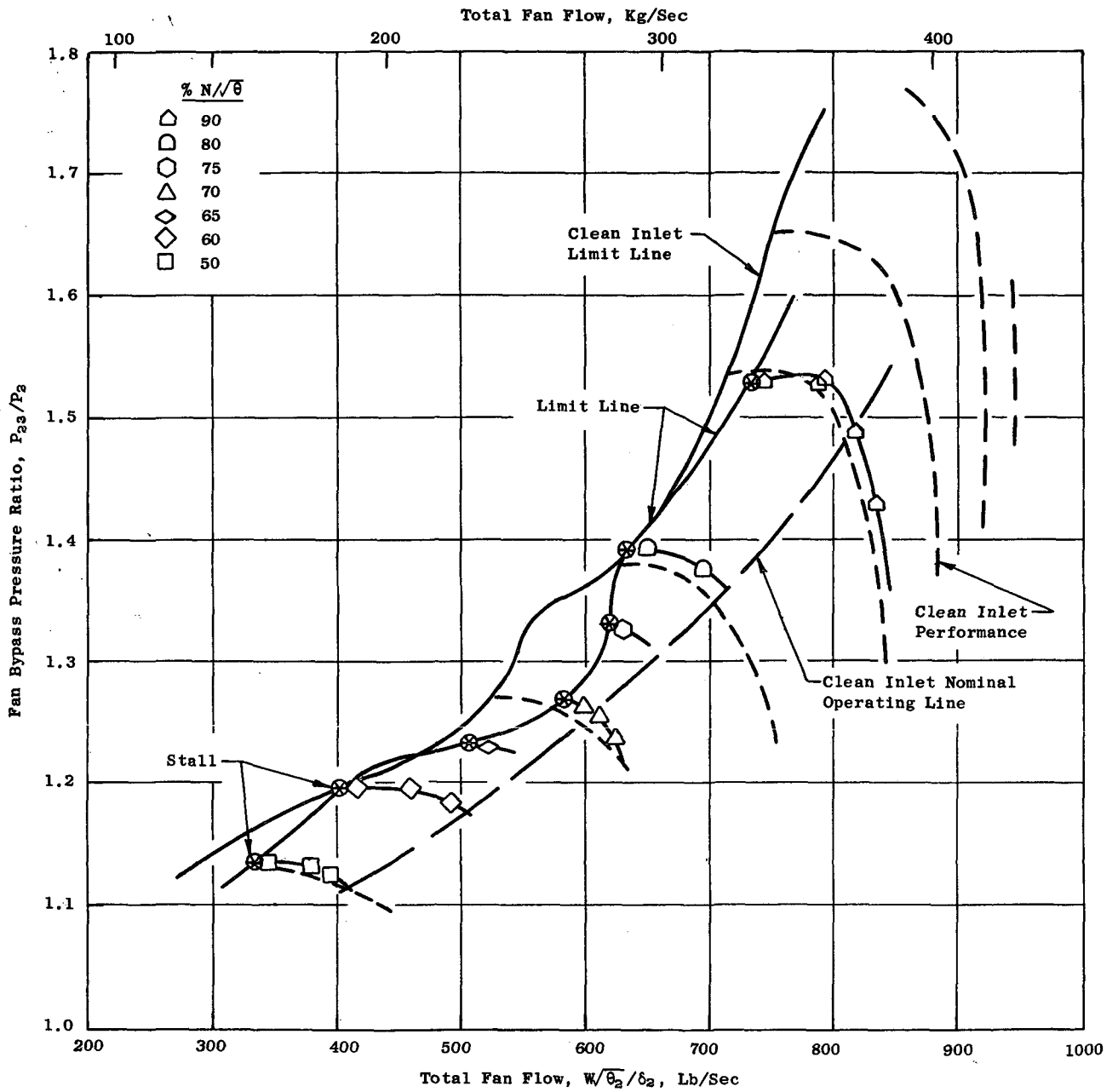


Figure 24. Fan C Performance Map, Tip Radial Inlet Distortion.

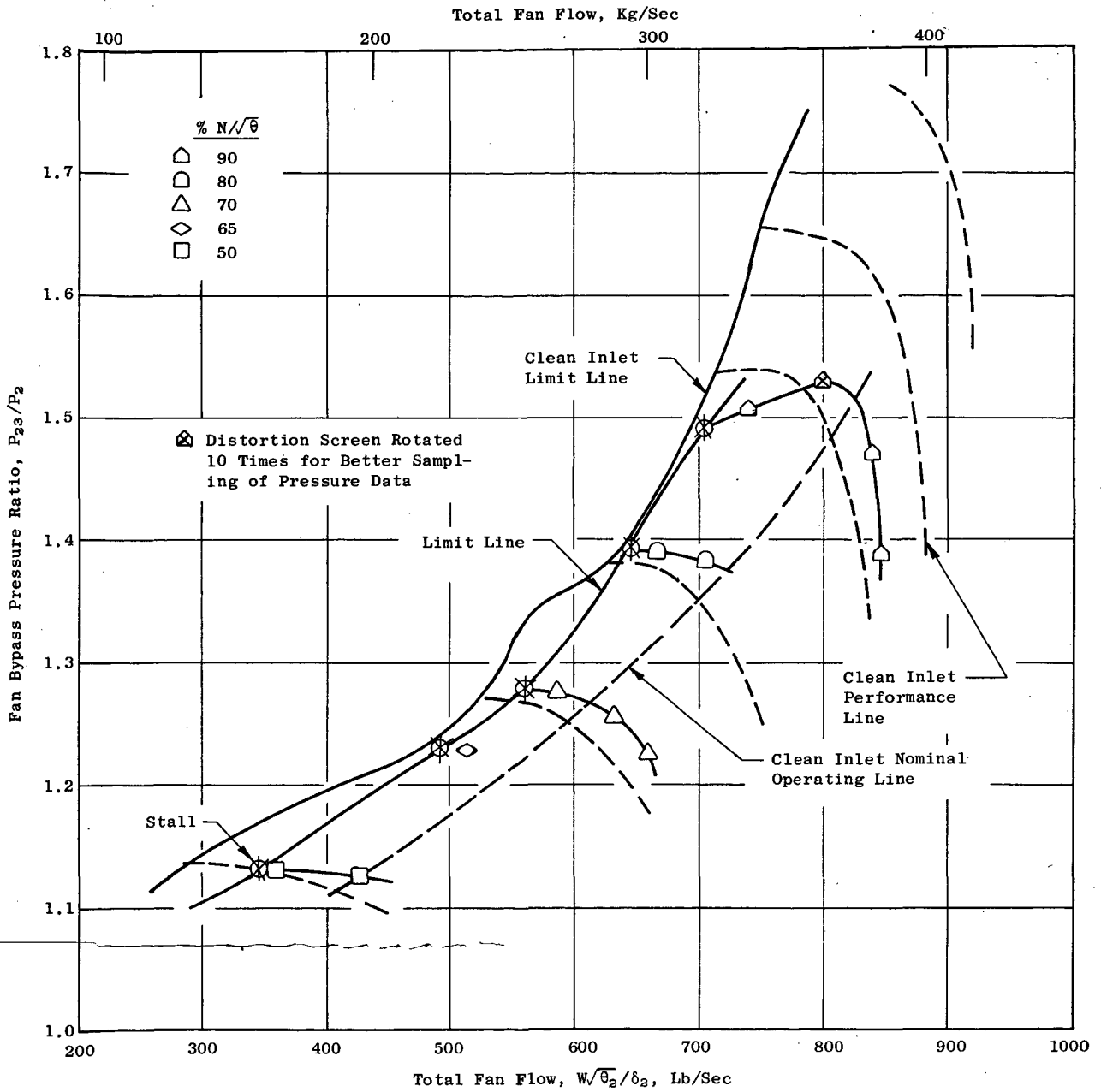


Figure 25. Fan C Performance Map, Crosswind Inlet Distortion.

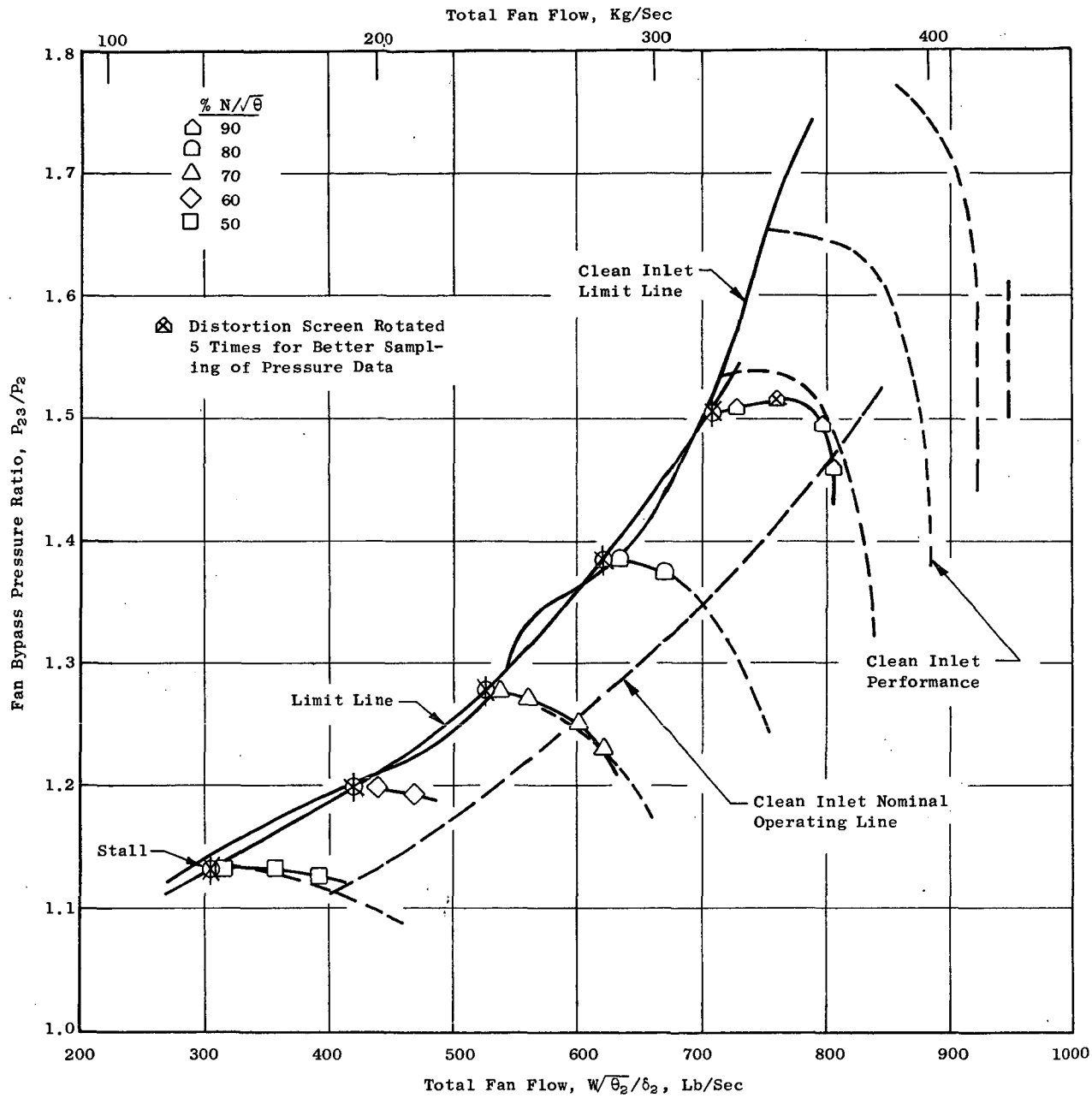


Figure 26. Fan C Performance Map, One/Rev Inlet Distortion.

## 6.0 SUMMARY OF RESULTS

The aerodynamic component test results of Fan C, a high-bypass-ratio, low-aerodynamic-loading, 1550 feet per second (472.4 m/sec) single-stage fan, which was designed to deliver a bypass pressure ratio of 1.60 with an adiabatic efficiency of 84.2% at a total fan flow of 915 lbs/sec (415.0 kg/s) yielded the following principal results:

1. With undistorted inlet flow, a bypass pressure ratio of 1.61 and an adiabatic efficiency of 83.9% at a total fan flow of 921 lbs/sec (417.8 kg/sec) were actually achieved at design speed. The peak adiabatic efficiency at design speed was 85.0% at a bypass portion pressure ratio of 1.68 and a total fan flow of 911 lbs/sec (413.1 kg/sec). The operating margin achieved at design speed was in excess of 14.6% and was 17.4% at 90% speed. At 105% corrected speed, a total fan flow of 946 lbs/sec (429 kg/sec) was achieved which gave a specific flow of 42.7 lbs/sec/ft<sup>2</sup> (208.0 kg/sec/m<sup>2</sup>) of annulus area. A fan core pressure ratio of 1.54 at an adiabatic efficiency of 82.3% was achieved at 100% corrected speed and the design flow of 152.8 lbs/sec (69.3 kg/sec).
2. The fan was tested with tip radial, crosswind, and one-per-rev screen-generated inlet distortion patterns. The distortion magnitude was about 15% at 90% speed, which is near the take-off condition. The tip radial pattern caused the limit line to be lowered by an amount equivalent to a loss in operating margin of 14%. The crosswind pattern caused a 7% loss. This loss in operating margin occurred at 70% speed for both patterns; the loss in operating margin at other speeds was significantly less. With the one-per-rev pattern, no significant change to the limit line was observed.

## 7.0 REFERENCES

1. Experimental Quiet Engine Program, Contract No. NAS3-12430, Phase 1 Engine Design Report, Volume 1, Section 4.0 Fan Aerodynamic Design, NASA CR-72967, March 15, 1970
2. Giffin, R.G., Parker, D.E. and Dunbar, L.W. "Experimental Quiet Engine Program Aerodynamic Performance of Fan B, NASA CR-72993," August 1972.
3. Giffin, R.G., Parker, D.E. and Dunbar, L.W. "Experimental Quiet Engine Program Aerodynamic Performance of Fan A, NASA CR-120858," June 1972.
4. Seyler, D.R. and Gostelow, J.P; "Single Stage Experimental Evaluation of High Mach Number Compressor Rotor Blading, Part 2 - Performance of Rotor 1B," NASA CR-54582, Sept. 22, 1967.

## APPENDIX I

### INSTRUMENTATION

An overall meridional view of the test vehicle with the test instrumentation superimposed is shown in Figure 27. The fan inlet conditions were measured by four six-element pitot-static rakes located in the cylindrical section of the inlet duct between the bellmouth and the fan inlet. Twenty-four thermocouples attached to the inlet FOD screens were used for determining inlet total temperature. The pressure and temperature sensors were located approximately on centers of equal area. The fan discharge total temperature and total pressure were measured by arc rakes. Seven arc rakes were located behind the fan bypass portion outer OGV's, and five arc rakes were located behind the fan core portion inner OGV's. Radially, the arc rakes were located on centers of equal design mass flow of the bypass portion and fan core portion, respectively.

The bypass portion arc rakes were composed of 12 elements with each element containing one temperature and one pressure sensor. This construction technique enables pressure and temperature sampling from a common fluid region and minimizes the effects of spatial variation in computing efficiency. The two outer arc rakes spanned one OGV spacing. The remaining five arc rakes spanned two OGV spacings. The five core portion arc rakes were of similar construction to that of the bypass portion arc rakes but with seven elements each containing one total pressure and total temperature sensor. These rakes spanned two OGV spacings.

The rotor discharge total pressure in the fan core portion was measured by three five-element radial rakes. The radial positioning of the elements were on centers of equal design flow. The total pressure at discharge from the transition duct leading to the core compressor was measured by five, five-element radial rakes with the elements being located on centers of equal area. (These rakes are identical with those used for core compressor inlet instrumentation on the TF39/CF6 engines.)

In addition to this instrumentation, there were wall static pressures located in the inlet duct and along the outer casing, along the inside diameter of the bypass portion, around the splitter leading edge, and throughout the ducting for the fan core portion flow. Total pressure profile rakes were located on the inlet duct outer casing just forward of the fan rotor and on the inside diameter of the bypass portion midway between rotor exit and outer OGV inlet. The total number of pressure sensing elements exceeded the recording capability of the test stand. Three alternate pressure matrices were employed to record those pressures judged most useful for the particular test configuration objectives. Traversing probes were located at fan rotor inlet (a cobra and a wedge static), fan rotor exit (a cobra, a disc static, and a high response Kulite transducer), outer OGV inlet (a cobra), and inner OGV inlet (a cobra). The traverse probes were used only at selected operating points near the aerodynamic design

PRECEDING PAGE BLANK NOT FILMED

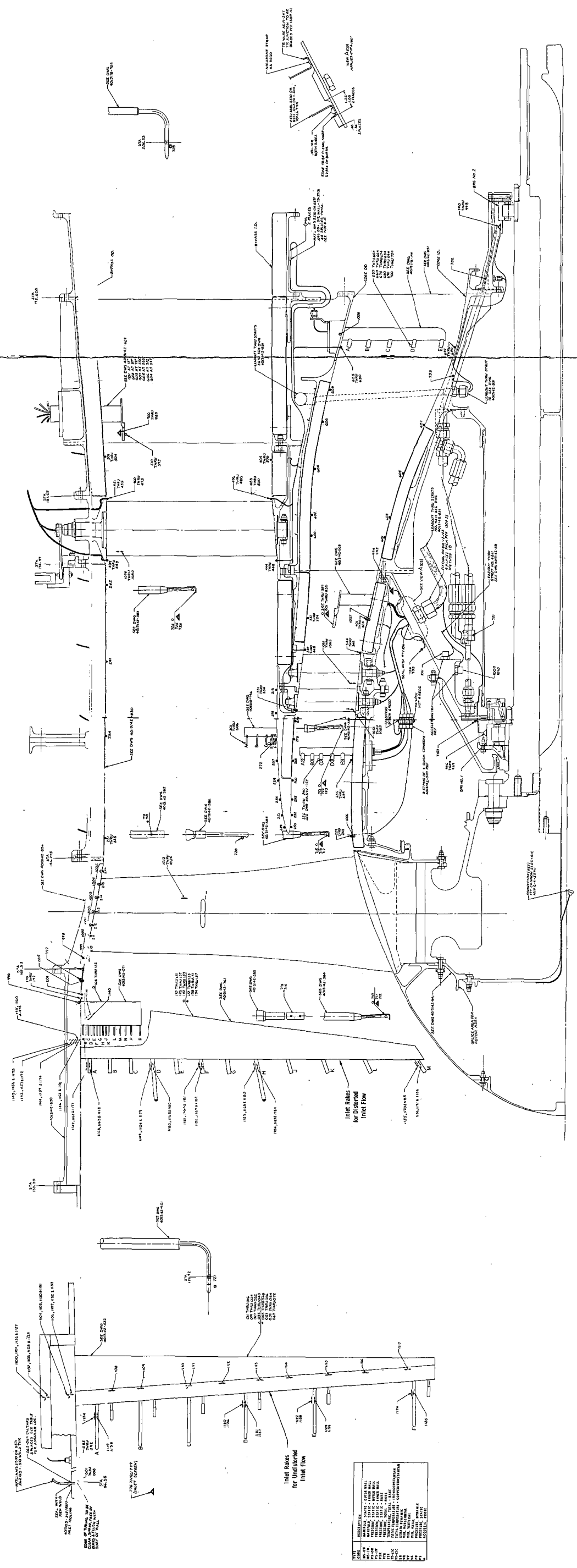


Figure 27. Fan C Test Vehicle Instrumentation Location.

PRECEDING PAGE BLANK NOT FILMED

point. Also, 10 Kulite transducers were mounted in the casing over the rotor tip for determining the time-varying static pressure field.

For the distortion testing, the fan inlet total pressure was measured by three 12-element radial rakes located just upstream of the fan rotor. The elements were positioned radially so as to be on centers of equal design flow.

## APPENDIX II

## COMPUTATION OF OVERALL FAN PERFORMANCE

The total fan flow was computed from the inlet total and static pressure, the inlet screen total temperature, a measured area, and an assumed flow coefficient of 0.992. Figure 28 is a plot of the normalized outer casing velocity profile forward of the fan face as deduced from the wall static pressure and the total pressure profile rake. The results are presented for four typical flow rates. A computation of the displacement thickness from the boundary layer profile yields an equivalent effective area coefficient of 0.993. The total temperatures and total pressures were recorded individually and arithmetically averaged. Generally, the static pressures were manifolded with only the single manifold value being recorded. However, the first instrumentation matrix recorded the individual static pressures from one of the inlet rakes as a check on the radial pressure profile. The inlet total and static pressure profiles for a typical high flow point are presented in Figure 29. The static pressure profile is nearly constant radially, as expected. The total pressure profile is slightly skewed towards the outside diameter; however, this skew is typical of all data points. It is believed that the closeness of the inlet bellmouth to the facility protection screen is responsible for the skew since the potential flow field in front of the bellmouth will have its highest velocity along the centerline, and, hence, this location will yield the largest screen pressure drop. The fan core portion flow was measured by a calibrated flow meter located in the facility discharge piping. The bypass portion flow is obtained by subtracting the fan core portion flow from the total fan flow; no independent measurement of the fan bypass flow was made.

The fan face total temperature and total pressure was taken as the arithmetic average of the screen-mounted total temperatures and pitot-static total pressures. At discharge, the fan bypass portion and fan core portion are treated separately. For each portion, the arithmetic average of the pressures and temperatures for each arc rake is computed. (The average excludes the last element on each rake, the 12th element on the fan bypass portion rakes, and the seventh element on the fan core portion rakes since this element is spaced one blade pitch from the first element and is, therefore, redundant for performance computation. This last element was incorporated to provide a check on the periodicity of the flow leaving the OGV's.) A linear variation in static pressure between wall measured values at the outside diameter and inside diameter was assumed. The averaged total temperature reading at each immersion is corrected for static wire (the error encountered in measuring an oil bath temperature) and Mach number at the Mach number and temperature of that immersion. The procedure then mass weights, radially, the actual enthalpy to obtain an average discharge total temperature and the ideal enthalpy rise to obtain an average discharge total pressure; Reference

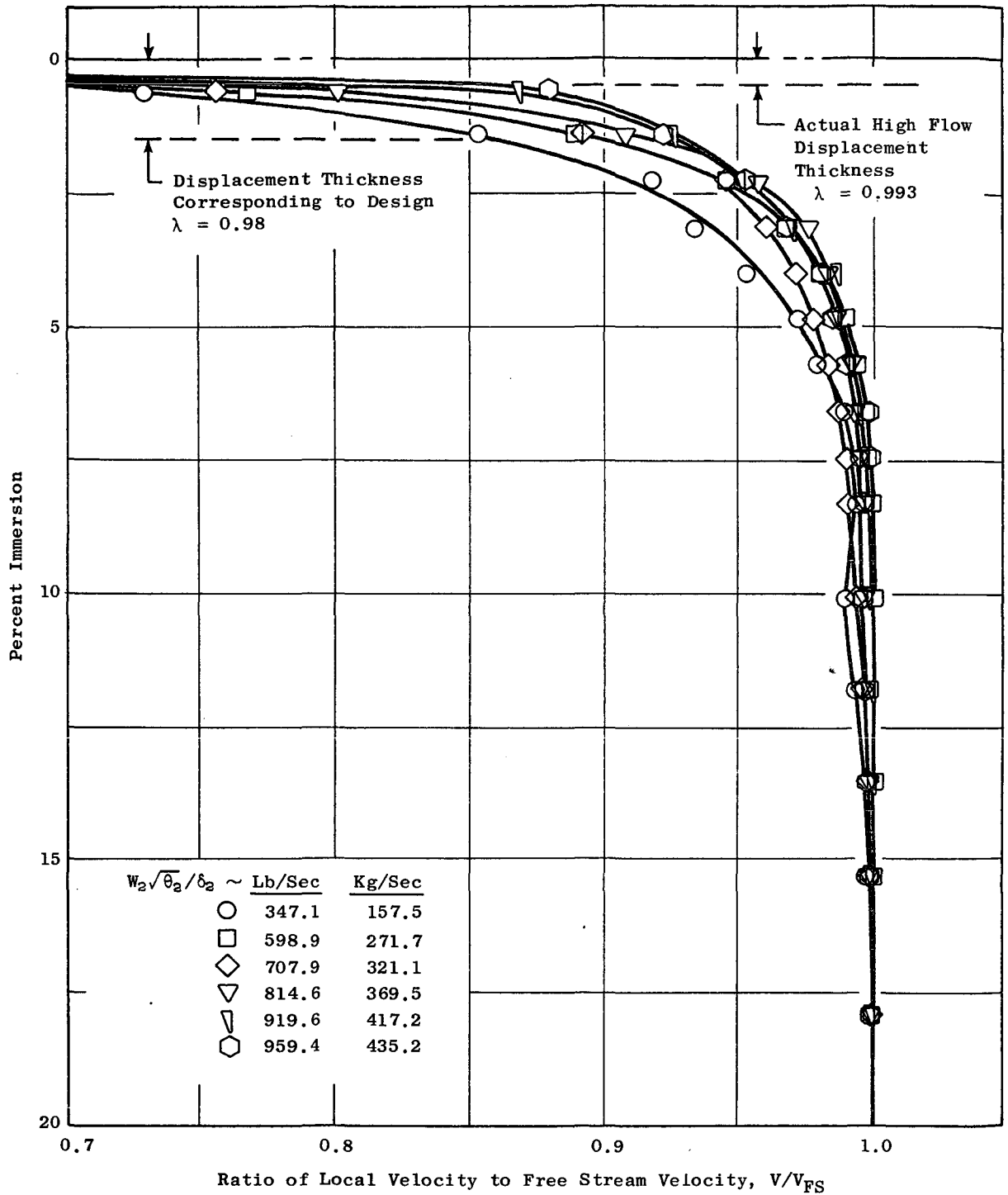


Figure 28. Inlet Boundary Layer Description.

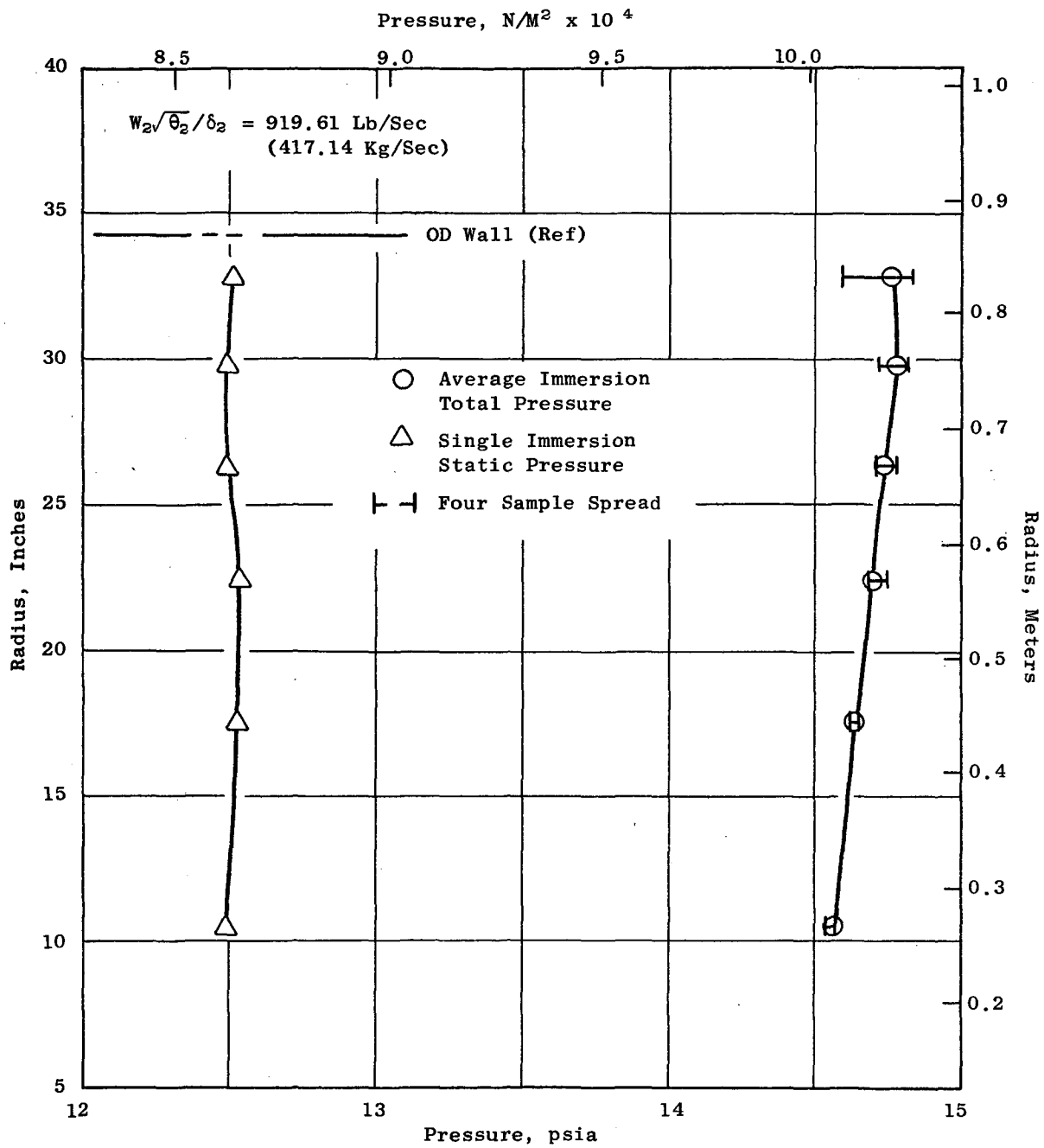


Figure 29. Typical Inlet Duct Pressure Profiles.

2 presents the calculation procedure in detail. With the average pressure ratio and temperature rise of fan bypass portion and fan core portion, the actual air properties, including the effects of humidity, are used to compute the efficiency of the two streams.

A computation was performed to determine the radial variation of stage and rotor only adiabatic efficiency and OGV total-pressure-loss coefficient and static-pressure-rise coefficient. A constant ratio of specific heats is used in these computations. The calculations assume the arithmetically averaged wake rake total pressure and total temperatures at OGV discharge. No change in total temperature is permitted through the OGV. For the bypass portion, the average of the three highest total-pressure wake-rake elements is assumed to be the pressure in front of the OGV. In the fan core portion, the elements at each radius on the three radial rakes at rotor exit were averaged circumferentially to determine the OGV inlet total pressures. At inlet and discharge, the stream static is obtained by linear interpolation between wall values.

Since data from the traverse probes are generally considered to be less reliable than that from fixed instrumentation, traverse data is viewed as giving only an indication of trends and is not used in performance calculations.

#### DATA ACCURACY

##### Pressure

The recording system for pressure uses a method whereby each transducer (which measures up to 10 vehicle pressures) is calibrated on each reading against a CEC electromanometer which in turn is calibrated before and after each test against a dead-weight tester which can be traced to the National Bureau of Standards. This procedure results in an overall accuracy of pressure measurements of  $\pm 0.25$  percent of level.

##### Temperature

The recording system used for temperatures has a readability of one microvolt and is periodically calibrated against a standard which is traceable to the National Bureau of Standards giving an overall accuracy of recording of  $\pm 3$  microvolts or approximately  $\pm 0.12^\circ$  F.

In addition, static wire and dynamic recovery ratio calibrations are performed on all sensors used for performance measurements. It is estimated that the overall RMS temperature measurement accuracy is  $\pm 0.5^\circ$  for CC wire and  $\pm 0.75^\circ$  for CA wire.

## Flow

There is no error in the total pressure sensed by the inlet pitot-static instrument. The static pressure sensed by the inlet pitot-static instrument has, under ideal conditions, an estimated error of 0.25% of the dynamic pressure. However, because of minute differences in probe-to-probe manufacture and or alignment, a sensing error of 1% of the dynamic pressure can be expected.

The data acquisition accuracy (or more appropriately inaccuracy) are the extremes expected for the individual element measurements. Since some elements read high while other elements read low it is more reasonably expected that the overall performance inaccuracies are on the order of one-fourth of the inaccuracies of the individual elements. The problem of data sampling is at least as important in overall performance accuracy as the ability to properly sense and record the data. A treatment of this problem is beyond the scope of the current report.

## APPENDIX III

## OVERALL PERFORMANCE DATA FOR BUILDS 1 AND 2

The measured bypass portion performance for the Build 1 and 2 Fan C stage is shown in Figures 30 and 31, respectively. Referring to Figure 30, the Build 1 bypass performance map, the measured design speed flow, at the design pressure ratio of 1.60, was 907 lb/sec (411.4 kg/sec) which is 0.87% less than the design value of 915 lbs/sec (415.0 kg/sec). At this point the bypass adiabatic efficiency was 78.8%. A peak design speed efficiency of 79.0% was measured at a pressure ratio of 1.635. At corrected speeds below 100% the peak efficiency generally remained at the 79.0% level. However, at a corrected speed of 105%, the peak recorded efficiency was 82.3% at a pressure ratio 1.736.

On test observations of over-the-rotor high response pressure pickups showed a definite discontinuity in the shock pattern as corrected speed was gradually increased from 100 to 105%. Stabilized steady-state readings were recorded at corrected speeds of 100, 101.8, 102.8, 103.6, and 105% at constant DV settings (the data from each of these readings is shown on the performance map). At corrected speeds of 100 and 101.8% the shock patterns, as indicated by the high response pressure pickups, were quantitatively similar. The 103.6 and 105% corrected speed shock patterns were also quantitatively similar. At 102.8%, corrected speed the shock pattern alternated between a pattern that was quantitatively similar to that observed at 101.8% and that observed at 103.6% corrected speed. The period of the alternations was on the order of seconds, with the flow appearing steady between alternations. The change from one shock pattern to the other, irrespective of direction, appeared to be discontinuous. The observed behavior was similar to what would be expected from a fixed geometry supersonic inlet, operating above the starting inlet Mach number with the shock positioned near the throat when subjected to small increases and decreases in backpressure. Tracking the efficiency for this series of readings on the overall performance map, Figure 30, shows an increase of approximately three points between the 101.8 and 103.6% corrected speed points. A continuous acceleration between 100 and 105% corrected speed was also performed on a somewhat more open operating line. On test observation of the high response pressure pickups showed a shock pattern discontinuity similar to that described above.

The operational limit line was determined from 50 to 90% corrected speed. At 50 and 70% corrected speed, rotating stall was the operational limit. At the higher speed points, high rotor stress in the blade outer panel precluded further increases in backpressure. It is speculated, however, that only a small additional closure of the DV would have resulted in rotating stall. This speculation is, in part, based on comparison to the Build 2 operational limit line, Figure 31, where rotating stall was encountered at all speeds tested. At 90% corrected speed, the operating margin relative to the design sea level static operating line is 23%.

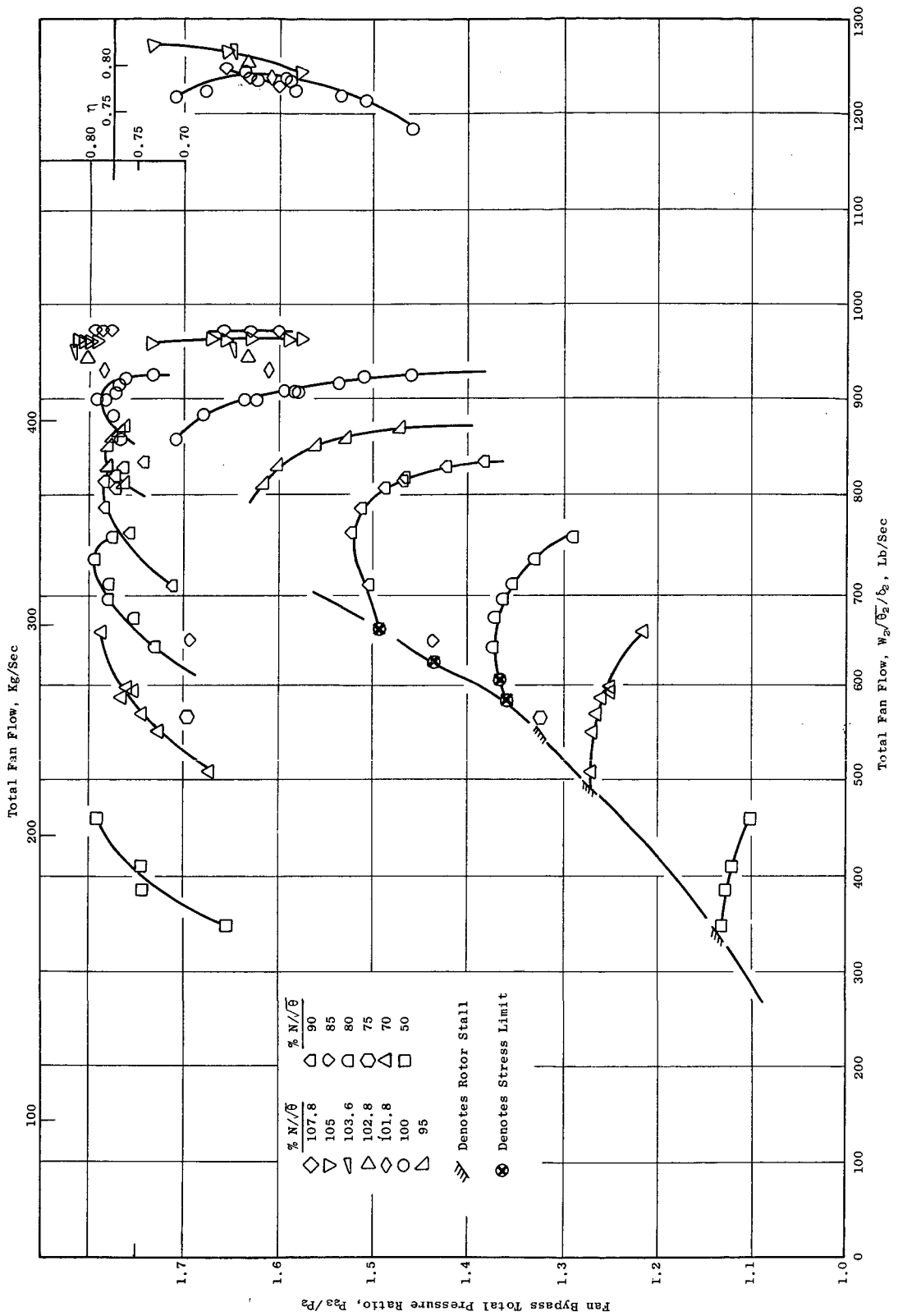


Figure 30. Build 1 Bypass Performance Map.

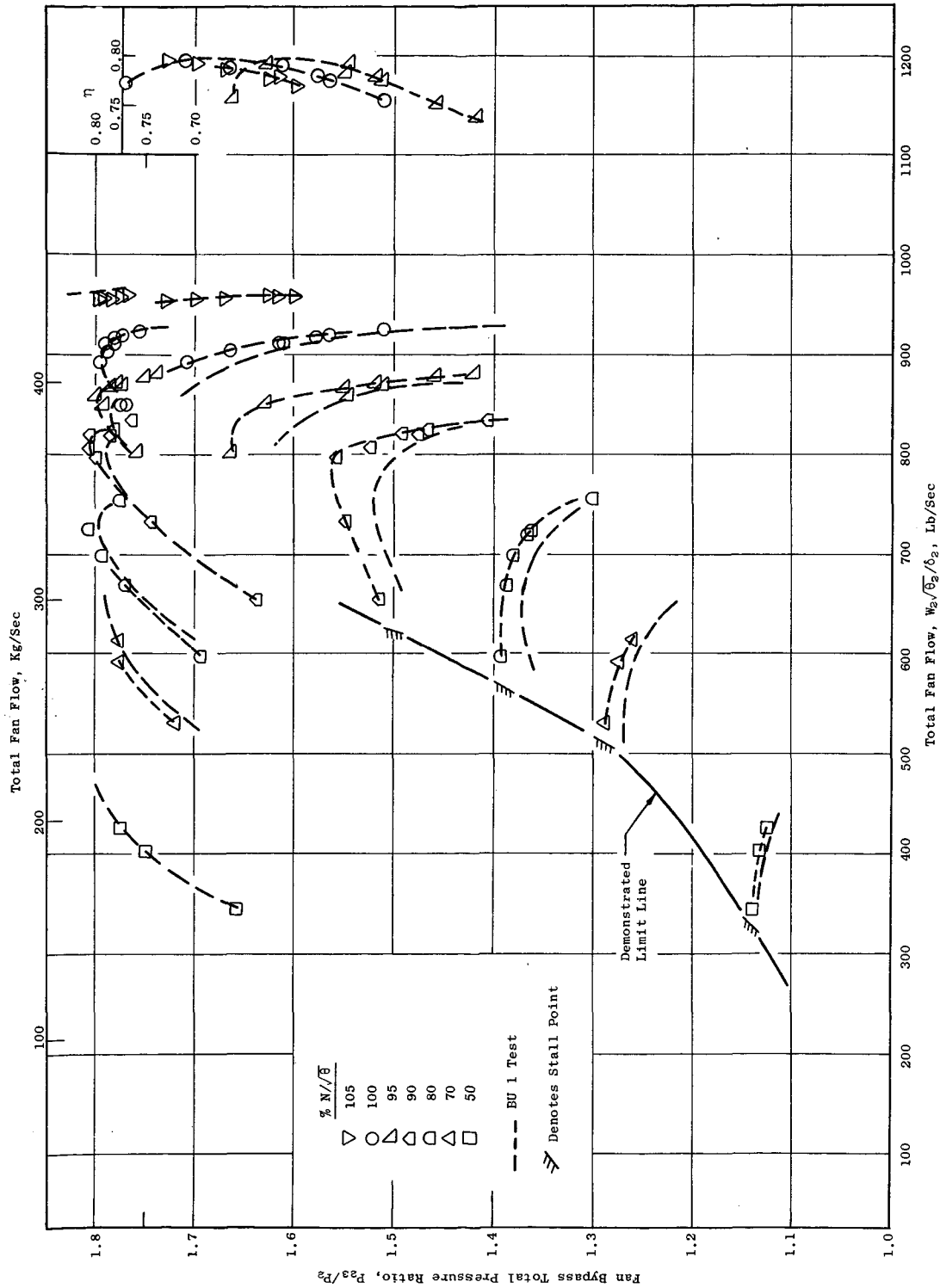


Figure 31. Build 2 Bypass Performance Map.

Hypothesizing that the poor performance of Build 1 at 100% corrected speed and lower was due to inadequate flow passing capability in the tip region because of an unstarted condition, a blade modification was made outboard of the part-span shroud; the shroud was located at 60% blade height. The modification increased the throat area by an average of about 1.2% over the region modified with the largest increase being 2% in the tip region. In addition, the area at the blade mouth (minimum distance from a blade leading edge to the adjacent blade suction surface) was reduced such that the internal contraction (ratio of blade throat to blade mouth area) was increased by an average of about 3% over the region modified with the largest increase being about 4% in the tip region. The internal contraction for the outer 20% of total fan flow, or 40% of the flow contained between the outer casing and the shroud, averaged 0.93. The throat area for the modified blade was still located in the aft region of the blade covered portion. This modification is referred to as Build 2.

Referring to Figure 31, the Build 2 bypass performance map, the measured design speed flow at the design pressure ratio of 1.60 was 915 lb/sec (415.0 kg/sec), the design value. At this point the adiabatic efficiency was 78.6%. A peak design speed efficiency of 79.0% was measured at a pressure ratio 1.68. At corrected speeds below 100%, the peak efficiency was generally about 80%. At the 105% corrected speed condition, the peak efficiency was 79.7% which occurred at a pressure ratio of 1.727. Thus, the only significant change in performance between the Build 1 and Build 2 configurations was a 2.6% reduction in peak efficiency at 105% corrected speed.

On test observation of the high response pressure pickups did not show the discontinuity that was observed on the Build 1 configuration. Analysis of the data at 100% corrected speed showed that the leading edge shock was moved further aft in the Build 2 configuration than in the Build 1 configuration. It was concluded, however, that a fully started condition on Build 2 had not been achieved at this speed.

The operational limit line was determined from 50 through 90% corrected speed. At each speed tested rotating stall was encountered at the operational limit line. The operating margin at 90% corrected speed relative to the design sea level static operating line is 27%.

Examination of the radial efficiency profiles for both Builds 1 and 2, additional discussion is presented on this item in the next section, showed a large hole relative to the expected profile. This apparent hole in the profile was centered at the location of the part-span shroud and was much larger than past experience would indicate as directly attributable to the combined profile and interference drags of the shroud. During the same time period, aero/acoustic testing of the part-span scale model Fan C, which also had a part-span shroud, was being conducted and performance problems similar to those of the full-scale Fan C vehicle were being encountered. It was decided to cut short the testing of the part-span scale model Fan C and to machine off the part-span shrouds. Testing of

this configuration showed large high speed efficiency gains. Accordingly, it was decided to machine off the part-span shrouds on the full size Build 2 Fan C configuration. In addition to removing the shroud the blade tip was twisted closed. The amount of twist was selected so as to somewhat more than compensate for the elastic untwist due to the removal of the shroud. The three considerations which resulted in the over-twist were: (1) clearanceometer data indicated that the tip of the shrouded blade was running more open than the design intent, (2) the energy input of the tip portion was greater than design, particularly for Build 2 since the modification resulted in an increase to the effective camber of the blade, and (3) a more closed tip was desirable from the standpoint of a stall or stress limit line without the shroud. This modification is referred to as Build 3.

Radial efficiency profiles for Build 1, Build 2, and Build 3 100% corrected speed lines, at two operating points corresponding to design and near peak efficiency, are presented in Figures 32 and 33. At both conditions the most significant difference between the three builds is the vast difference in efficiency over the middle portion of the annulus for Build 3. It can also be seen that for Builds 1 and 2 that the shroud noticeably influences the efficiency over a region corresponding to about 40% of the total fan flow. Since these radial efficiency profiles are determined at the discharge from the OGV, which makes the measurement plane approximately three true rotor chords axially removed from the rotor trailing edge, a significant amount of mixing and spreading of the shroud wake must have occurred. This indicates that the depth of the efficiency decrement at rotor exit is more severe than shown on the radial profile plots.

Figures 34, 35, and 36 show how the casing static pressure, for two of the static pressure taps over the rotor tip varies with corrected fan speed along a nominal operating line. The two taps are located 1.10 inches (27.9 mm) and 1.97 inches (50.0 mm) behind the design location of the rotor blade leading edge. At 100% corrected speed and below, the lower level of static pressure of Build 3 relative to Build 2 and of Build 2 relative to Build 1 is a direct result of the leading edge shock being located further aft in the cascade. The rapid drop in static pressure above 100% corrected speed for Builds 1 and 2 is a result of the shock being drawn back into the cascade. As previously discussed, a literal discontinuity was observed on Build 1 whereas no discontinuity was observed on Build 2. The Build 3 data shows that the transition of the shock back into the cascade was smooth and gradual, as expected.

#### TRAVERSE DATA

Traverse data at 100% corrected speed, at an operating point slightly below the design operating line, are presented in Figures 37 through 45. This type of data is used primarily to indicate flow profile trends; it is not used for performance computations. These data were recorded on Build 1; no traverse data were recorded for Build 2 or Build 3. Traverse data was taken at four axial planes; rotor inlet, rotor discharge, bypass OGV inlet and fan core OGV inlet. A major purpose for the traverses at two axial locations behind the rotor was the determination of any detrimental effects on the flow caused by the large axial gap between blade rows.

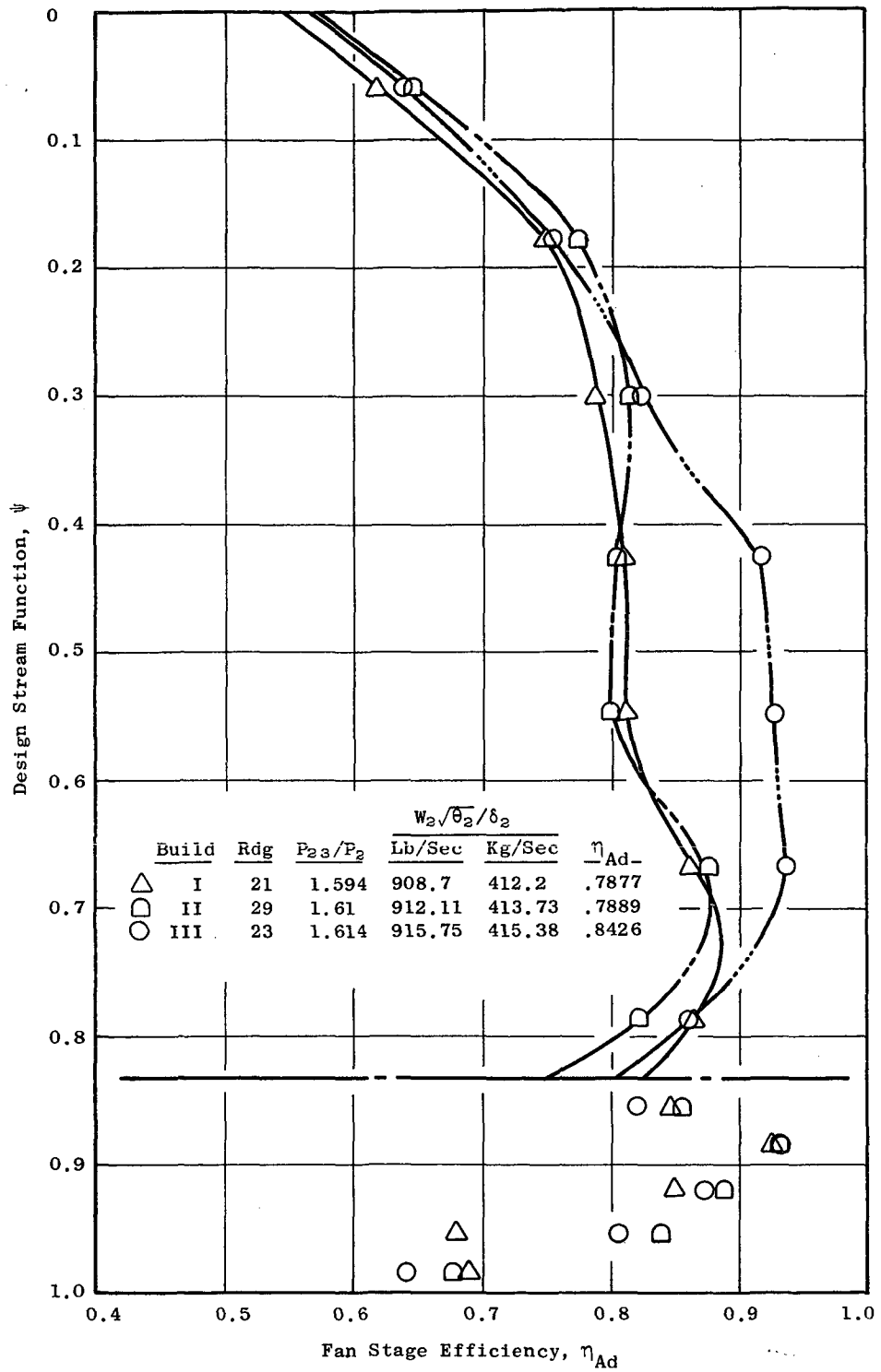


Figure 32. Radial Efficiency Profile for Builds 1, 2, and 3 (Near Design Point).

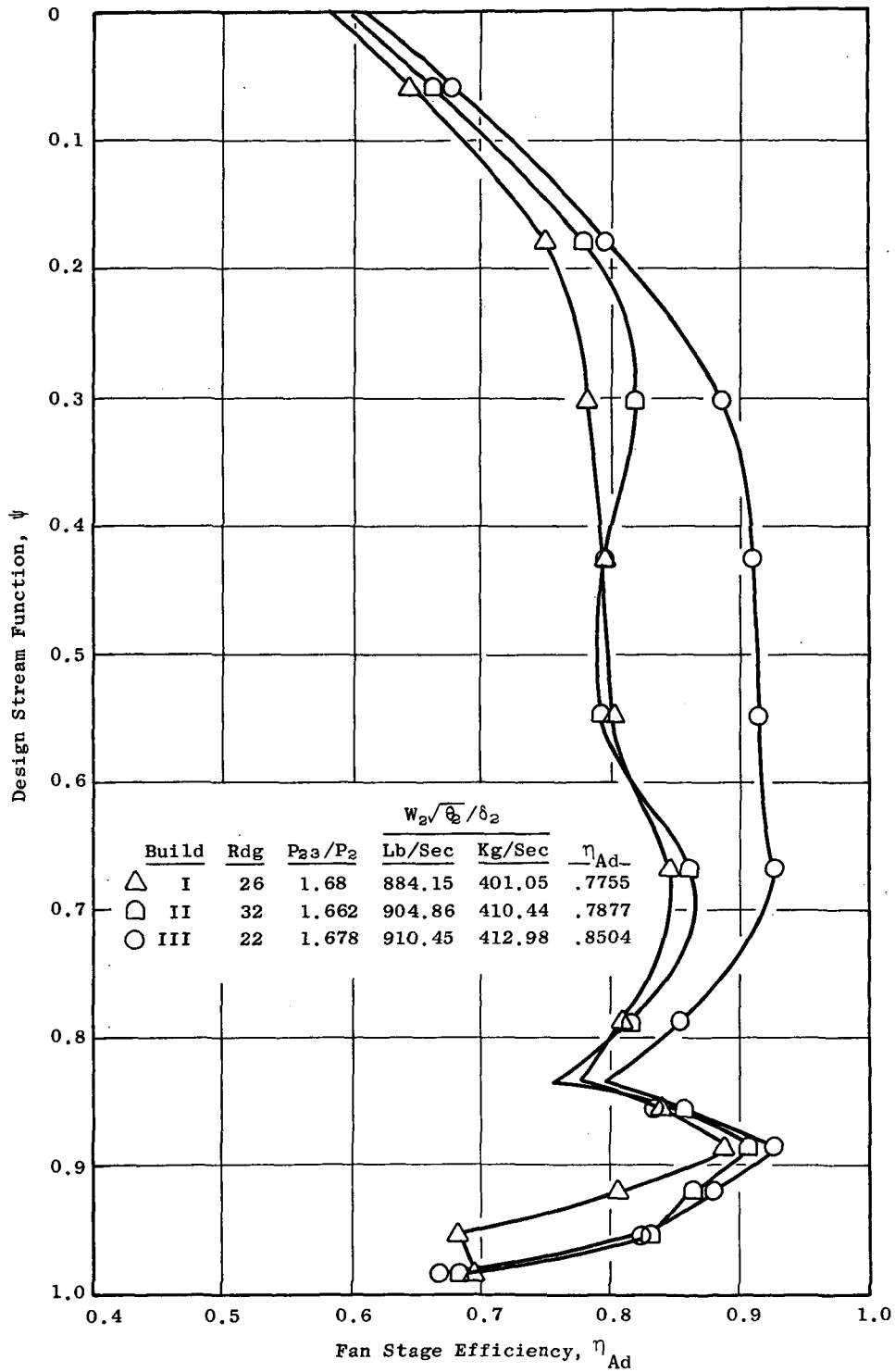


Figure 33. Radial Efficiency Profile for Builds 1, 2, and 3 (Throttled Above Design Point).

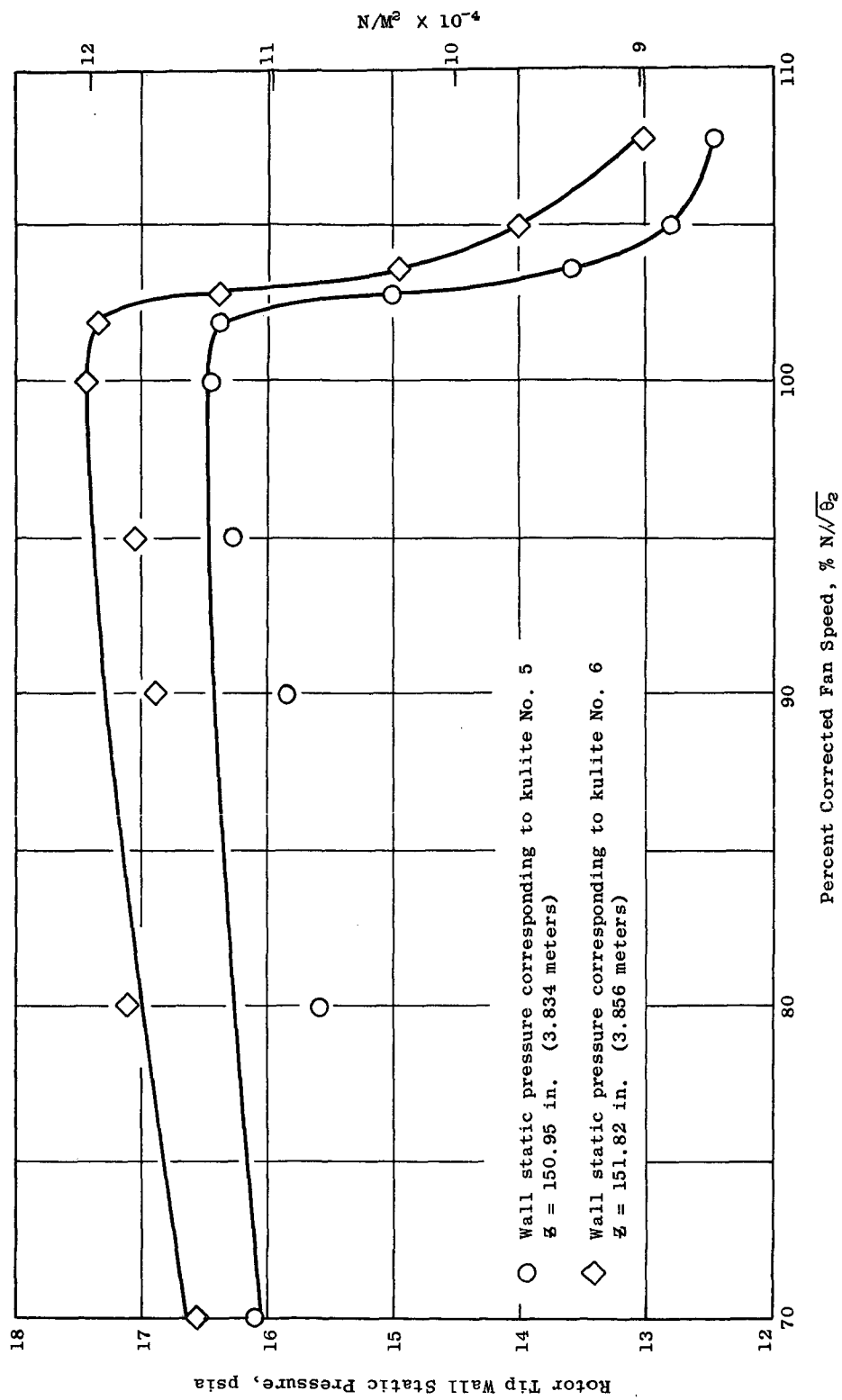


Figure 34. Rotor Tip Wall Static Profile Vs. Speed for Build 1.

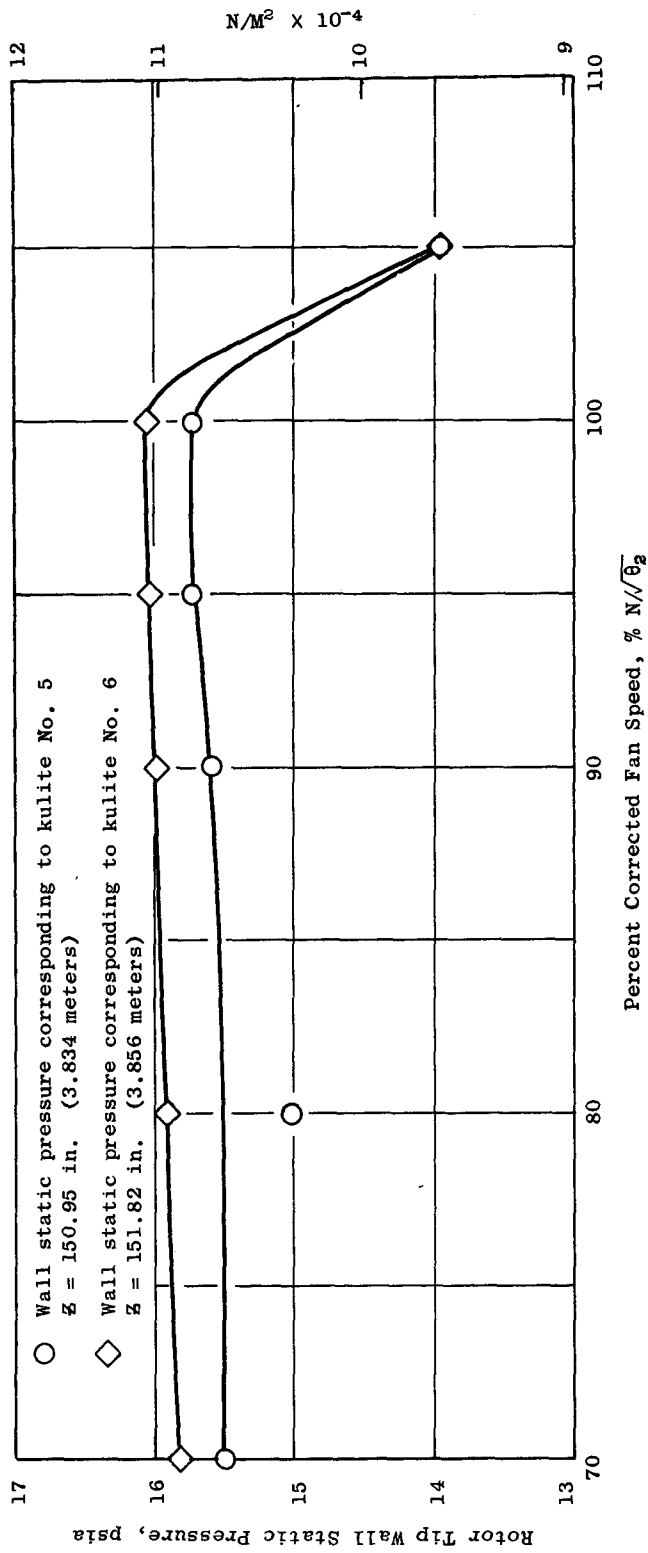


Figure 35. Rotor Tip Wall Static Profile Vs. Speed for Build 2.

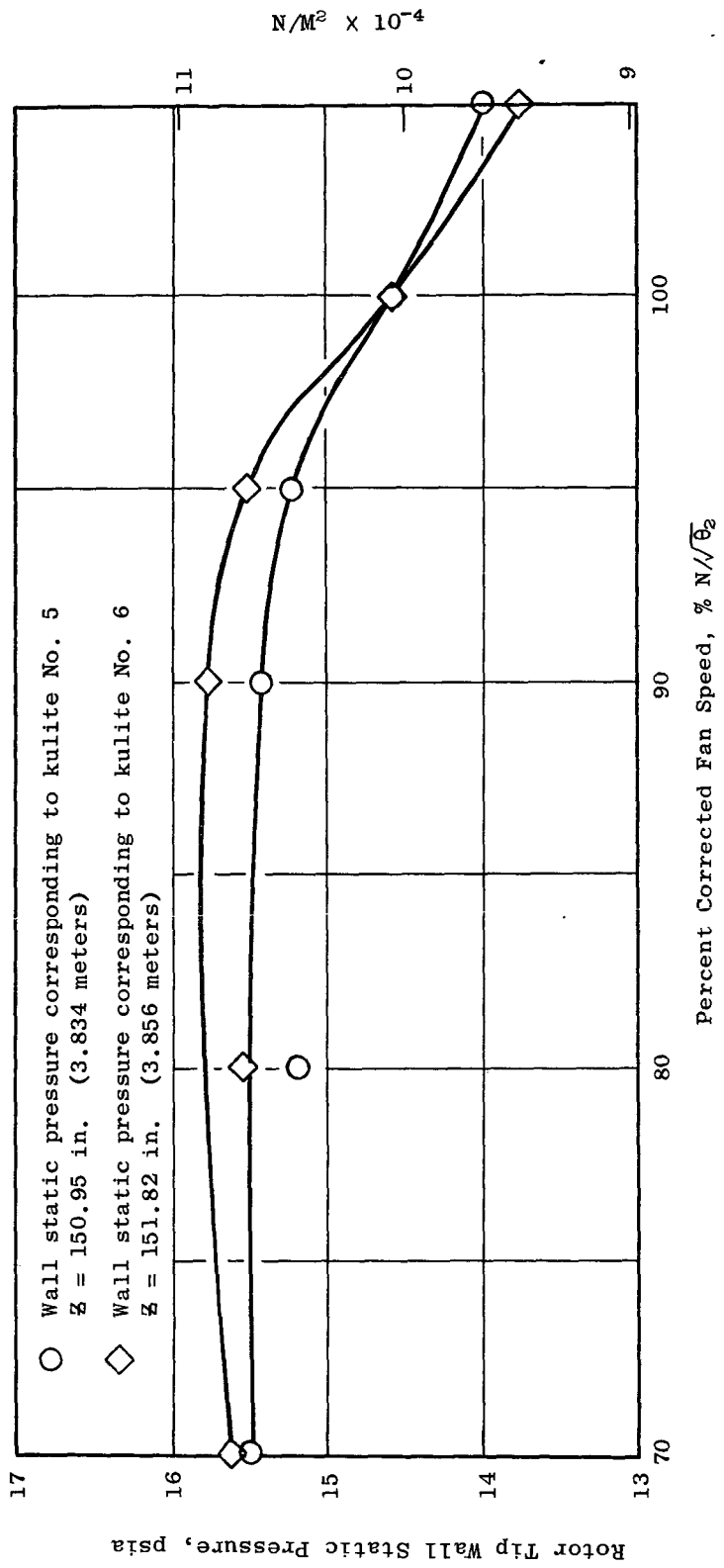


Figure 36. Rotor Tip Wall Static Profile Vs. Speed for Build 3.

$\% N/\delta_2$  100.08,  $P_{23}/P_2$  1.583,  $P_{24}/P_2$  1.505,  $W_2/\delta_2/\delta_2$  909.80 Lb/Sec  
 $(412.68$  Kg/Sec),  $\eta_{Ad23}$  77.52 %,  $\eta_{Ad24}$  80.59 %

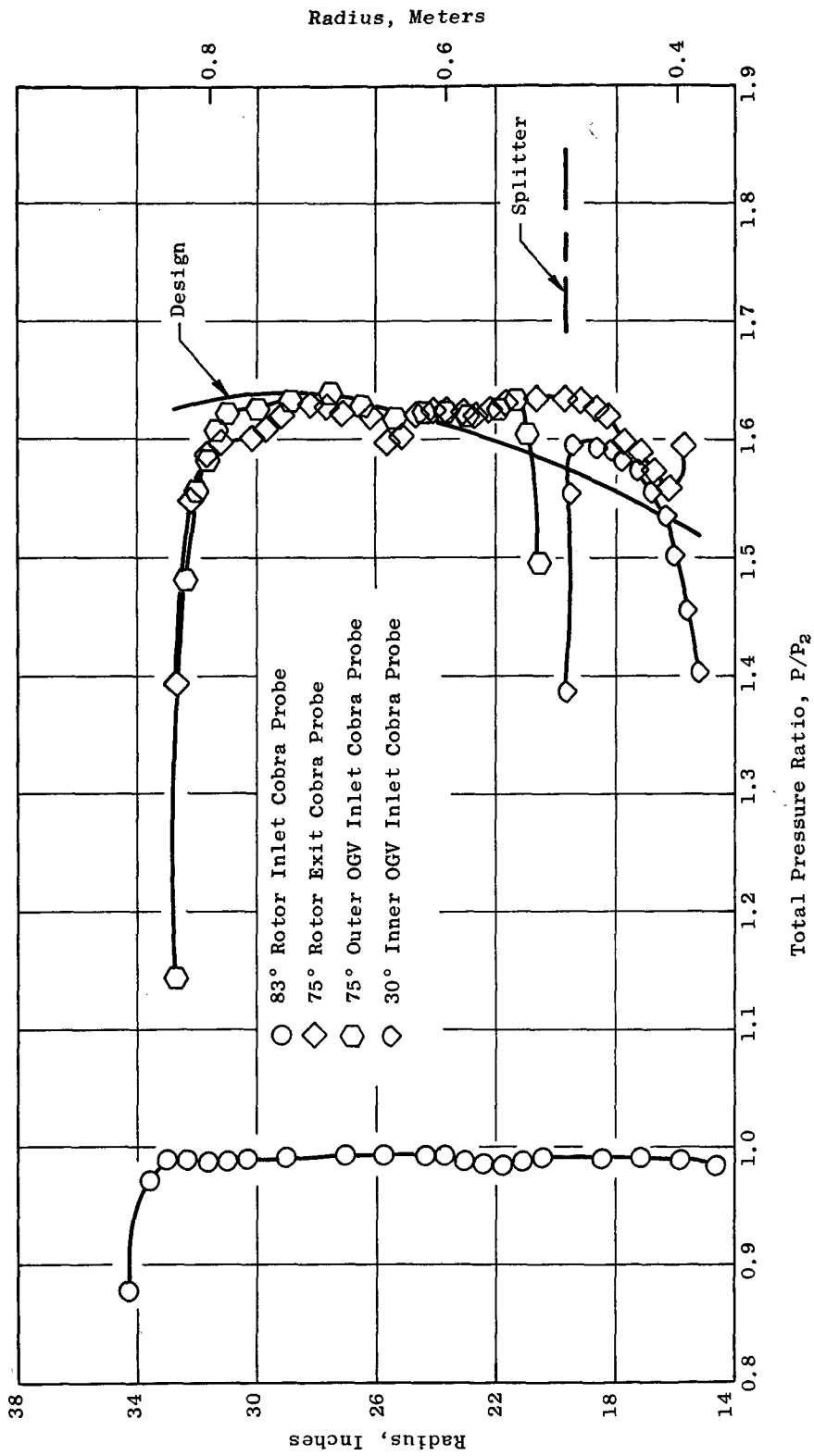


Figure 37. Traverse Radial Profiles, Radius Vs. Total Pressure Ratio (Bypass).

$\% N/\theta_2$  100.08,  $P_{23}/P_2$  1.583,  $P_{24}/P_2$  1.505,  $W_{27}/\theta_2/\theta_2$  909.80 Lb/Sec  
 $(412.68$  Kg/Sec),  $\eta_{Ad23}$  77.52 %,  $\eta_{Ad24}$  80.59 %

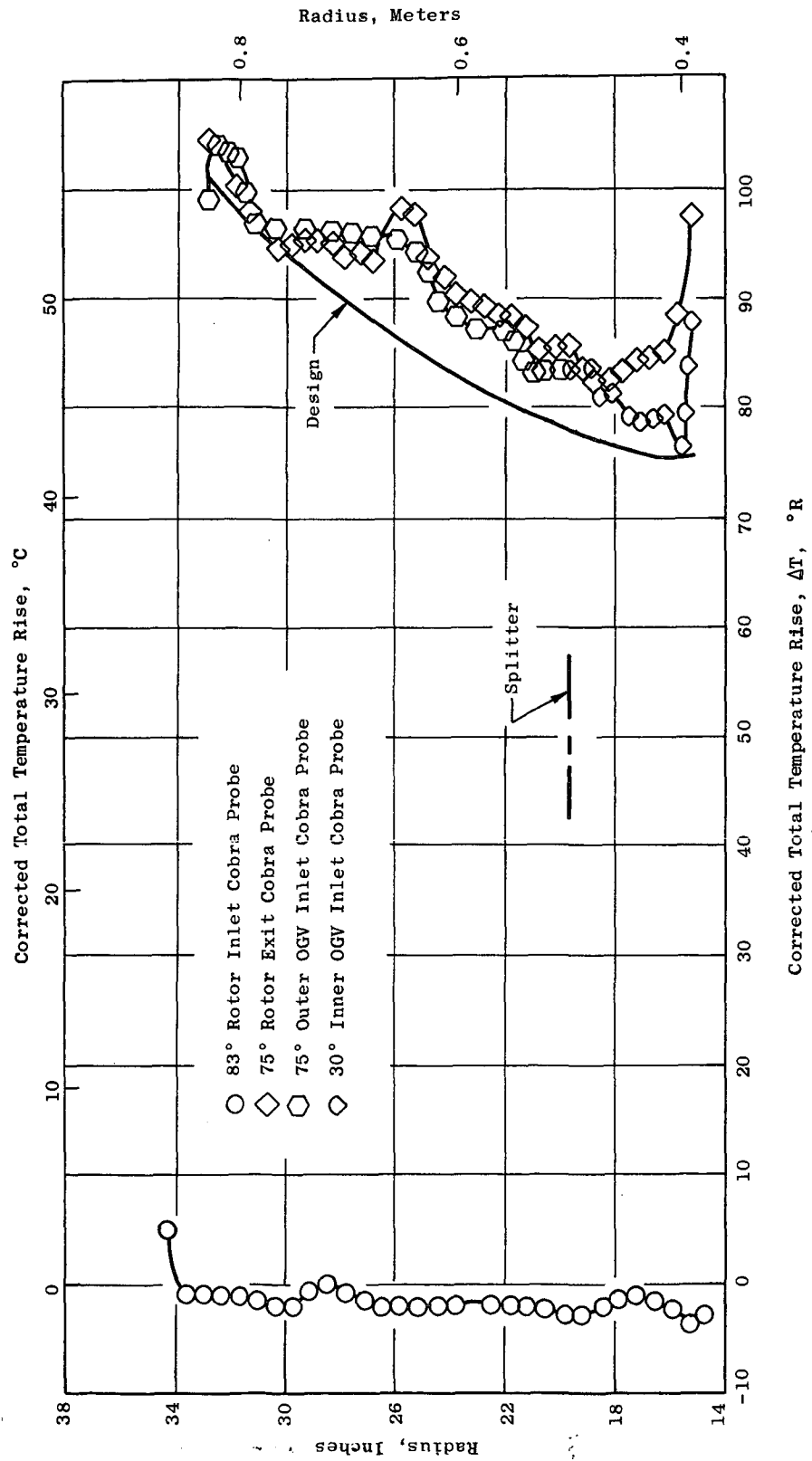


Figure 38. Traverse Radial Profiles, Radius Vs. Corrected Total Temperature Rise (Bypass).

$\% N/\sqrt{\theta_2}$  100.08,  $P_{23}/P_2$  1.583,  $P_{24}/P_2$  1.505,  $W_2/\sqrt{\theta_2/\theta_2}$  909.80 Lb/Sec  
 $(412.68$  Kg/Sec),  $\eta_{Ad_{23}}$  77.52 %,  $\eta_{Ad_{24}}$  80.59 %

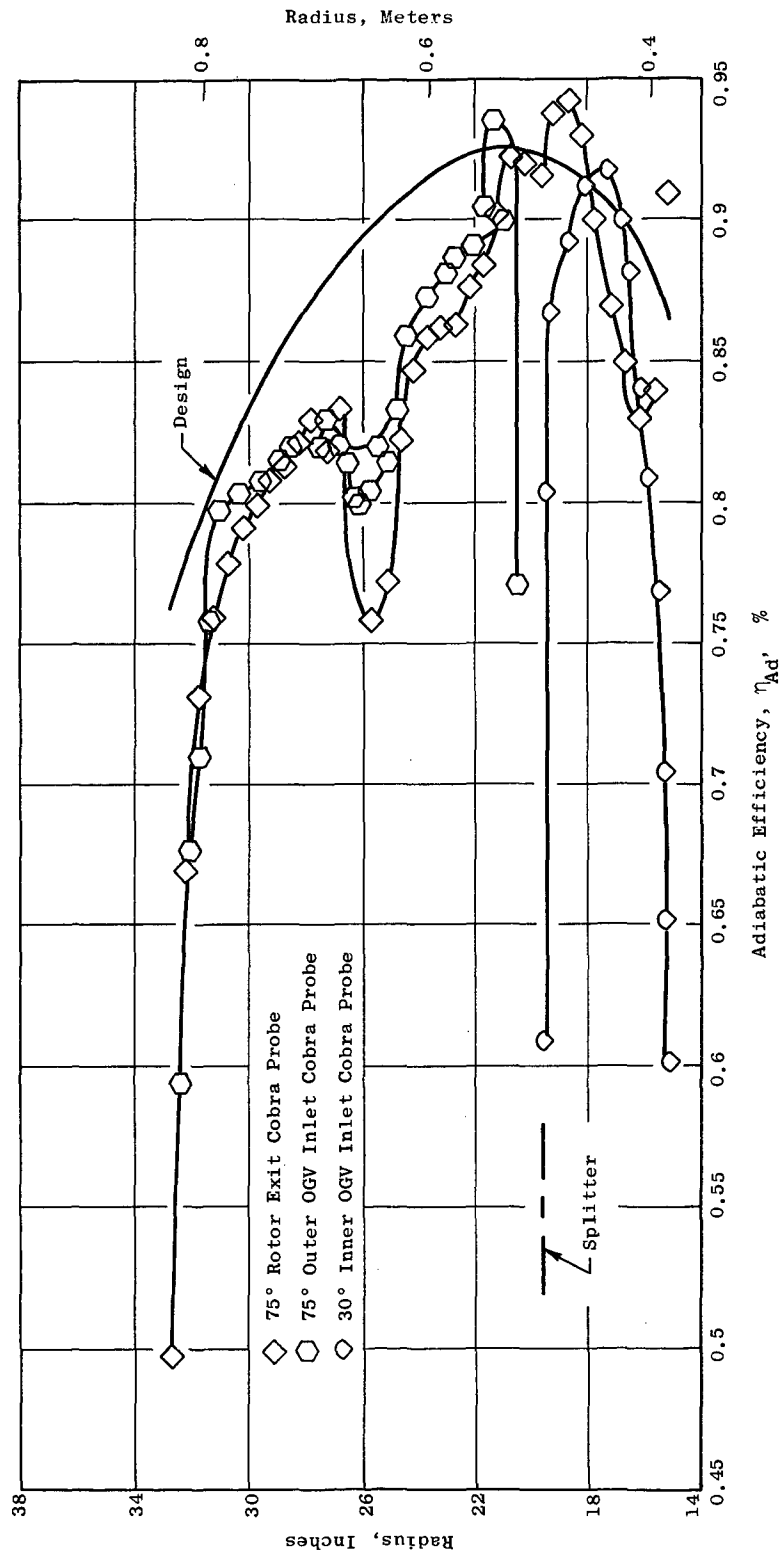


Figure 39. Traverse Radial Profiles, Radius Vs. Adiabatic Efficiency (Bypass).

$\% N/\sqrt{\theta_2}$  100.08,  $P_{23}/P_2$  1.583,  $P_{24}/P_2$  1.505,  $W_p/\theta_2/b_2$  909.80 Lb/Sec  
 (412.68 Kg/Sec),  $\eta_{Ad_{23}}$  77.52 %,  $\eta_{Ad_{24}}$  80.59 %

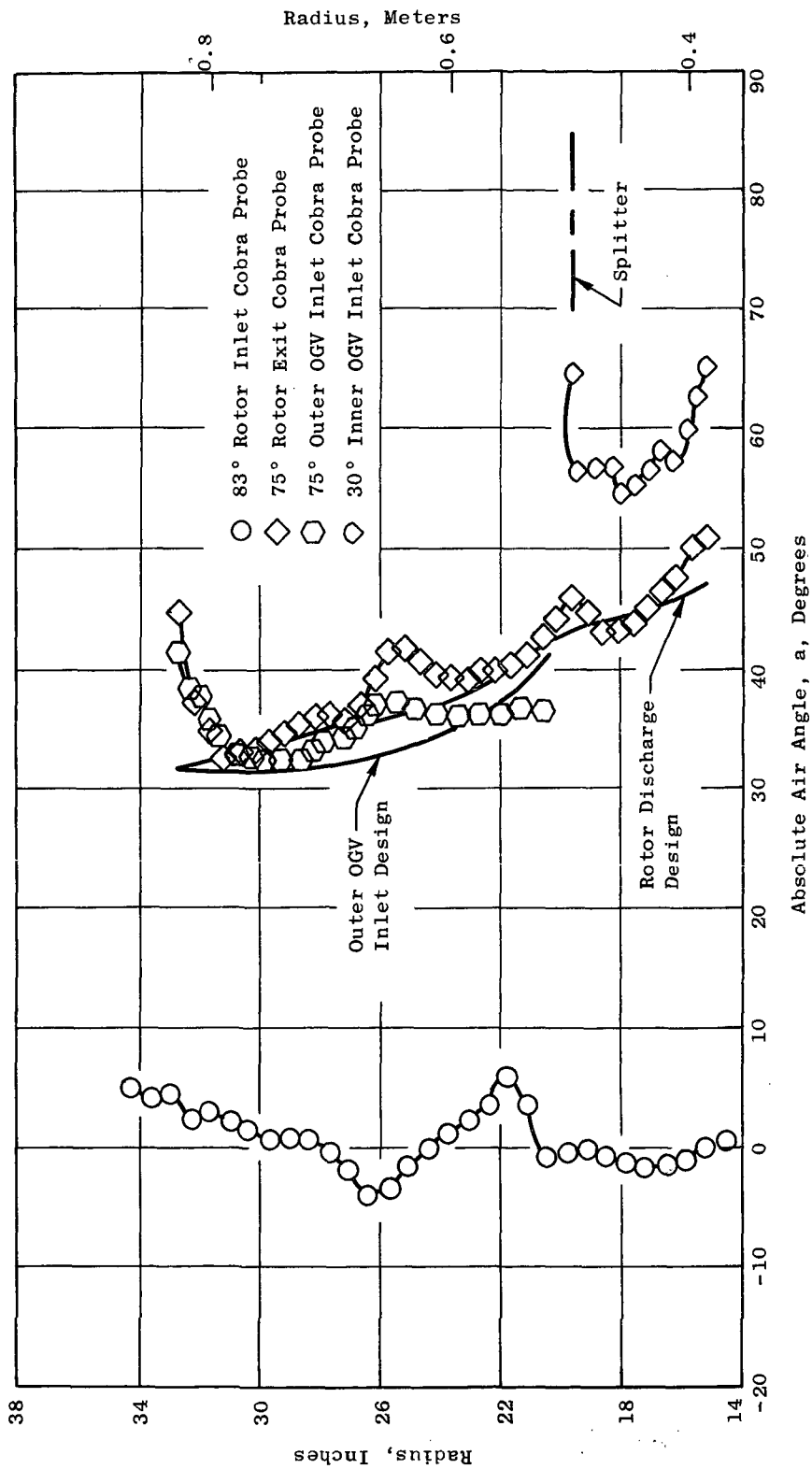


Figure 40. Traverse Radial Profiles, Radius Vs. Absolute Air Angle (Bypass).

$\% N/\theta_2$  100.08,  $P_{23}/P_2$  1.583,  $P_{24}/P_2$  1.505,  $W_2/\theta_2/\delta_2$  909.80 Lb/Sec  
 $(412.68 \text{ Kg/Sec})$ ,  $\eta_{Ad_{23}}$  77.52  $\%$ ,  $\eta_{Ad_{24}}$  80.59  $\%$

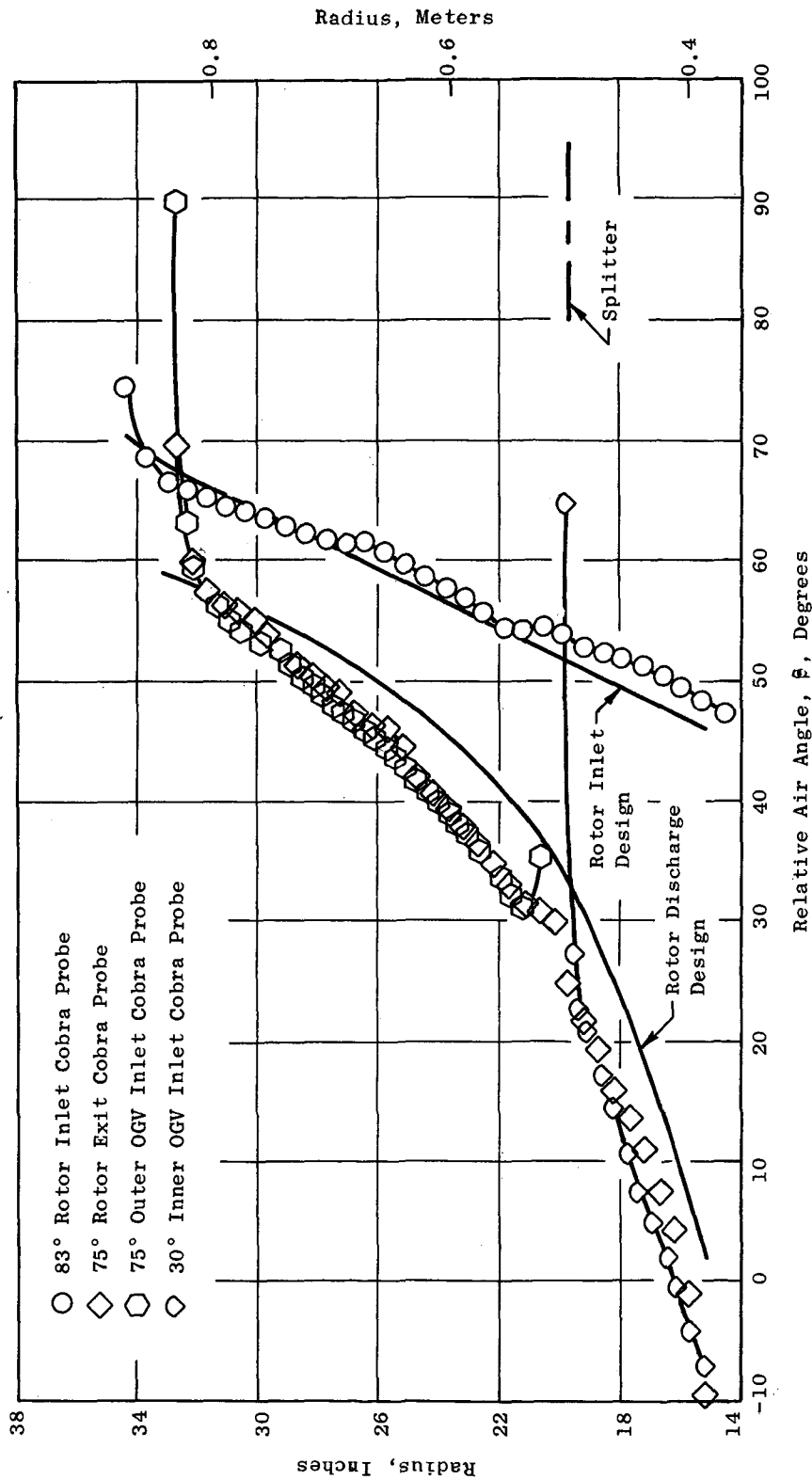


Figure 41. Traverse Radial Profiles, Radius Vs. Relative Air Angle (Bypass).

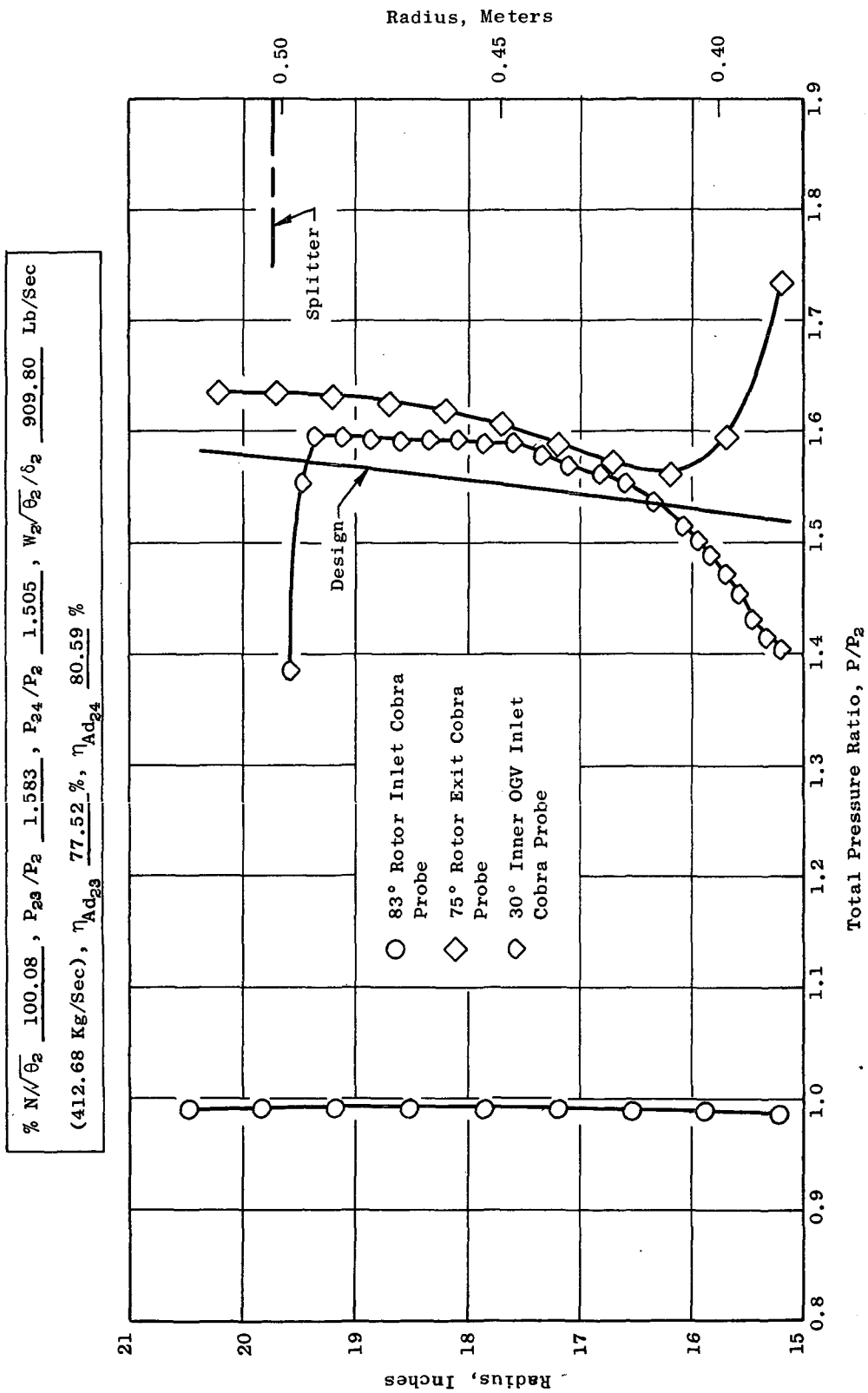


Figure 42. Traverse Radial Profiles, Radius Vs. Total Pressure Ratio (Core).

$\% N/\theta_2$  100.08,  $P_{23}/P_2$  1.583,  $P_{24}/P_2$  1.505,  $W_2/\theta_2/\delta_2$  909.80 Lb/Sec  
 (412.68 Kg/Sec),  $\eta_{Ad_{23}}$  77.52 %,  $\eta_{Ad_{24}}$  80.59 %

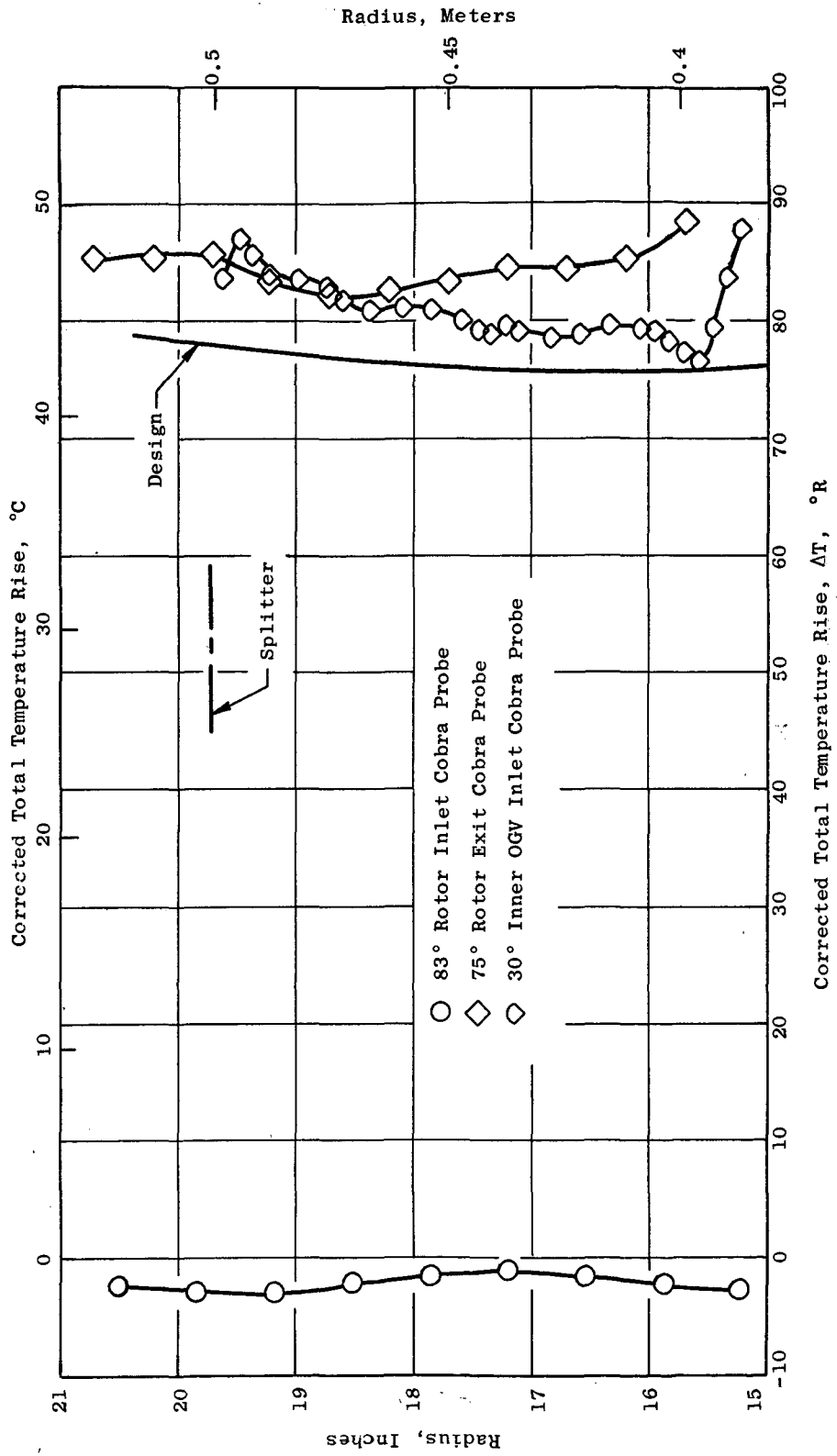


Figure 43. Traverse Radial Profiles, Radius Vs. Corrected Total Temperature Rise (Core).

$\% N/\sqrt{\theta_2}$  100.08,  $P_{23}/P_2$  1.583,  $P_{24}/P_2$  1.505,  $W_2/\sqrt{\theta_2}/\delta_2$  909.80 Lb/Sec  
 $(412.68$  Kg/Sec),  $\eta_{Ad23}$  77.52 %,  $\eta_{Ad24}$  80.59 %

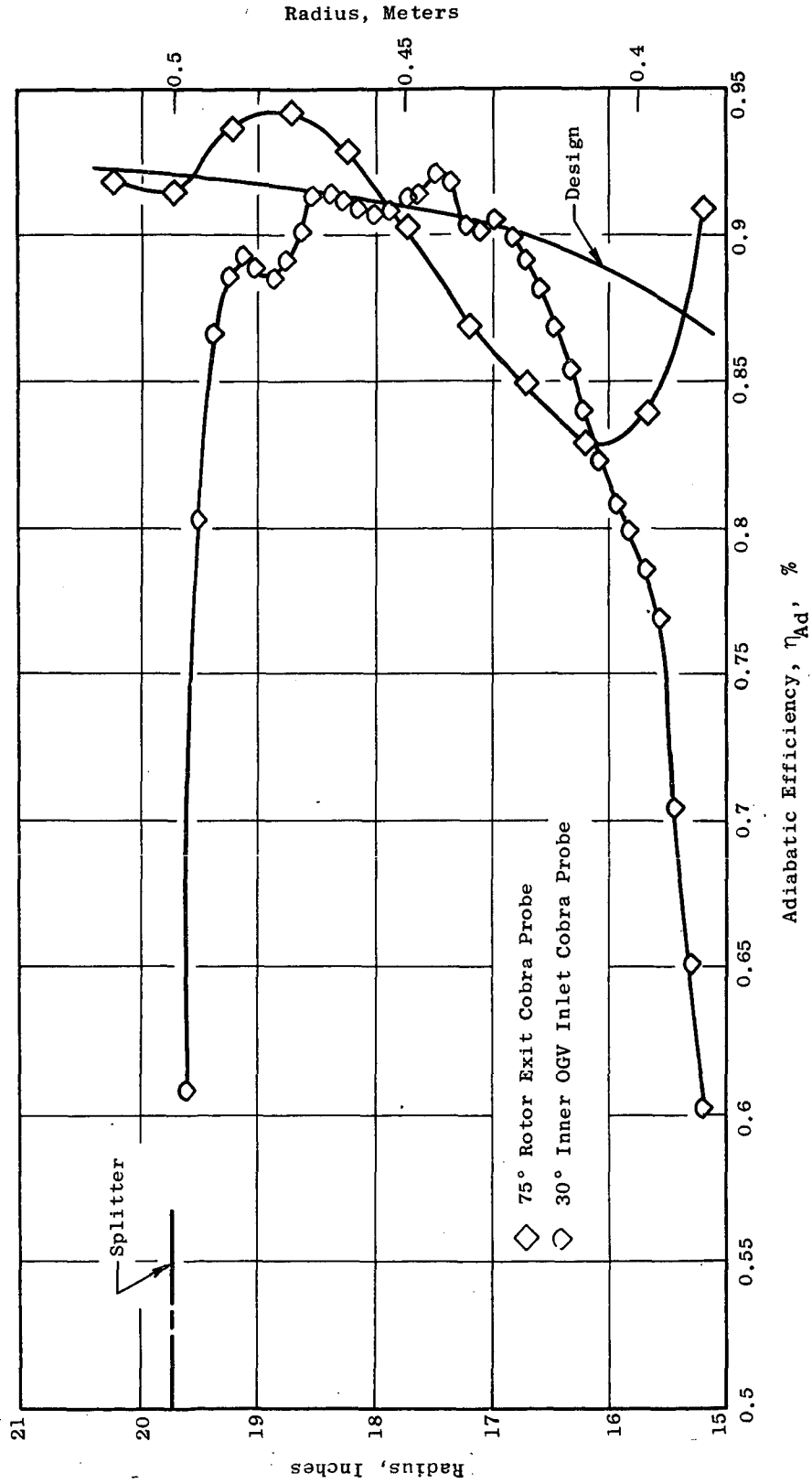


Figure 44. Traverse Radial Profiles, Radius Vs. Adiabatic Efficiency (Core).

$\% N/\theta_2$  100.08,  $P_{23}/P_2$  1.583,  $P_{24}/P_2$  1.505,  $W_2/\theta_2/b_2$  909.80 Lb/Sec  
 (412.68 Kg/Sec),  $\eta_{Ad23}$  77.52 %,  $\eta_{Ad24}$  80.59 %

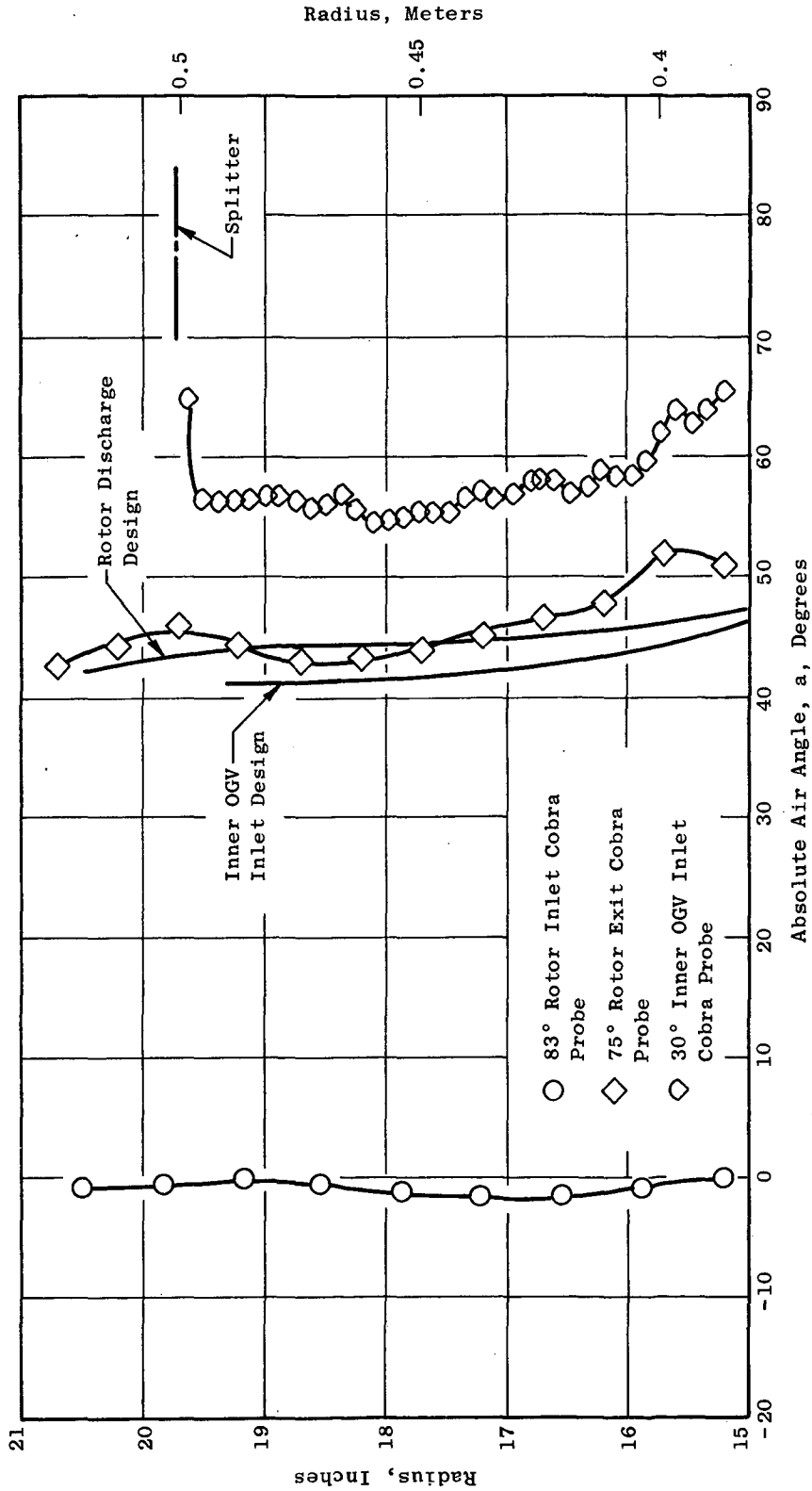


Figure 45. Traverse Radial Profiles, Radius Vs. Absolute Air Angle (Core).

The total pressure traverse data show that a significant growth in wall boundary layer occurs between the fan rotor exit and the OGV inlet which is probably due to the large axial space that was incorporated, for acoustic reasons, between the two rows of blades. The discrepancy in the temperature measurements between the two probes in the core region is unexplained. Comparison with the fixed discharge information, which is believed more reliable, indicates that the lower of the two readings is more correct. The efficiency profile shows a significantly deeper wake from the part-span shroud at rotor exit than at OGV inlet. As was hinted at in an earlier discussion, the radial depth of what appears to be directly associated with the drag on the shroud is typical of past experience. However, what appears to be an abnormally low efficiency level for a region not directly affected by the shroud extends over a large portion of the annulus. The absolute air angle measured at the core OGV inlet appears out of line on the high side. The rotor relative exit air angle, as computed from the traverse measurements, indicate a significant overturning by the rotor except locally in the rotor tip region. This is consistent, in trend, with the traverse probe and fixed instrumentation total-temperature measurements that show more temperature rise across the rotor than design intent.

#### BYPASS RATIO EXCURSION

Tolerance of the fan to off-design bypass ratio operation was systematically investigated as a part of the test investigation on Fan C. This investigation was performed on Build 2 and is believed representative of the configuration, independent of the build, since no significant changes were made to the parameters which would logically be expected to affect performance deltas during off-design bypass ratio operations. A fan corrected speed of 90% was selected as representative, and for a bypass discharge valve setting of 34, representative of the nominal operating line, readings were taken at five fan core portion discharge valve settings. The overall performance maps are shown in Figures 46 and 47. For increased bypass ratios, Figure 47 shows that the core portion suffers large efficiency losses while the bypass portion (Figure 46) loses only moderately. This is a result of the fact that, in order to simulate engine operation, only the core discharge value was varied. At the highest bypass ratios the core portion incidence angles and diffusion factors were significantly greater than their design values, particularly for the outlet guide vanes, and the splitter was subjected to a high enough incidence to cause high losses on its upper surface, implying flow separation there.

To aid in the understanding of these effects, the stage and rotor efficiencies OGV total-pressure-loss, and static-pressure-rise coefficients were computed as described in Appendix II, for selected arc rake immersions, of the bypass ratio investigation. The results of these computations are shown in Figures 48 through 54. The immersion for each of the figures is identified in terms of its design stream function, 0 being the OD, 0.83 being the splitter, and 1.0 being the ID. Referring to Figures 48 through 50, which correspond to

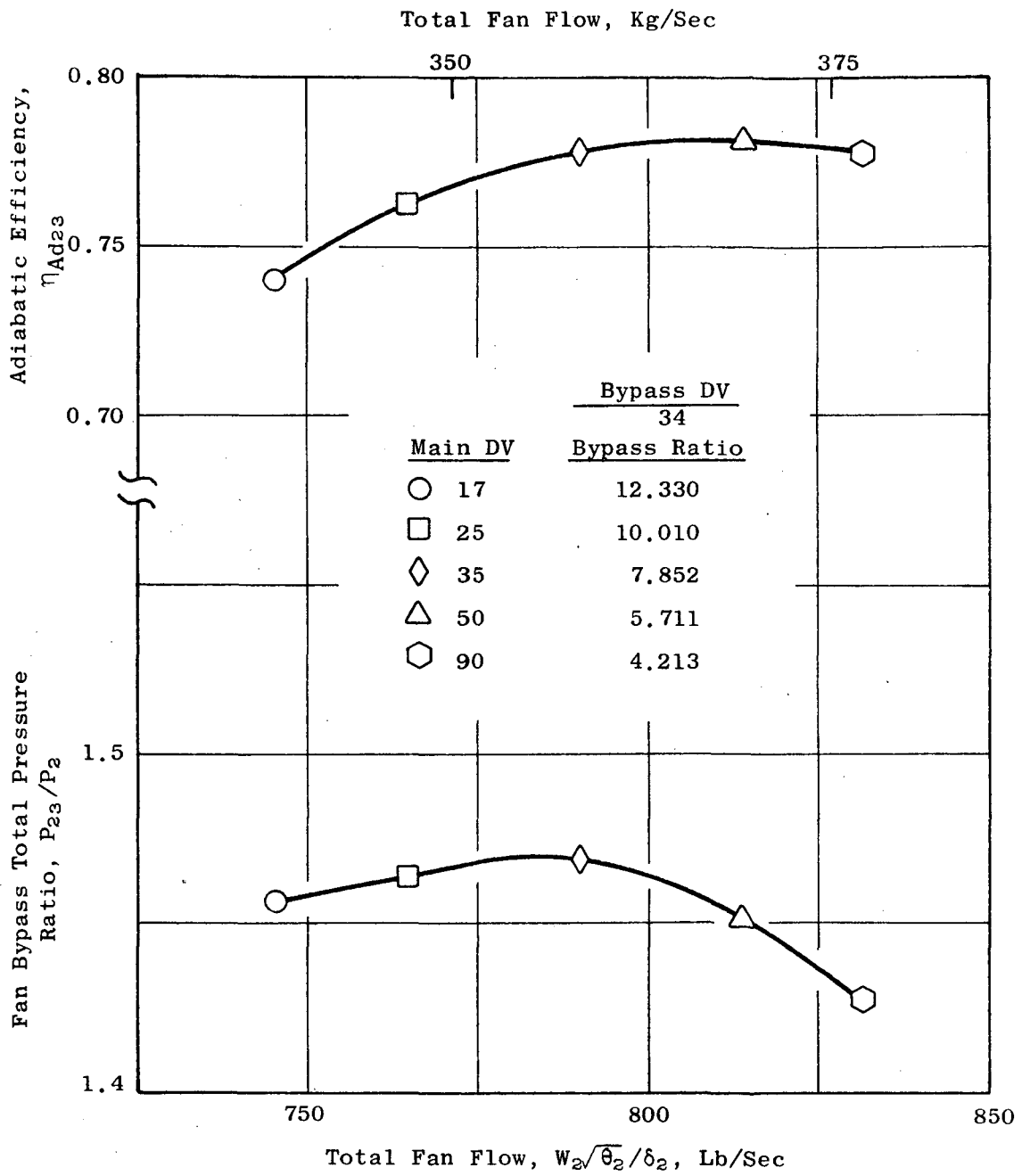


Figure 46. Bypass Ratio Excursion, Bypass Performance.

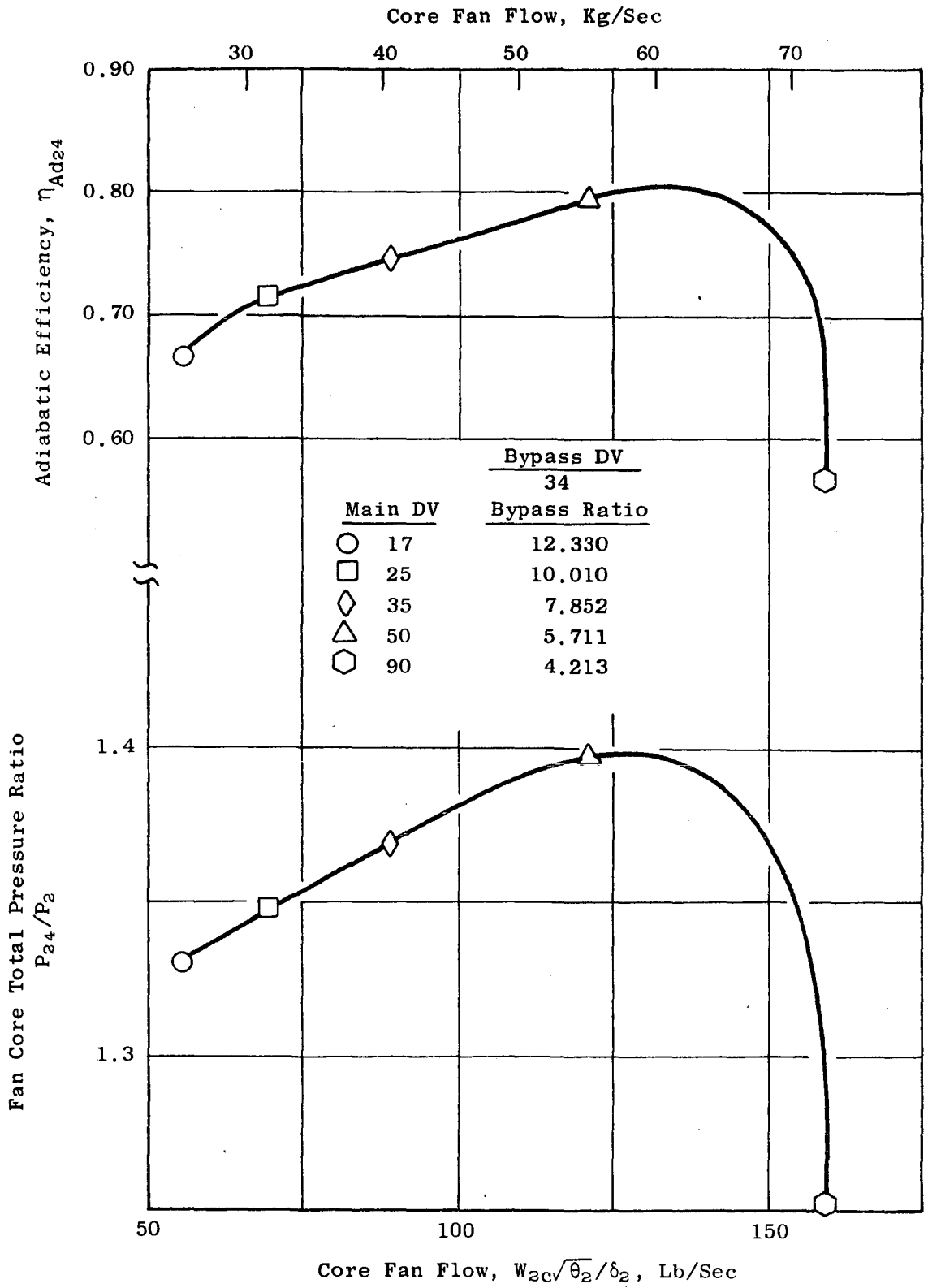


Figure 47. Bypass Ratio Excursion, Core Performance.

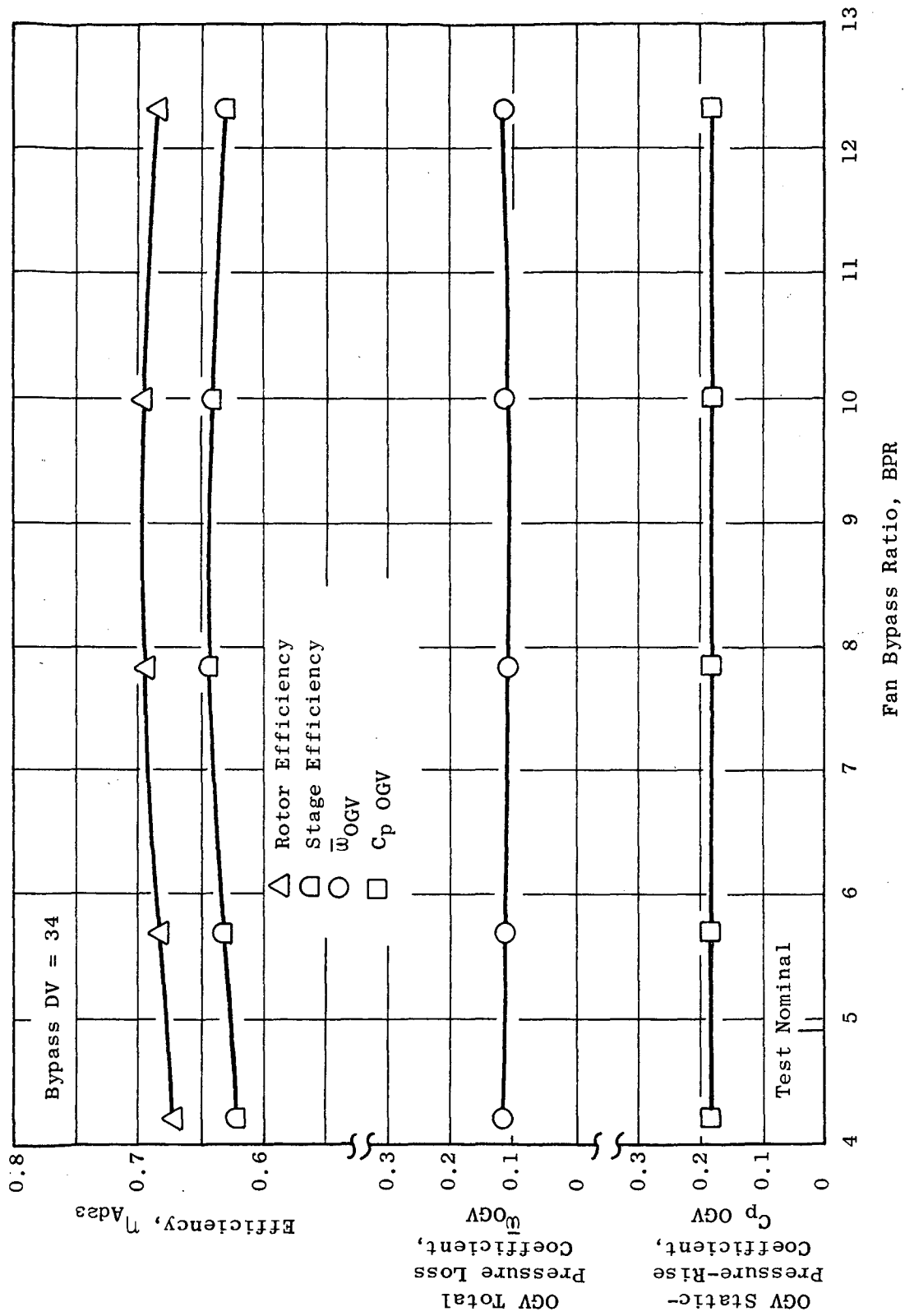


Figure 48. Variation of Element Properties with Bypass Ratio, Design Stream Function = 0.059 (Bypass OD).

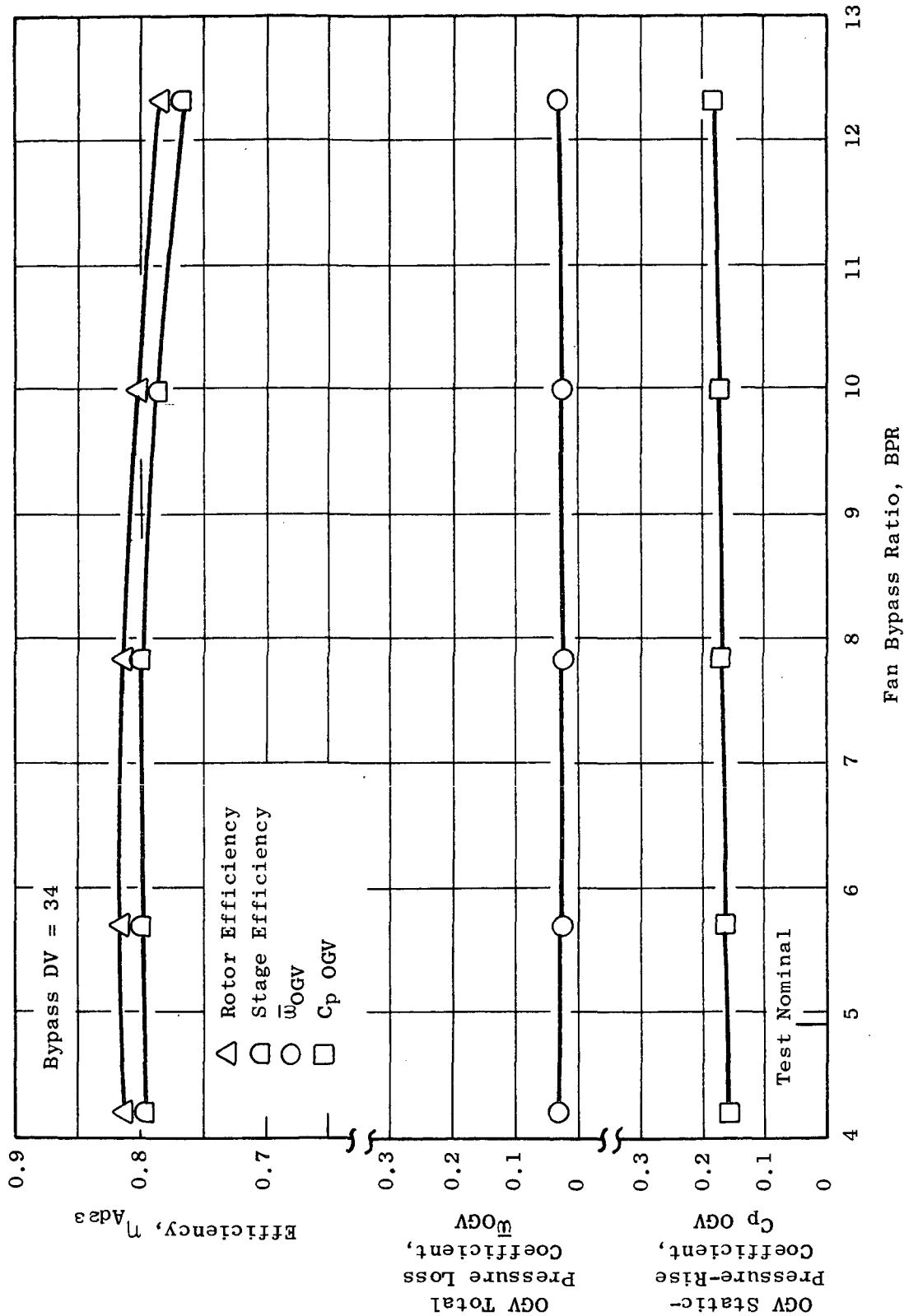


Figure 49. Variation of Element Properties with Bypass Ratio, Design Stream Function = 0.303.

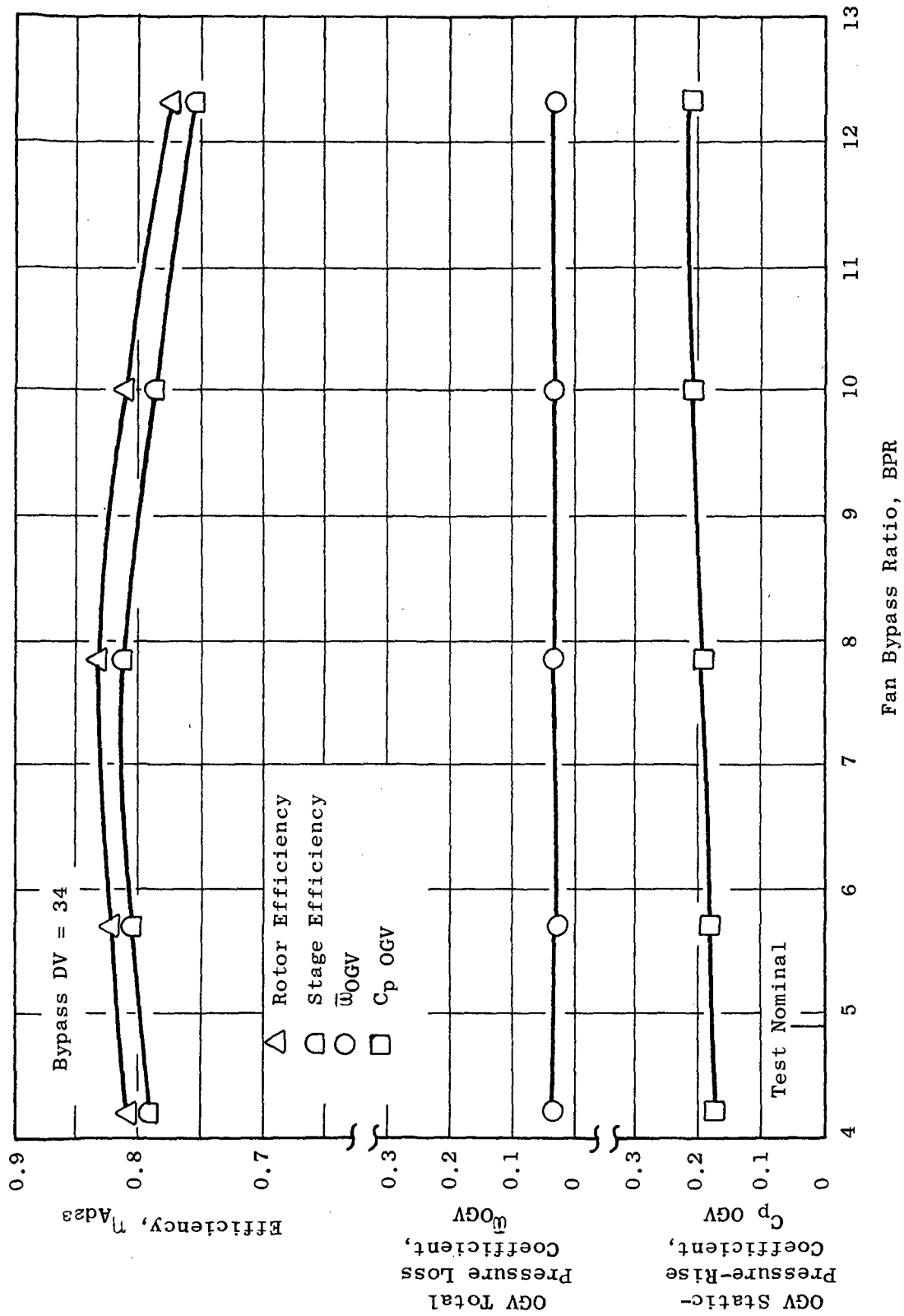


Figure 50. Variation of Element Properties with Bypass Ratio, Design Stream Function = 0.548.

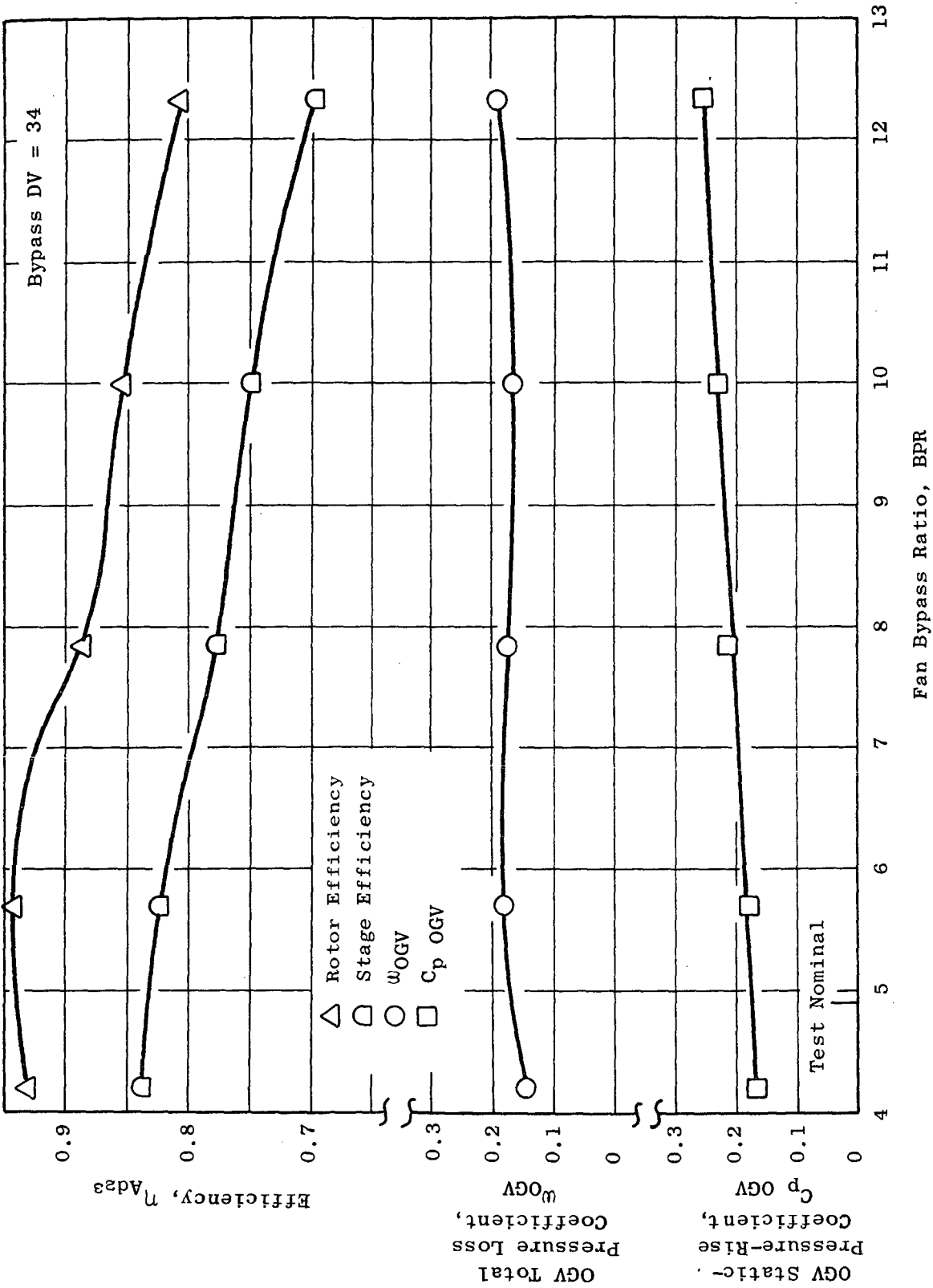


Figure 51. Variation of Element Properties with Bypass Ratio, Design Stream Function = 0.787 (Bypass ID).

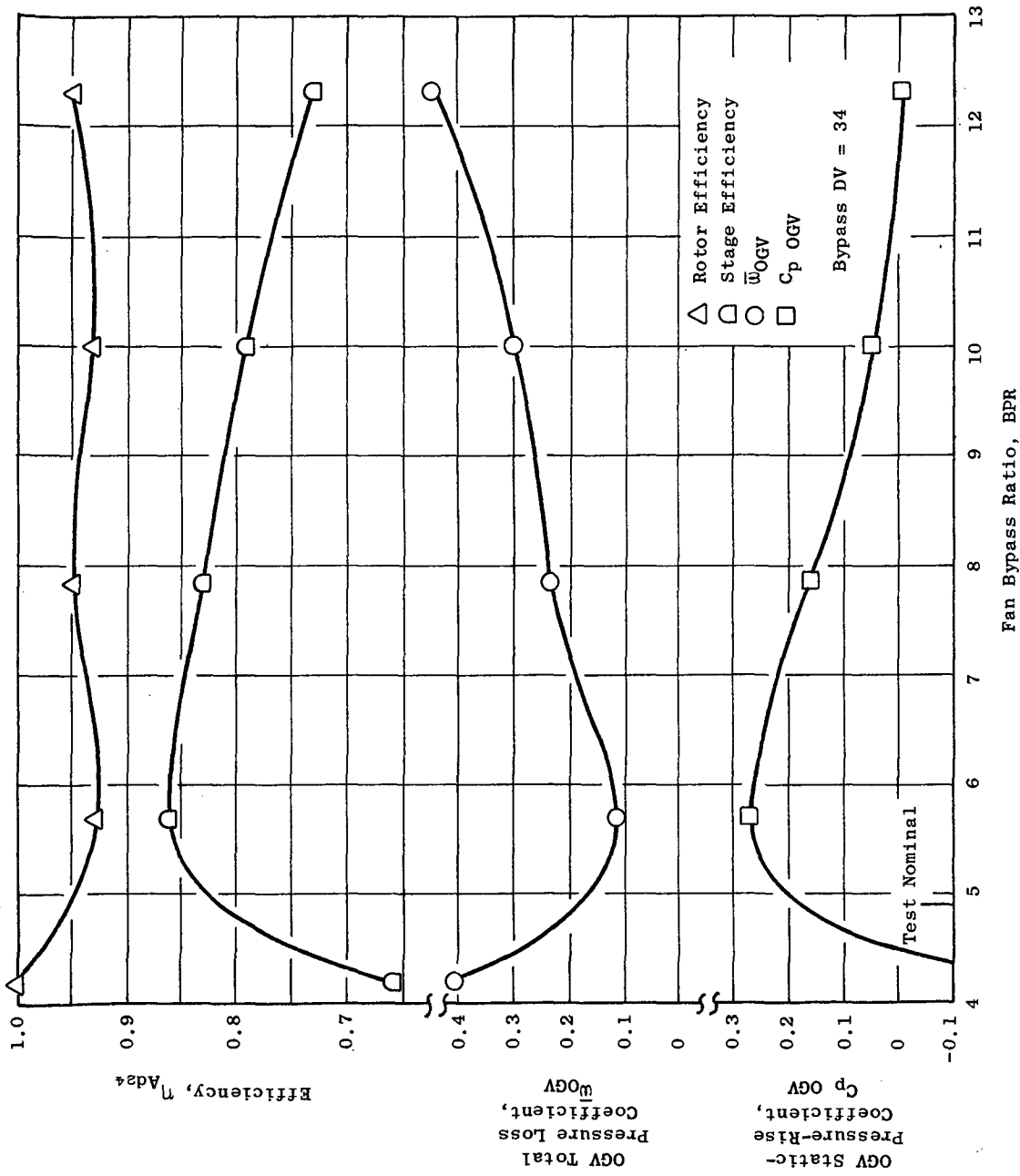


Figure 52. Variation of Element Properties with Bypass Ratio, Design-Stream Function = 0.855 (Core OD).

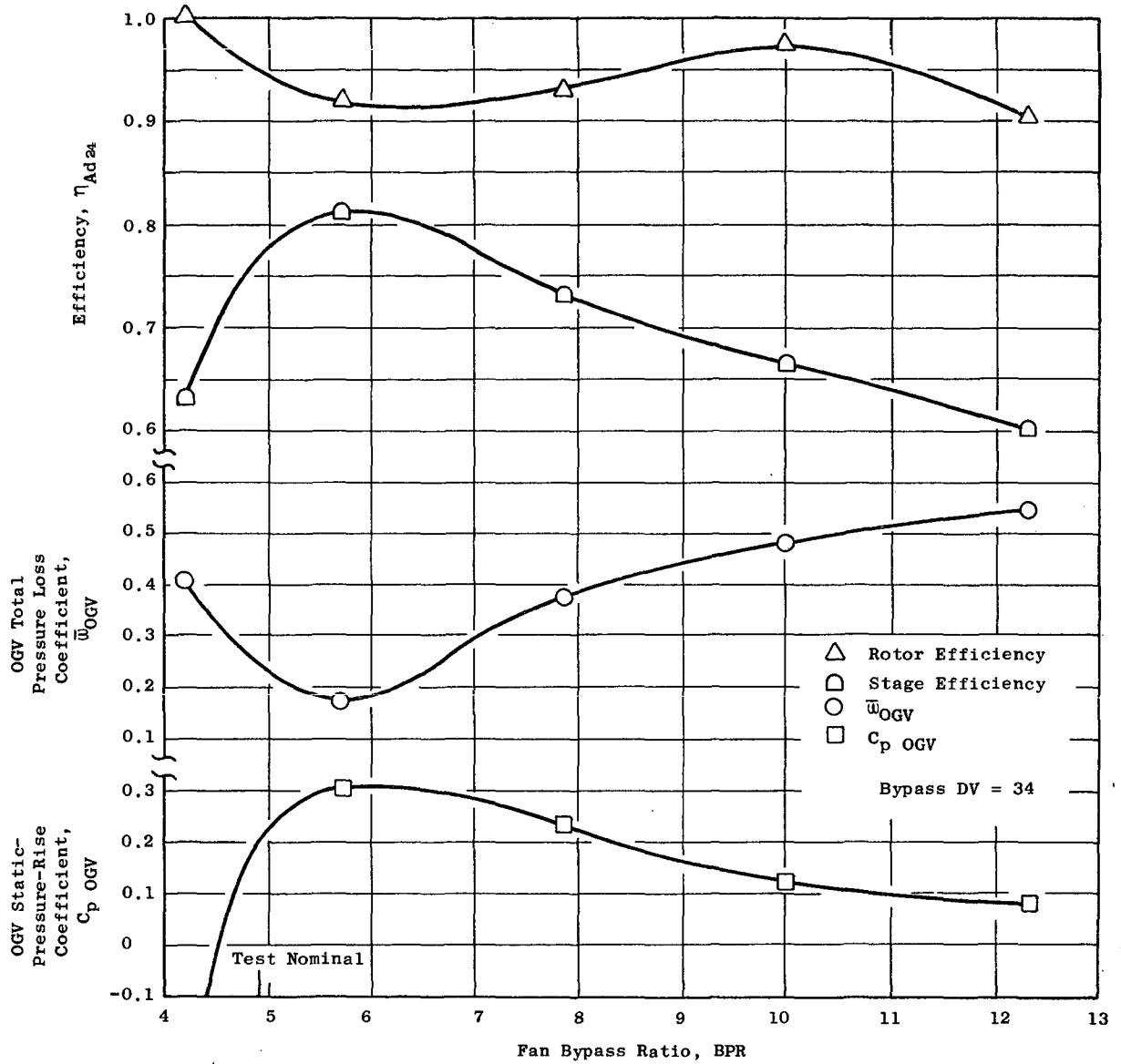


Figure 53. Variation of Element Properties with Bypass Ratio, Design Stream Function = 0.953.

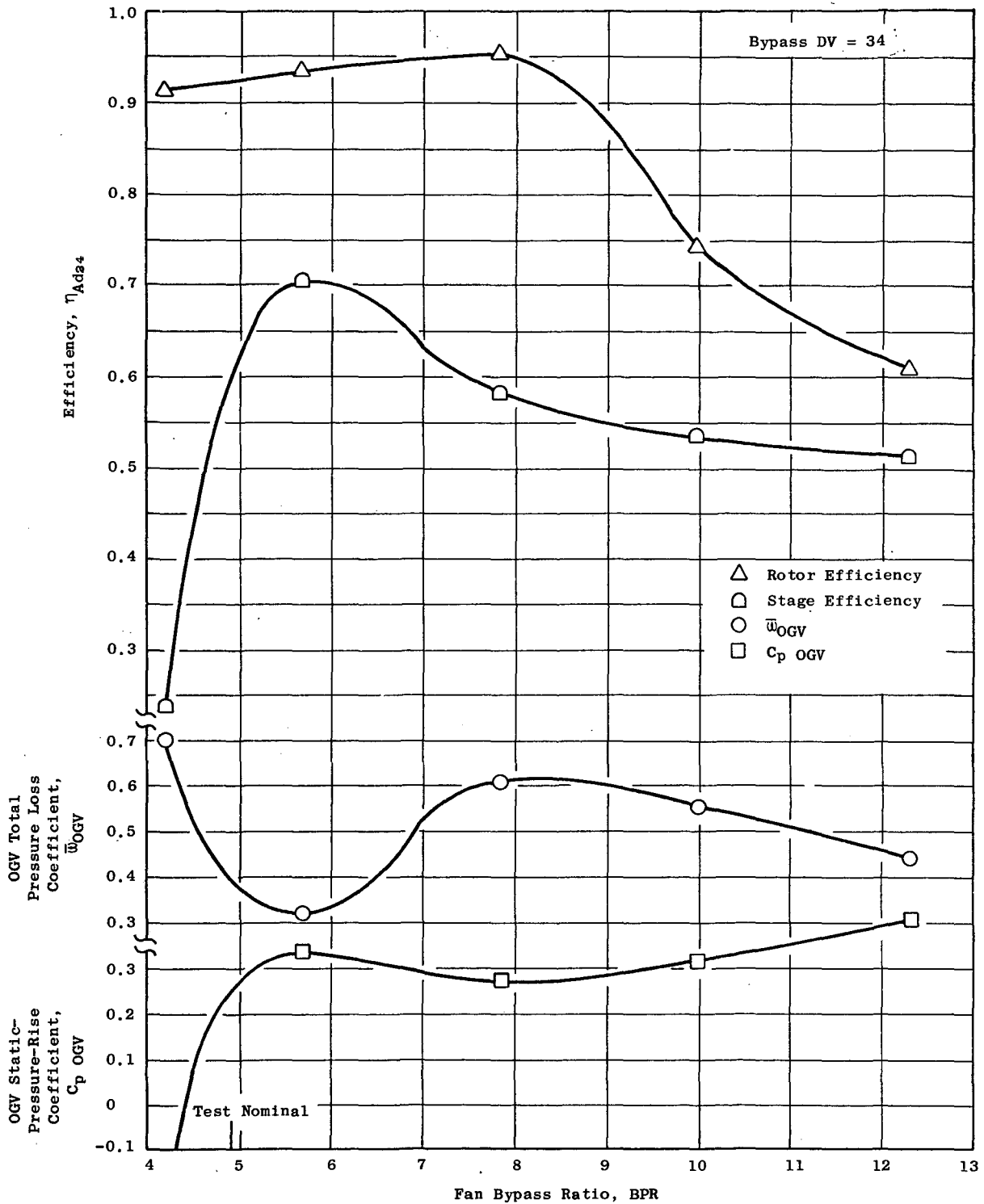


Figure 54. Variation of Element Properties with Bypass Ratio, Design Stream Function = 0.984 (Core ID).

the majority of the bypass flow, only very modest changes to stage and rotor efficiency and OGV total-pressure-loss and static-pressure-rise coefficients are observed. This indicates that the bypass configuration is tolerant to bypass ratio migrations, at least over the range tested, and that no significant flow breakdown occurs. (An exception to this is the drop in rotor and stage efficiency observed in the bypass ID immersion, Figure 51, for the higher bypass ratio points. Discussion of this item is given later in this section). Referring to Figures 52 through 54 for the fan core, the two outermost elements indicate no significant changes in rotor efficiency as the fan core flow is reduced and bypass ratio increased. The inner most immersion indicates significant rotor hub performance degradation at bypass ratios above 8. This deterioration is a result of the high static pressure imposed at the inlet to the core stream when the bypass ratio is increased. It is unclear however, whether the deterioration is in the rotor, along the hub flowpath between the rotor exit and measurement station or, more likely, a combination of the two. Performance of the fan core OGV deteriorates as bypass ratio increases as shown by increasing OGV total-pressure-loss coefficients. High positive incidence angles on the OGV are indicated. The reduced OGV performance is responsible for the stage efficiency deterioration noted. At lower than design bypass ratio, the negative static-pressure-rise coefficient and the rapid upswing in total-pressure-loss coefficient indicate the approach of a choke condition. Throughout the bypass ratio migration, continuous monitoring of blade and vane vibratory stresses and high response pressure transducers flush mounted in the casing over the fan tip and in the core flowpath did not indicate a fluctuating flow field as would be caused by a rotating stall zone.

Figure 55 shows the total pressure profile in front of the bypass and core OGV's and traces its development during the bypass ratio swing. A radial rake mounted on the splitter midway between fan rotor and bypass OGV was used to determine the total pressure in the bypass stream. A circumferential average of the three radial rakes at core OGV inlet were used for total pressure in that portion of the annulus. Figure 56 shows the surface static pressure distribution on both the top side and the under side of the splitter and shows its variation with bypass ratio. The implied high incidence condition on the splitter leading edge discussed previously is clearly evidenced by the static pressure distribution.

Referring to Figure 55, the three highest bypass ratio readings show a deterioration in total pressure profile in the bypass region near the splitter. The high angle of attack forced on the splitter during high bypass ratio operation creates a severe aerodynamic loading on the bypass side leading edge region which causes high losses and ultimately will produce a flow separation from the surface. The significant deterioration in the fan core for these highest bypass ratio points indicates that the rotor performance and/or the hub flow path between the rotor exit and the measuring station is affected by the bypass ratio migration. However, as was noted previously, no rotating stall zone was detected during the migration. The previously noted apparent drop in rotor and stage efficiency in Figure 51

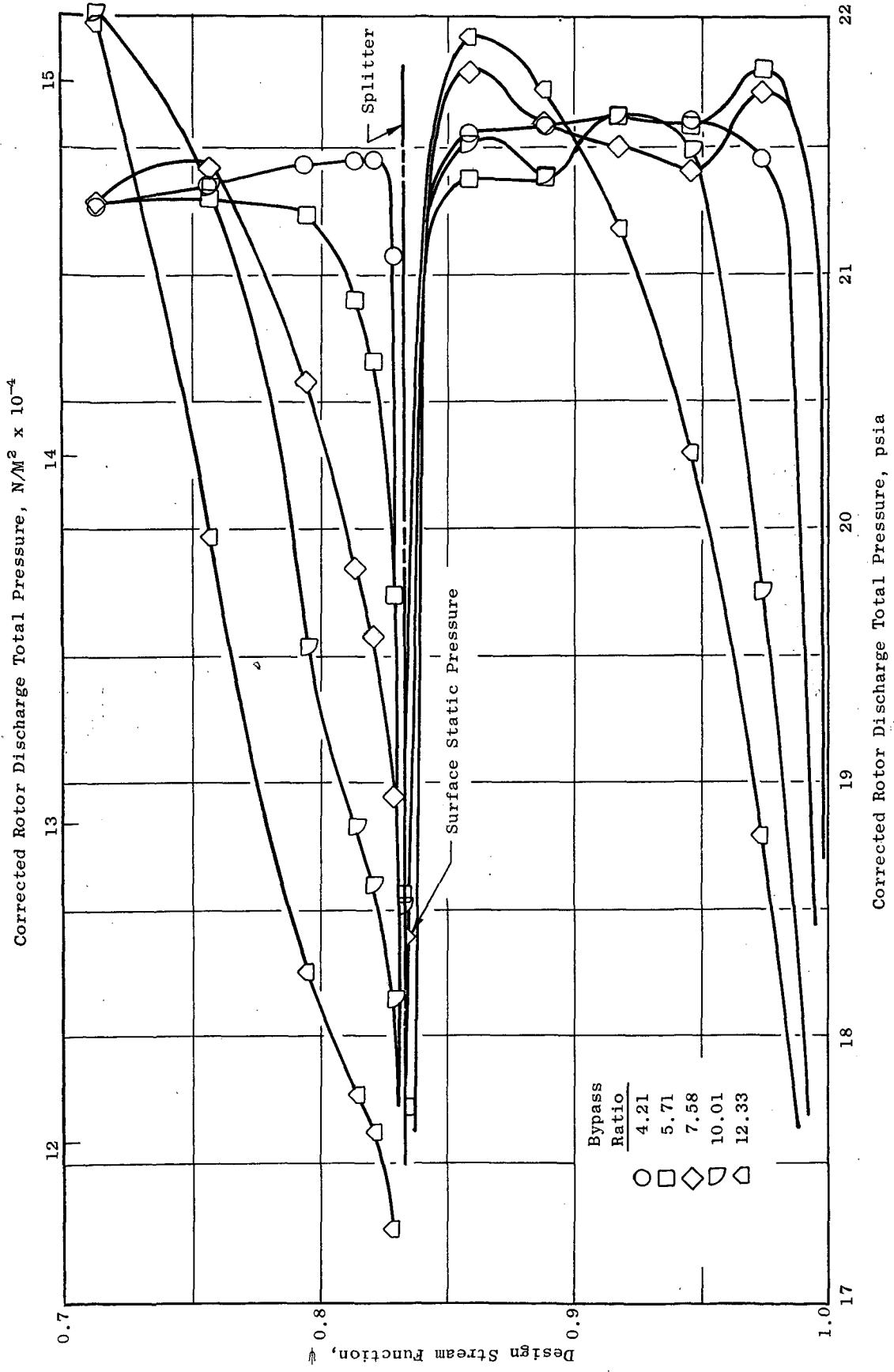


Figure 55. Effect of Bypass Ratio on Rotor Hub Total Pressure Profile.

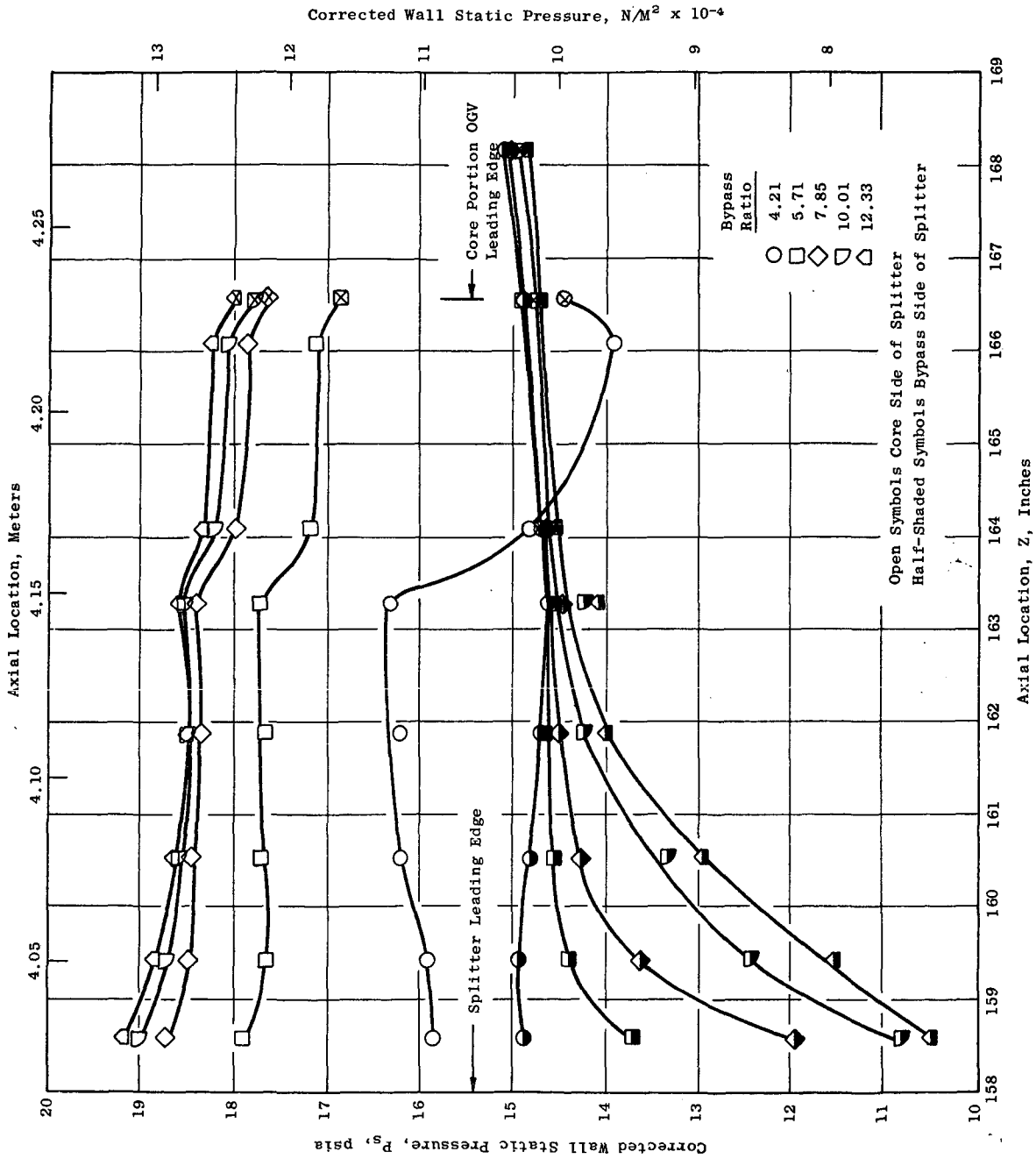


Figure 56. Effect of Bypass Ratio on Splitter Wall Static Pressure.

can be explained by the high splitter loss since the method used to determine the efficiencies is not capable of separating the rotor and splitter performance. The fact that the rotor and stage efficiency in this figure deteriorate by an approximately equal amount, hence the OGV total-pressure-loss coefficient remains relatively unchanged, indicates that the performance of the OGV is not seriously affected by the high splitter loss, at least over the range tested.

#### BYPASS OGV SCHEDULE

A brief investigation to verify the correctness of the bypass OGV setting was conducted at 100% corrected speed for two fan bypass operating lines. This investigation was conducted on Build 1 to ensure that an improper OGV setting was not responsible for the fan performance being below expectations. The results are presented in Figure 57 which shows the series of test points recorded for this investigation on a bypass performance map. The two operating lines bracket the design point with the low operating line being more representative of the nominal operating line. The high operating point data indicate performance deteriorates with OGV opening as would be expected since a high incidence angle condition created by the high operating line is further aggravated as the vane is opened. For the low operating line, performance deteriorated for both an opening and a closing of the OGV. It was judged that the nominal vane setting was near optimum at the design operating line.

Figure 58 shows a comparison of the OGV total-pressure-loss coefficients between the Build 1 and Build 3 configurations. Examination of the comparison indicates only minor differences in performance between the two configurations. Although the optimum OGV setting angle was not verified for Build 3, the relative consistency in OGV performance indicates that no significant improvement could reasonably be expected by a setting angle change.

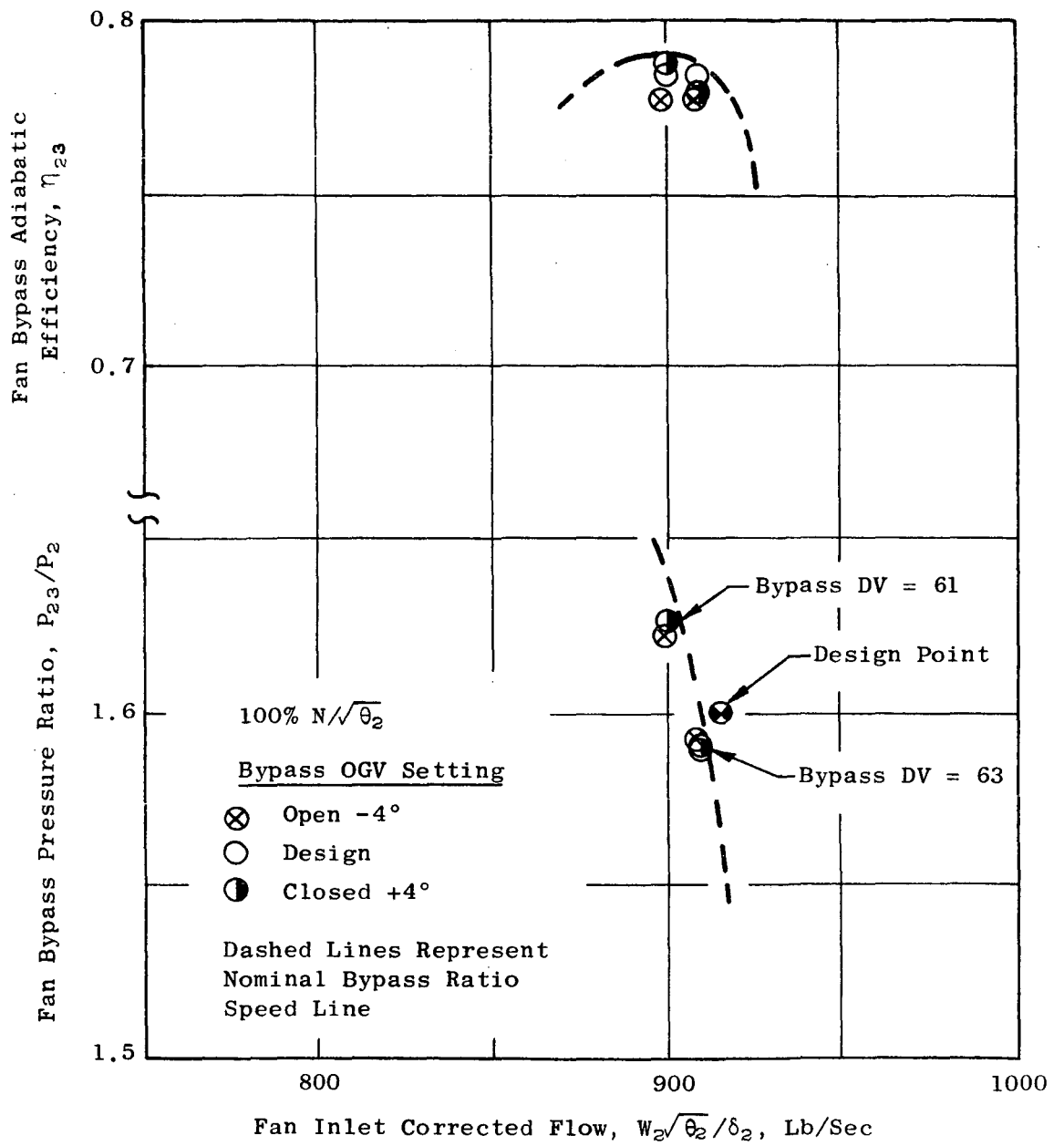


Figure 57. Effects of OGV Setting Angle on Bypass Performance.

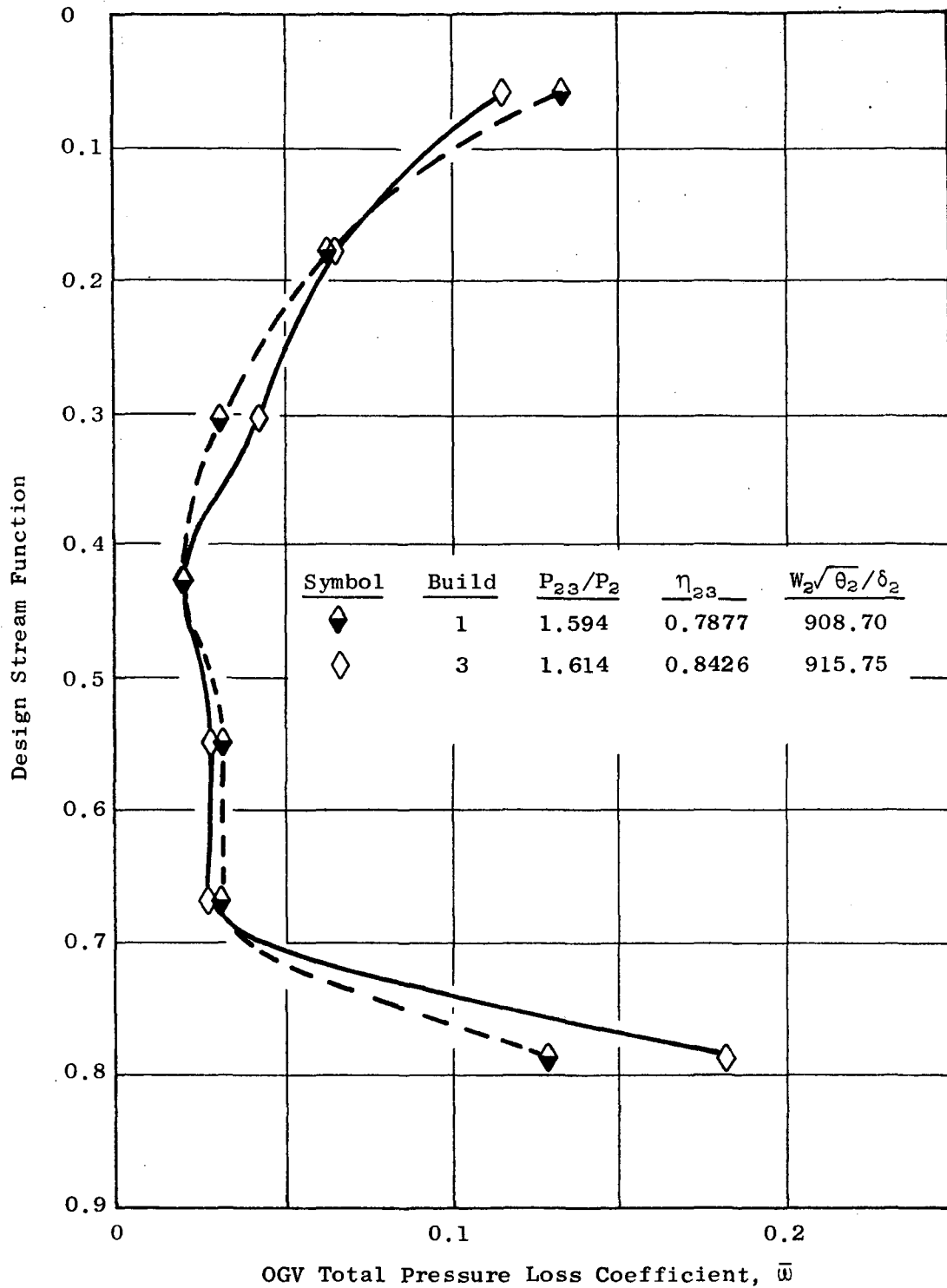


Figure 58. Comparison of OGV Loss Coefficient Between Builds 1 and 3.

## APPENDIX IV

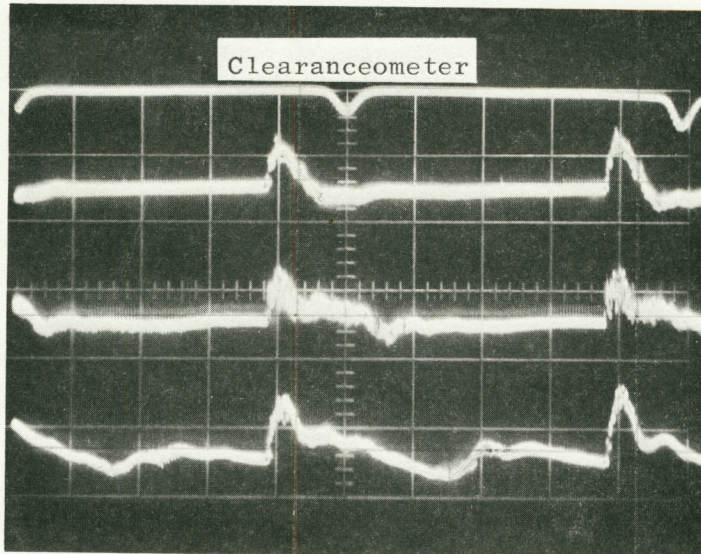
## ROTOR TIP PRESSURE PATTERNS

Ten Kulite transducers were mounted in the casing over the rotor tip to determine the time-varying static pressure field caused by the passage of the rotor blades. The electronic signal from the Kulite transducers was displayed on an oscilloscope. The oscilloscope sweep rate was synchronized with rotor speed and the start of the sweep cycle was triggered with a one-per-rev indicator such that a time-steady picture of the pressure variation within a selected number of blade passages appears on the scope screen. The vertical scale of the scope was calibrated by inputting a known pressure differential and measuring a deflection. The horizontal time or distance scale was calibrated by a clearanceometer which indicates the passing of each blade. The horizontal scale was adjusted such that two blade passages were displayed on the scope screen. The method of data recording was to photograph the screen image. Figure 59 shows the recorded data for a typical reading at 100% corrected speed. A wall static pressure tap was located in the same axial plane as each Kulite. The data reduction method assumes that the wall static pressure tap recorded a true average value and that differences from the average could be added or subtracted according to the differences from the average, as deduced from the photographs. An average trace was deduced from which these differences were obtained by digitizing the photograph over both blade passages and performing a numerical average.

Figure 60, which shows a skeleton of the overall bypass performance map previously presented in Figure 4, shows the data points selected for analysis. The readings for Build 3 were generally selected so as to be representative of a constant area operating line transisting from sea level static operation at 90% corrected speed (takeoff) to altitude cruise operation at 100% corrected speed. Readings at two other operating lines were selected at 90% corrected speed to show the effect of throttling. In addition, two readings from Build 1 at 105% corrected speed were selected for analysis. As discussed in Appendix III, the fan operation for Build 1 at 100% corrected speed and below and for Build 2 was not typical. Therefore, detailed analysis of this Kulite information was not performed. The figure number of the isobar plot appears adjacent to the data point.

Figures 61 through 70 present the isobar plots for the 10 reduced readings. Adjacent to the axial distance scale a triangular symbol shows the location of the Kulite transducer. Only nine Kulite transducers are indicated; the tenth, which was located forward of those shown, was inoperative for the majority of the testing. Shown as an inset on each of these figures is the axial distribution of static pressure, as measured by the wall static pressure taps, for that reading.

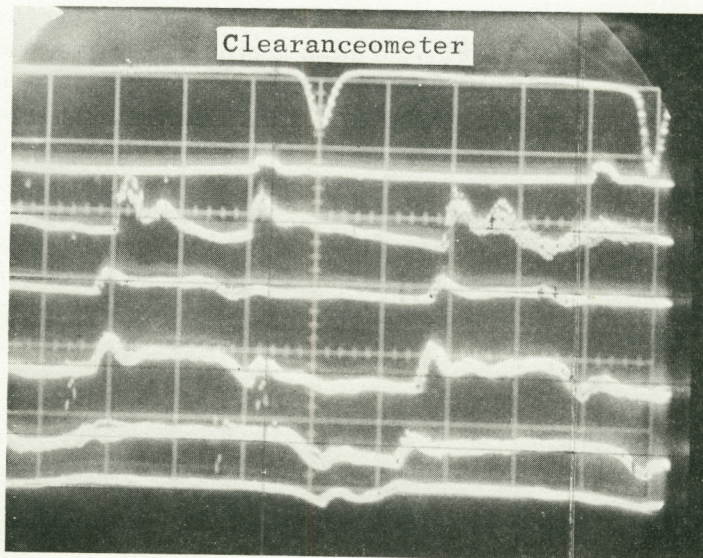
Referring to Figure 62, the 100% corrected speed reading for Build 3, several interesting characteristics are observed. Along the forward portion of the suction surface a precompression raises the static pressure from the



Kulite  
Number  
4

5

6



3

7

7.5

8

9

10

Figure 59. Typical Data Record of Kulite Trace.

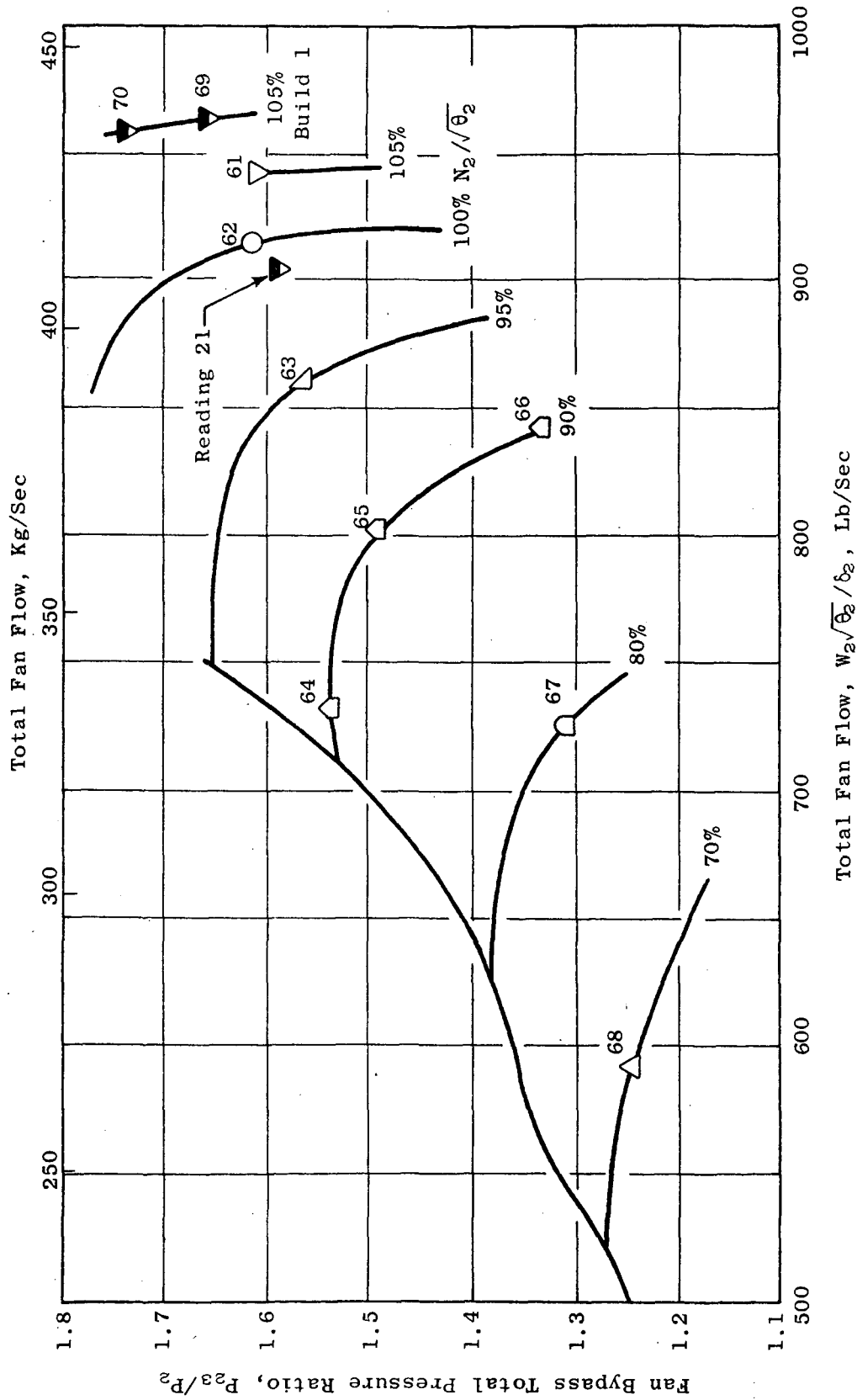


Figure 60. Readings Taken for Rotor Tip Static Pressure Contours.

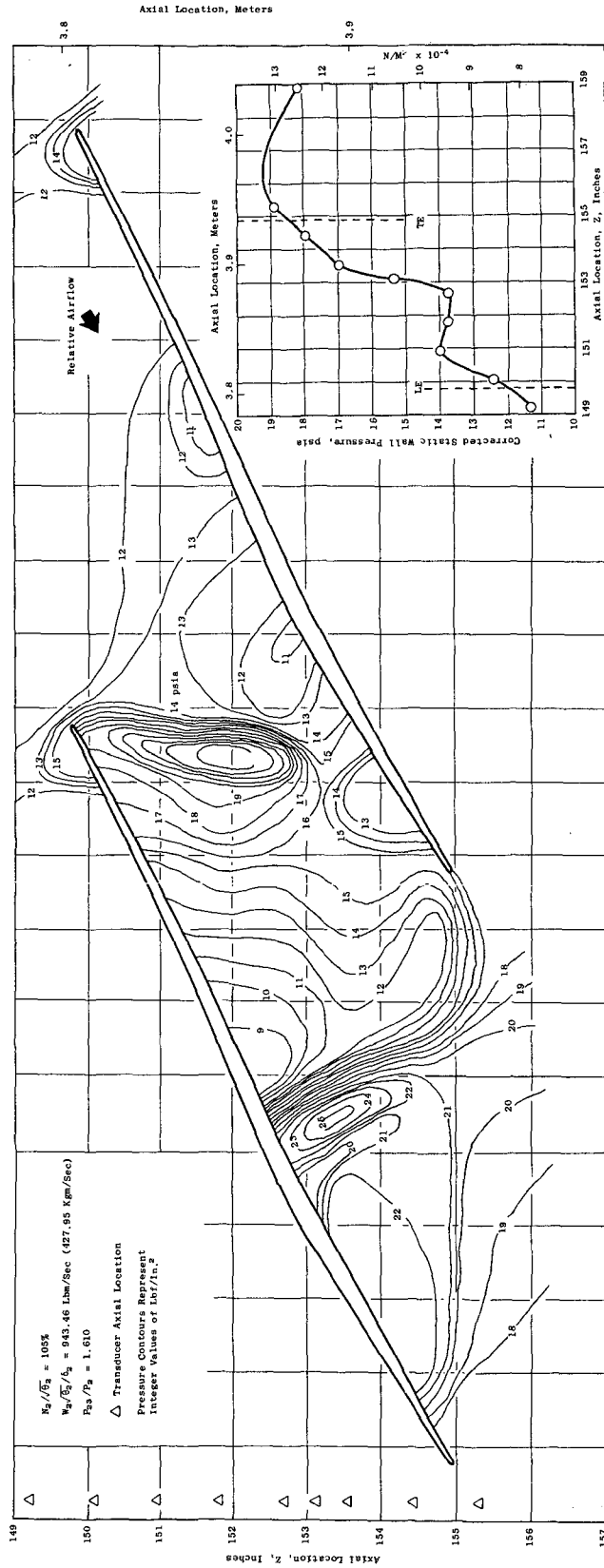


Figure 61. Rotor Static Pressure Distribution.

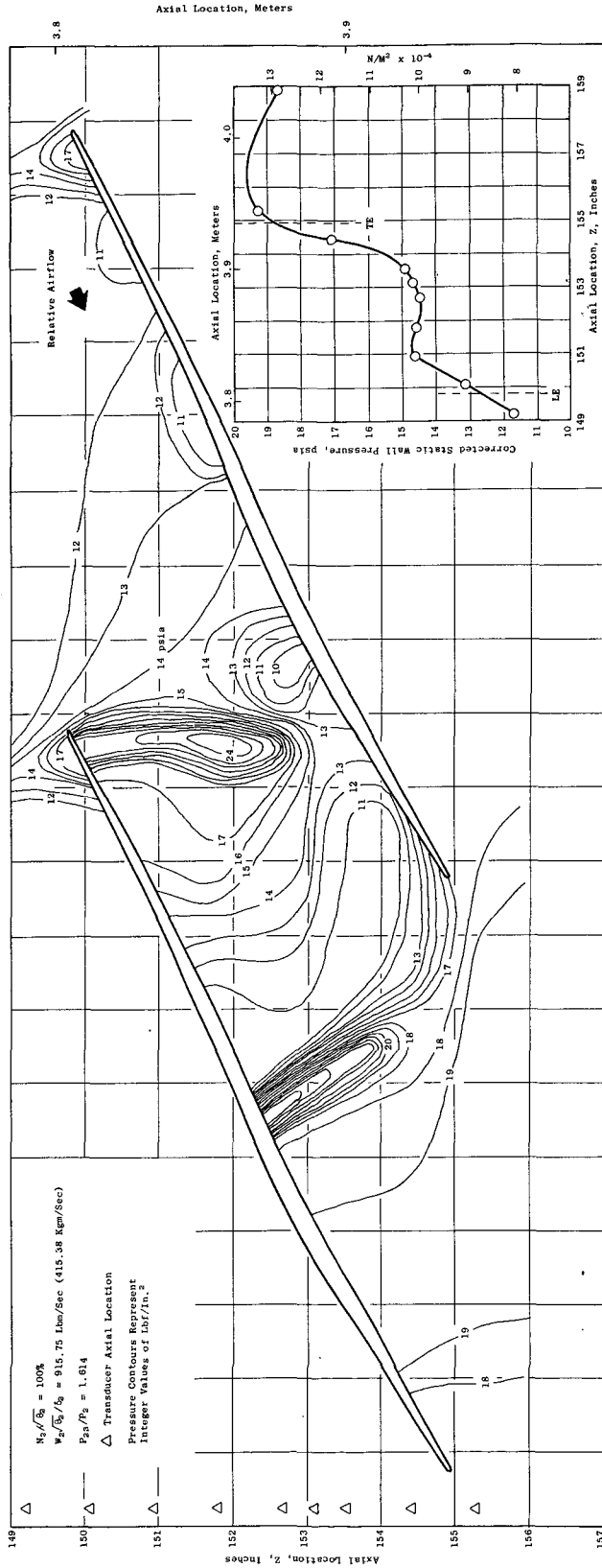


Figure 62. Rotor Static Pressure Distribution.

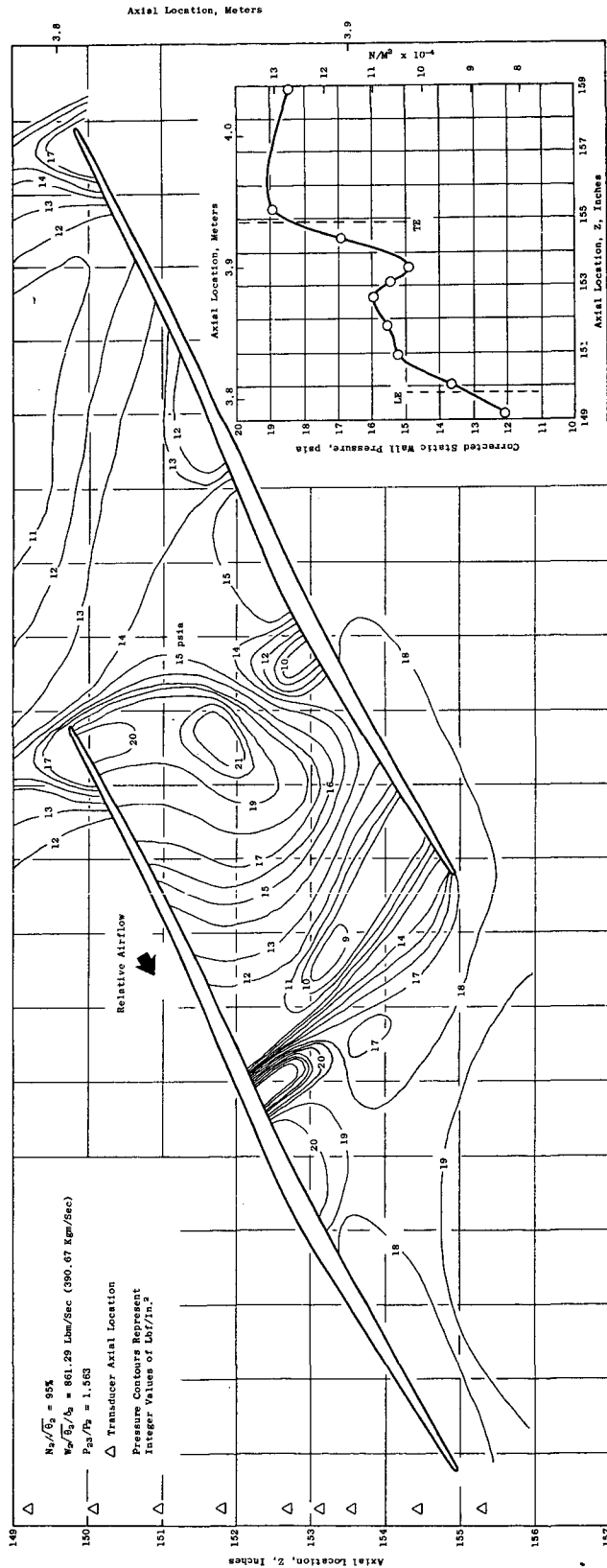


Figure 63. Rotor Static Pressure Distribution.

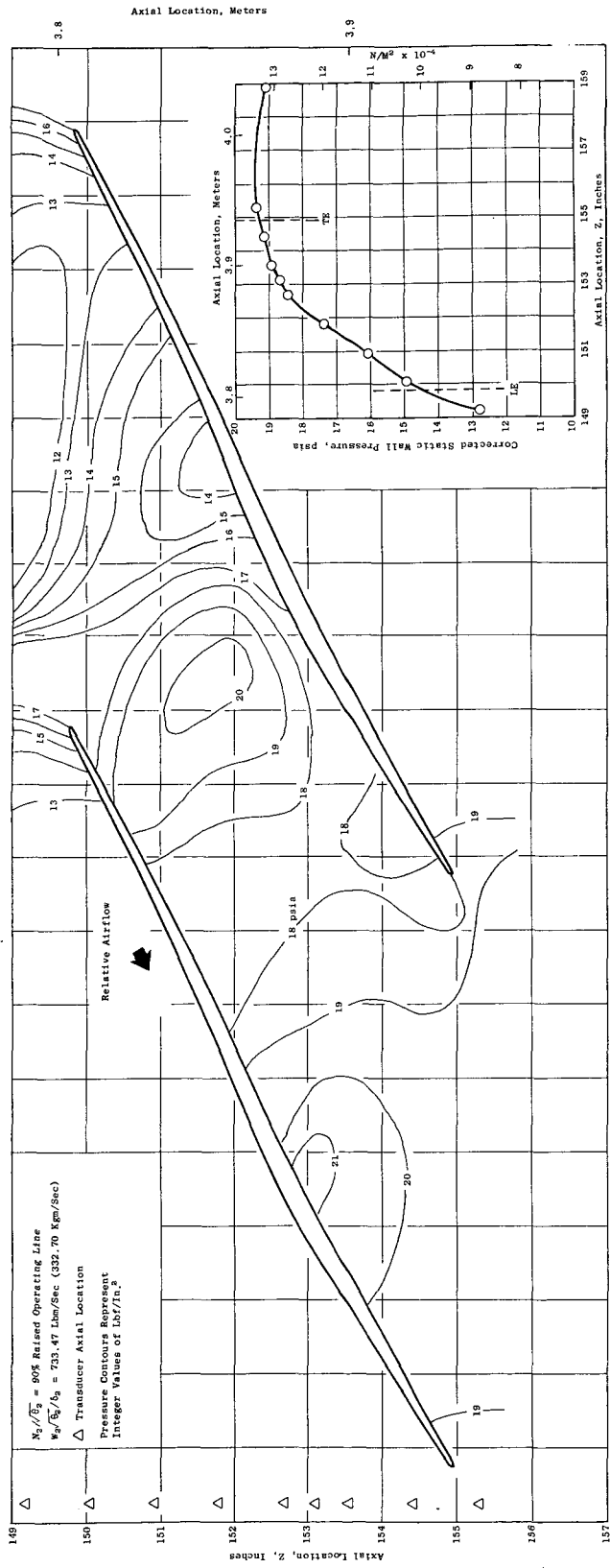


Figure 64. Rotor Static Pressure Distribution.

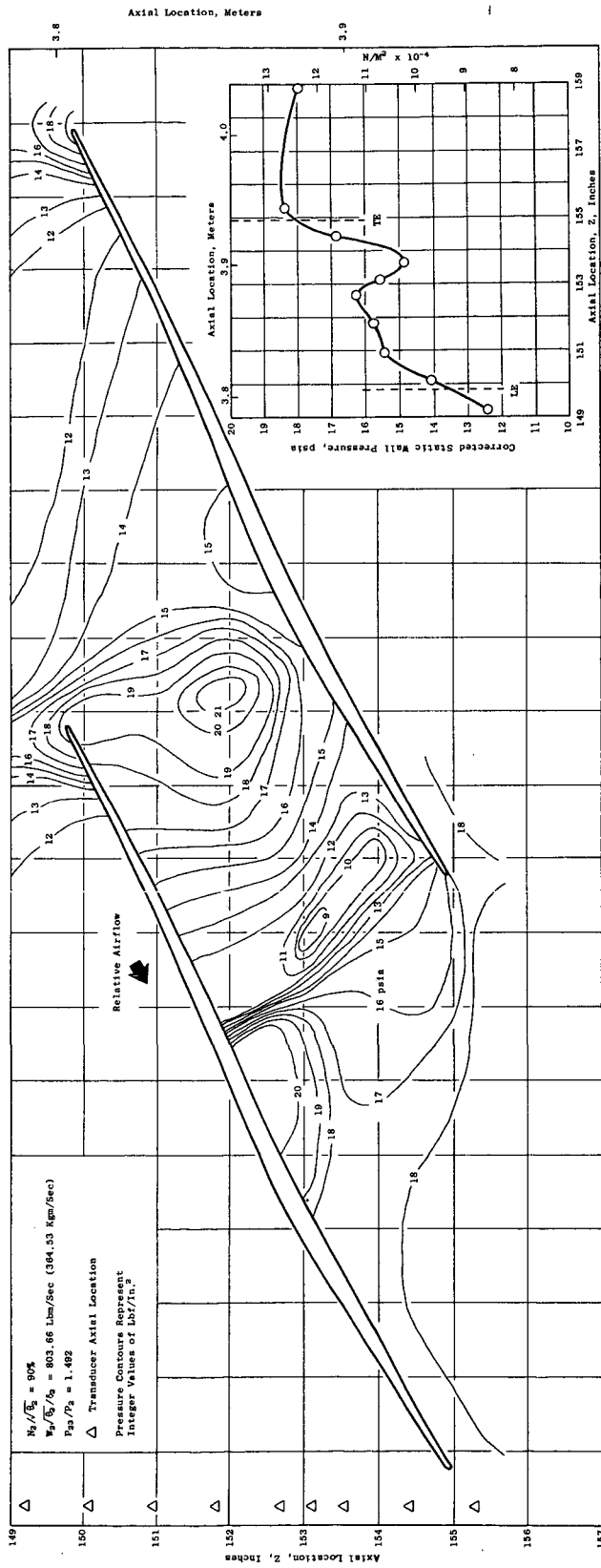


Figure 65. Rotor Static Pressure Distribution.

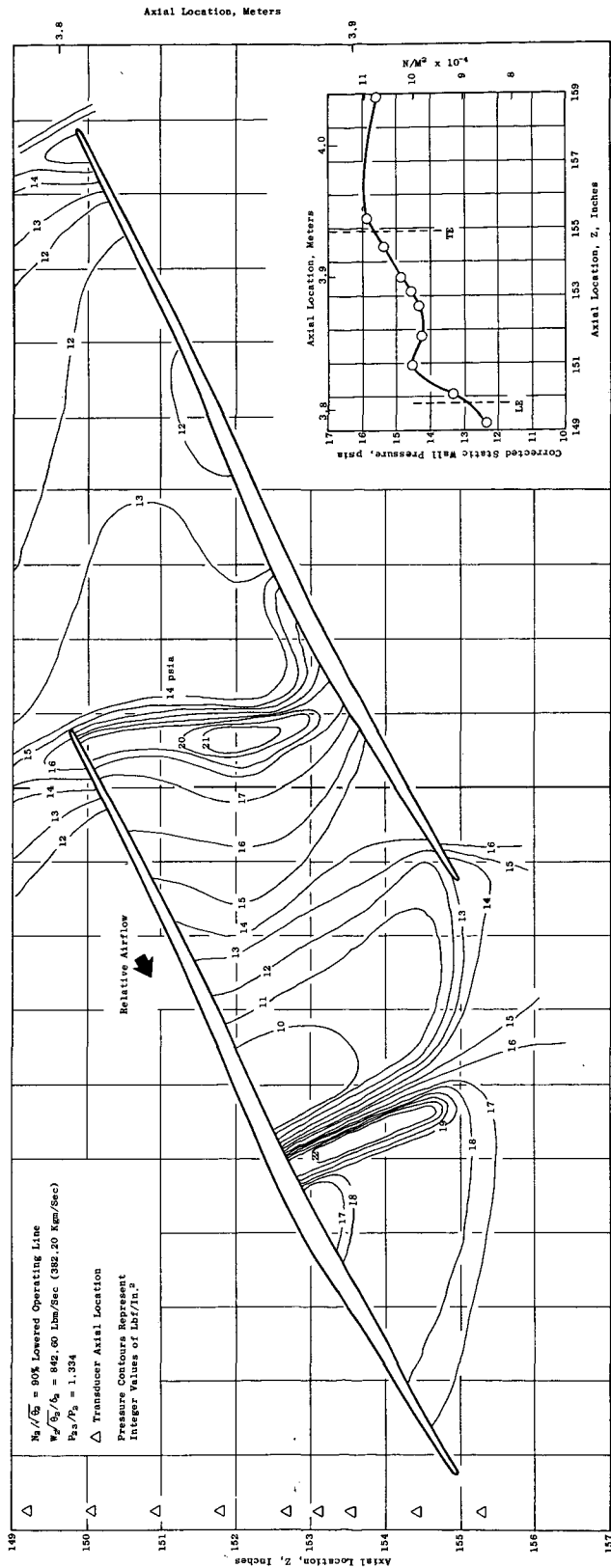


Figure 66. Rotor Static Pressure Distribution.

C.2

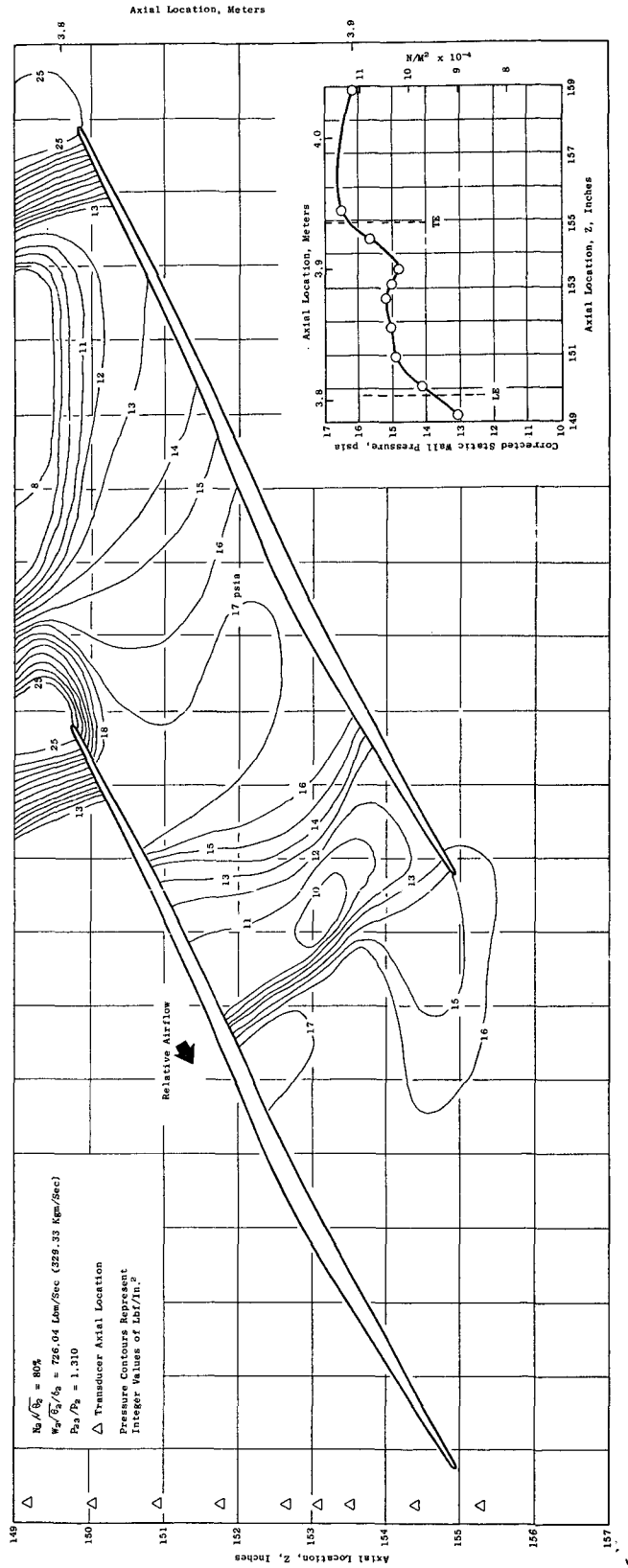


Figure 67. Rotor Static Pressure Distribution.

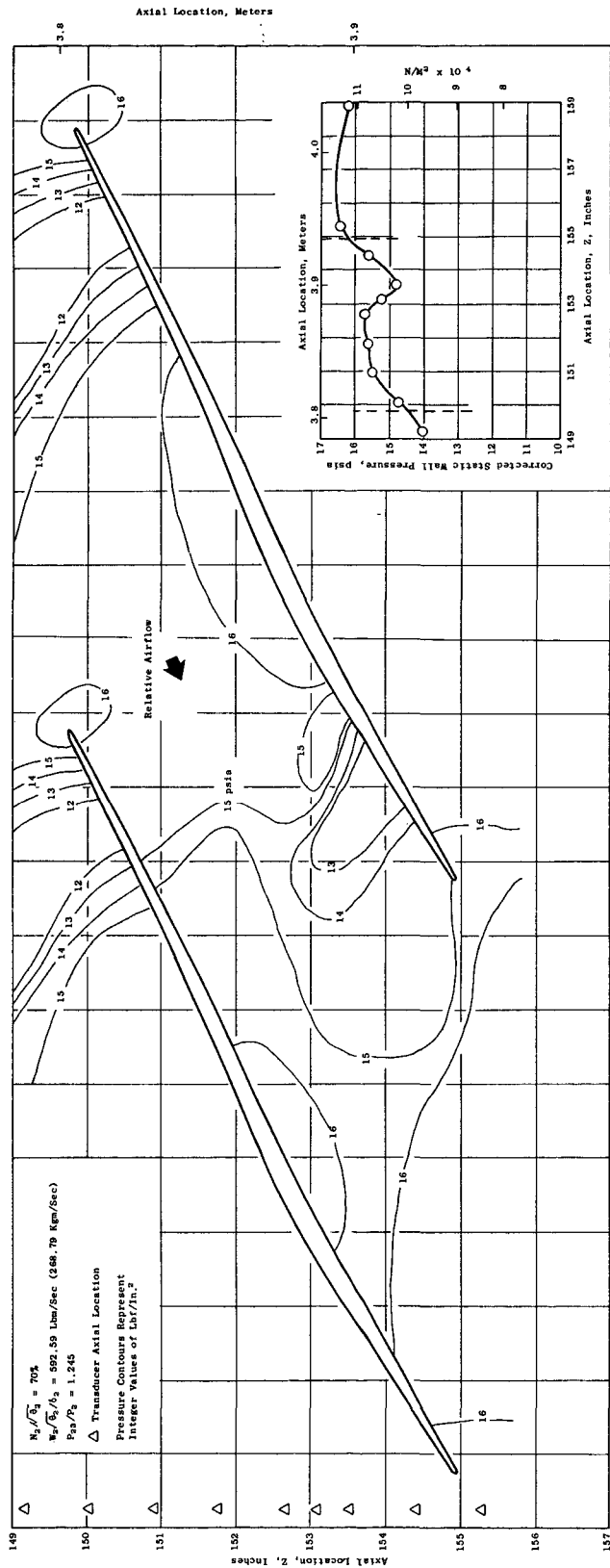


Figure 68. Rotor Static Pressure Distribution.

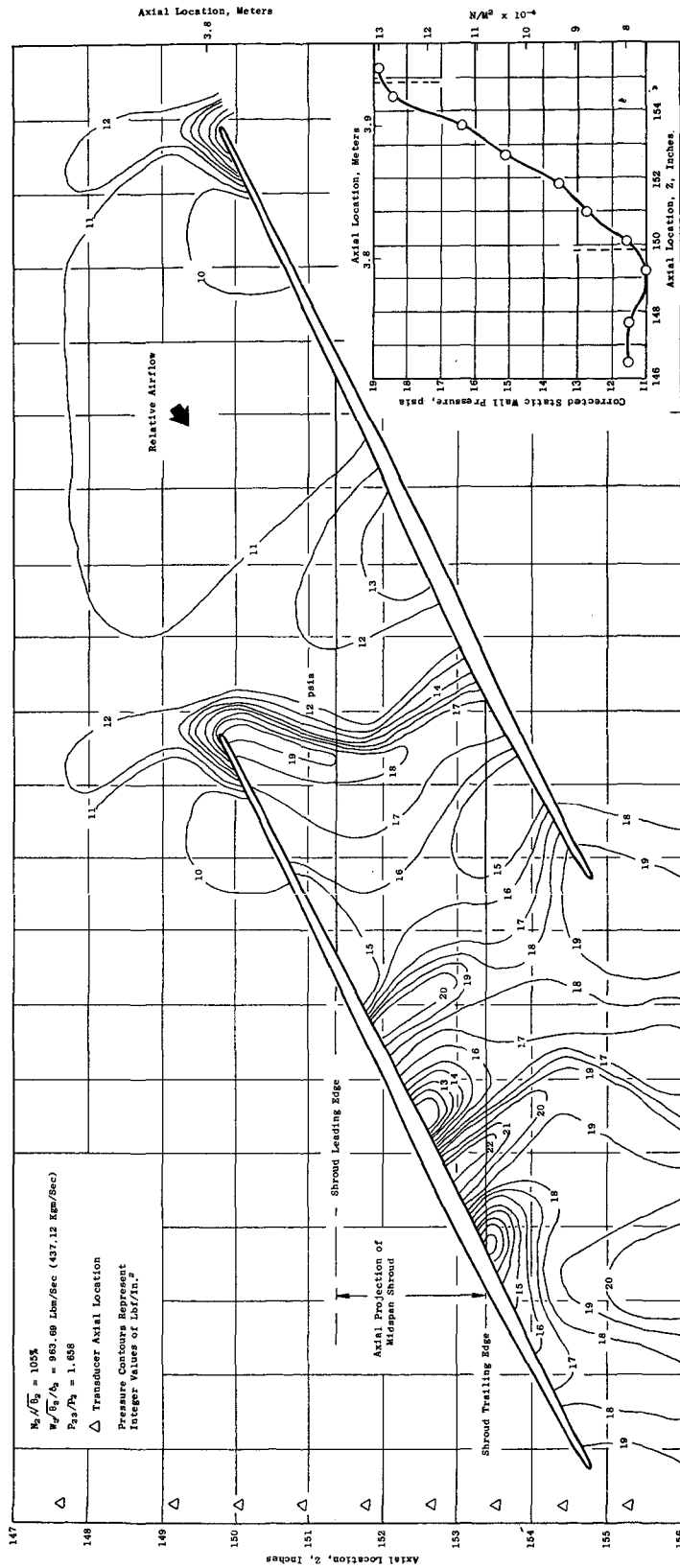


Figure 69. Rotor Static Pressure Distribution.



Figure 70. Rotor Static Pressure Distribution.

inlet level of about 12 psia to about 14 psia prior to the oblique leading edge shock. This precompression requires a deflection of about  $3^\circ$  which is consistent with the design intent of the Build 3 blading. The static pressure ratio of the leading edge oblique shock is 23 divided by 13.5 or 1.7. Oblique shock tables require a total deflection of  $10^\circ$  and a shock angle of  $61^\circ$  to be internally consistent at the Mach number forward of the shock. The approximate shock angle is readily verified. The reflection of the precompression from the pressure surface, about  $3^\circ$ , the included angle between suction and pressure surface, about  $4^\circ$ , and a small incidence angle between the average suction surface and the inlet flow direction account for the majority of the required deflection. Inaccuracies in the pressure data and uncertainty due to the leading edge bluntness are probably responsible for the difference. The leading edge bow shock is of relatively constant strength for about two-thirds of the distance across the passage. It then abruptly diminishes strength and remains at this reduced strength across the remainder of the passage. The most notable difference between the leading edge bow shock in the current fan, compared with past experience, is the large distance for which the shock retains its strength and the abruptness of the change in strength. The relatively abrupt suction surface angle change in the near vicinity to the projected intersection of the leading edge bow shock is a contributor to the abrupt change in shock strength. It is further speculated that a separation region adjacent to the suction surface, in the near vicinity of the projected leading edge shock intersection, may alter the effective blade geometry to produce an expansion corner that is somewhat larger than the geometric blade surface expansion corner. Supporting evidence for this hypothesis is the significant static pressure rise observed along the trailing edge portion of the suction surface. This pressure rise can be explained by a compressive deflection of the flow by the suction surface as would be the case if the above mentioned effective blade geometry had a slope which is more axial than the geometric slope. This hypothesis implies that the separation region is contained and the flow becomes reattached in the trailing edge region. A reacceleration of the flow occurs aft of the leading edge shock to a static pressure level approximately equal to inlet. An oblique shock from the blade trailing edge transitions into a normal shock on the adjacent blade pressure surface which increases the static pressure to the level imposed by the discharge value. The static pressure ratio of about 2 for the passage exit normal shock implies a Mach number into the shock of 1.37. The acceleration from behind the leading edge bow shock to the inlet of the passage exit normal shock implies an increase in passage area of approximately 9%. The loss in relative total pressure, from inlet, implied by the 1.37 Mach number exceeds that measured across the entire blade row. Hence the Mach number entering the shock must be larger than 1.37 which implies a passage area increase greater than 9%. Since this passage area increase far exceeds the geometric passage area increase, it corroborates the hypothesis of a contained separation on the blade suction surface. It is interesting to note that the pressure force on the blade, for a short segment in the midportion of the blade, acts in a direction to remove energy from the fluid.

As the corrected speed is increased to 105%, Figure 61, the shock pattern remains qualitatively similar to that observed at 100% corrected speed. The

angle of the leading edge bow shock is slightly diminished and the aft passage shock is displaced in the downstream direction. The hypothesized contained separation appears to be of significantly diminished size relative to the 100% corrected speed point. This is evidenced by a smaller decrease in average static pressure from behind the leading edge bow shock to the passage exit which implies an area ratio closer to its geometric value. It also is observed that the suction surface is able to sustain a significantly increased static pressure rise at the projected intersection of the leading edge bow shock. Furthermore, the static pressure rise which was previously observed on the trailing edge portion of the suction surface has clearly moved aft and appears as a shock which emanates from the trailing edge and no compressive deflection by the suction surface is in evidence. It is also interesting to note that the isobars behind the leading edge bow shock appear to result from characteristics of the same family as the bow shock. However, for the 100% corrected speed reading, Figure 62, the isobars appear to result from characteristics of both families and perhaps are even dominated by characteristics from the opposite family as the bow shock.

As the corrected speed is reduced from 100% along the nominal operating line, the leading edge bow shock approaches normal and at about 90% corrected speed begins to move forward from the leading edge. Also, the strength of the shock propagating forward into the oncoming flow increases and reaches a peak at about 80% corrected speed. The expansion from behind the bow shock and its termination in a normal shock at passage exit is characteristic down to 80% corrected speed. At 70% corrected speed, the aft passage shock has finally disappeared. A low static pressure along the leading edge portion of the suction surface is retained all the way down to 70% corrected speed. This is a result of an overexpansion from the upstream flow direction which is continuously increasing as speed is diminished.

At 90% corrected speed, as the operating line is lowered, Figures 64, 65, and 66, the leading edge bow shock progressively moves aft from an unstated position forward of the leading edge to a started position at the leading edge. No aft passage shock is observed for the highest operating line. As the back pressure is reduced the aft passage shock forms and, with further reduction to the back pressure, continues to move aft as expected.

Figures 69 and 70 present isobar contours for Build 1 at 105% corrected speed for two different operating lines. Referring to Figure 69, the lower operating line of the two readings, an expansion occurs from upstream to the forward portion of the suction surface. A modest precompression follows which raises the static pressure to slightly above inlet just forward of the leading edge shock. The leading edge shock is oblique for approximately 50% of the distance to the adjacent blade suction surface and then transits to become approximately normal to the incoming flow for the remainder of the distance. The static pressure ratio of the oblique portion of the leading edge shock is 1.5 which requires a deflection of  $8^\circ$  and a shock angle of  $50^\circ$  to be consistent with classical oblique shock theory. The  $50^\circ$  shock angle is readily

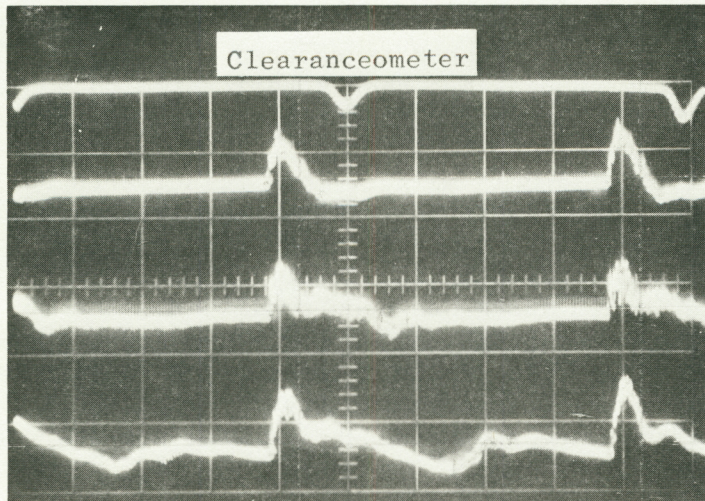
verified. The included angle between pressure and suction surface of  $4^\circ$ , the  $1.5$  to  $2^\circ$  reflection of the precompression waves, a small angle of incidence of the average suction surface angle relative to the incoming flow and bluntness effects of the leading edge make the actual deflection angle reasonably internally consistent.

Two notable differences between the leading edge shock for Build 1 and Build 3, Figures 69 and 61, respectively, are the shock strength adjacent to the suction surface and the increase in the strength of the Build 3 oblique shock as distance from the leading edge increases. The precompression of the Build 3 blade was significantly increased from that of Build 1. Furthermore, the precompression was distributed such that none occurs in the leading edge region forward of the first captured wave and the maximum occurs just forward of the mouth. Therefore, as distance increases from the leading edge along the leading edge shock, the amount of compression increases and an increase in static pressure is required. The reduced precompression of the Build 1 blades, when coupled with throat area considerations, require a greatly reduced adjacent blade surface curvature in the near vicinity of the mouth. This reduced curvature is apparently responsible for the additional static pressure rise observed on the suction surface of the Build 1 blade. Returning to Figure 69, the flow reaccelerates from behind the leading edge shock to the passage exit where a shock, approximately normal to the flow, is observed. The magnitude of the reacceleration is greatly reduced from that previously observed on Build 3, Figure 61, hence the implied area ratio of the expansion is greatly diminished. A reduction in the extent of the hypothesized contained separation for the Build 3 blades or the lack of reattachment of the separation would explain the implied area ratio reduction. Since a substantial static pressure rise is observed on the suction surface at the intersection of the leading edge shock and along the trailing edge portion, a reduction in the extent of the hypothesized separation is believed more likely. Behind the aft passage shock, along the pressure surface, a second reacceleration followed by a shock and a third reacceleration followed by substantial static pressure rise is observed. The exact reasons for the reaccelerations and compressions is not obvious. However, it will be recalled that Build 1 had a part-span shroud and, as discussed in Appendix III, the shroud had an abnormally large effect on performance. It is possible that the shroud constrained the flow from the natural radial shifts it otherwise wanted and the resulting highly complex three dimensional patterns give rise to the observed measurements.

As the operating line is raised, Figure 70, the leading edge shock moves forward, becomes more normal and strengthens. The reacceleration to each of the three previously mentioned pressure surface low pressure regions diminishes and each of the pressure rise regions move forward. The relative behavior is about as expected.

Figures 71 and 72 illustrate graphically the differences in shock swallowing between the Build 1 and Build 3 configurations. Figure 71 shows Kulite traces for Build 1 and Build 3 at 100 and 105% corrected speeds. The locations of the shock and the blade are indicated. Physically, the Kulites are in an axial line on the fan casing and are numbered such that increasing

numerals proceed front to back. Hence, a shock which appears at the same time on two adjacent Kulite traces is axial. A shock which appears time wise later on the higher numeral of two adjacent Kulite traces is more oblique relative to the incoming flow and a shock which appears time wise earlier on the higher numeral of two adjacent Kulite traces is more normal relative to the incoming flow. The location of the shock as deduced from Figure 71 and from similar photographs at lower speeds has been superimposed on a blade layout and is shown in Figure 72. Generally the points selected correspond to fixed discharge nozzle operation. Referring to Figure 72 at 70 and 80% corrected speed, the shock for Build 3 is slightly aft relative to Build 1. At 90 and 100% corrected speed the difference is much greater. On Build 3, the 90% corrected speed shock is on the verge of being swallowed and the 100% corrected speed shock has clearly been swallowed. On Build 1, neither the 90 nor the 100% corrected speed shock has been swallowed. The relative slope differences of the Build 1 and Build 3 100% corrected speed shocks is readily apparent from Figure 71 and the preceding discussion on interpretation. However, on both Builds 1 and 3 at 105% corrected speed, the shock is clearly swallowed. No significant difference in the shock location nor shape are noted for this latter condition.



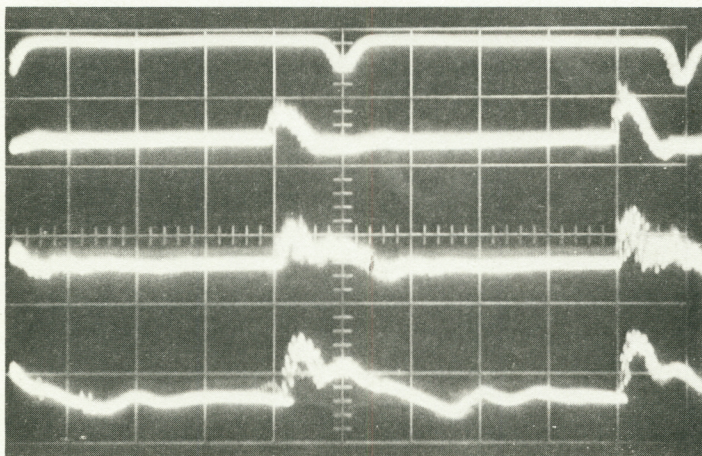
Kulite  
Number

4

Build 3  
100%  $N/\sqrt{\theta}$

5

6



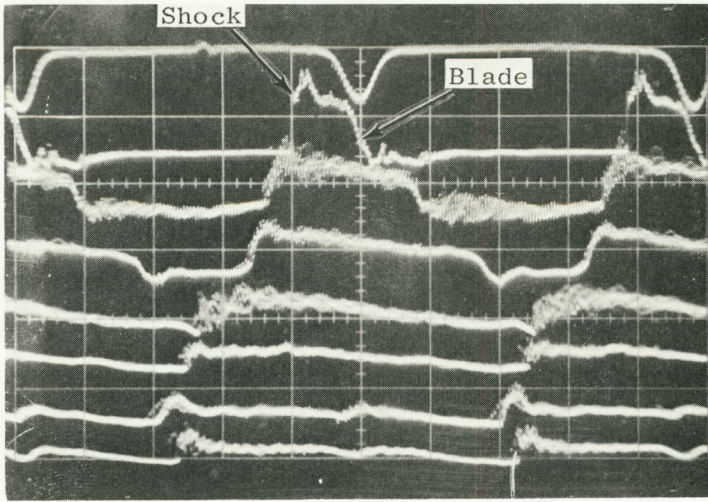
4

Build 3  
105%  $N/\sqrt{\theta}$

5

6

Figure 71. Comparison of Build 1 and Build 3 Kulite Traces at 100% and 105%  $N/\sqrt{\theta}$ .

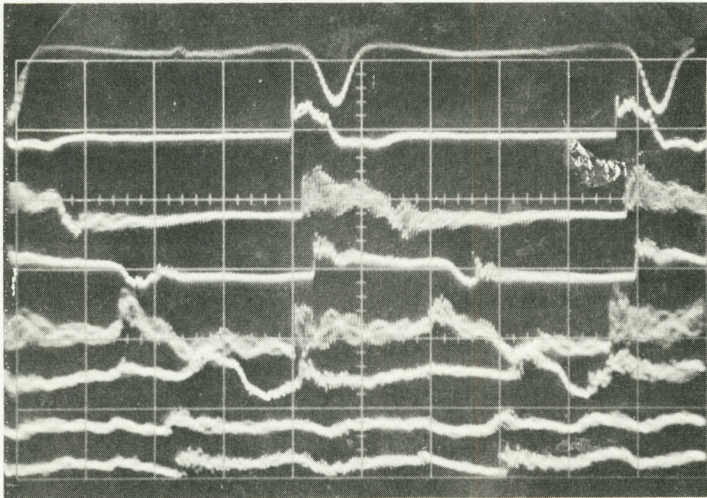


Kulite  
Number

4  
5  
6  
7  
8  
9  
10

Build 1

100%  $N/\sqrt{\theta}$



4

Build 1

105%  $N/\sqrt{\theta}$

5  
6  
7  
8  
9  
10

Figure 71. Comparison of Build 1 and Build 3 Kulite Traces at 100% and 105%  $N/\sqrt{\theta}$  (Concluded).

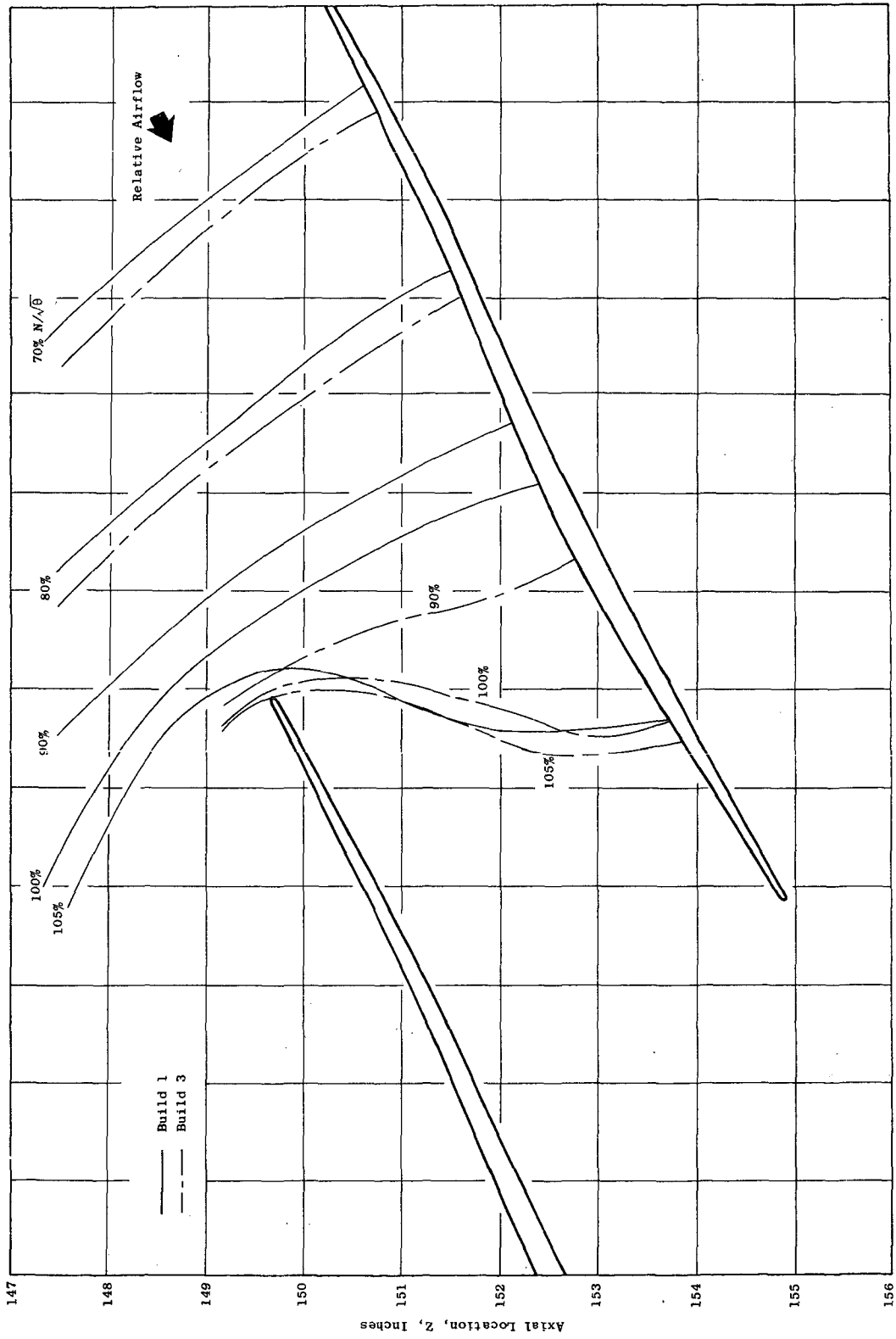


Figure 72. Comparison of Build 1 and Build 3 Shock Swallowing Process as Speed Increases.

## APPENDIX V

### AEROMECHANICAL CHARACTERISTICS OF FAN C BASED ON FAN COMPONENT TESTING

#### A. INTRODUCTION

This appendix covers the aeromechanical characteristics of the NASA Quiet Engine Program full-scale Fan C vehicle which was tested in the General Electric Company Lynn Component Test Facility. The first section of this appendix covers the rotor and the second section the stator. A background concerning the modification made to the fan blades for this rotor and the techniques used in determining blade scope limits are given to complete the report. The investigation included performance mapping in the 50 to 105% corrected speed range with three inlet distortion screen patterns designed to have a magnitude of about 0.15 to 90% speed\*. The three patterns were tip radial, simulated crosswind, and 1/Rev.

By the way of background, terminology which may not be of common understanding, and/or is peculiar to the General Electric Company, is defined below:

#### Aeromechanics

The technical discipline that considers the interaction of the aerodynamic environment with the elastic and mechanical properties of turbo-machine component, such as rotor blades or stator vanes.

#### Vibration Mode

Identification of a variety of ways in which a structure can vibrate, each of which has its own natural frequency. Examples in blading are:

- First flex (1F): vibration normal to the least-moment axis with a node (zero motion) only at the fixed end(s) of the blade.
- Second flex (2F): same as first flex except there are two nodes, one at the fixed end(s) and another at some point on the blade air-foil away from the ends.
- First torsion (1T): vibration having a twisting motion with a node running radially along the blade near its mid-chord location.
- System mode: one in which vibratory coupling occurs between blades as well as between the blades and the disc. The disc involvement involves radial nodes which are called nodal diameters. The disc involvement generally

$$* \quad \Delta P/P = \frac{P_{Tmax} - P_{Tmin}}{P_{Tmax}}$$

induces lower system mode frequencies than for the corresponding blade modes; and, like blade resonances, system mode resonances to excitations fixed in space (distortion, struts, etc.) can occur when the number of nodal diameters coincides with corresponding integral orders. See Chapter VI of Den Hartog, Mechanical Vibrations for more details.

Integral-Order Resonance This type of blade vibration exists when a natural frequency corresponding to a "mode" of vibration is induced to respond at an integral multiple of rotor speed. These multiples are referred to as "orders" or "per-revs". Such resonances can occur when a blade natural frequency crosses each per-rev.

Separated Flow Vibration This type of blade vibration involves the random amplitude response of the blading to turbulent excitation, either from separated flow on the blade itself or from free-stream turbulence. It occurs in one, or more, of the normal blade vibration modes, those having the lowest frequencies usually being the most responsive.

Endurance Limit Vibratory stress above which fatigue failure will occur in  $10^7$  cycles, or less.

## AEROMECHANICAL CHARACTERISTICS OF FAN C ROTOR

This portion of the Appendix covers the aeromechanical characteristics of the unshrouded Mod. II Fan C rotor which was tested in Build No. 3 of the NASA Quiet Engine Fan C Vehicle in the Lynn Component Test Facility. A background concerning the modifications made on the fan blades for this rotor and the techniques used in determining blade scope limits are given to complete the report.

The regions in which the fan can be continuously operated without encountering stall or aeromechanical distress are defined on the fan performance maps. These maps are bounded on the upper side by an "operational limit line". This limit line is defined either by the occurrence of rotating stall or excessive self-excited vibration of the fan blades. A separate map is given for fan operation with a clean inlet and for each of the distortion patterns tested. The mechanical response of the fan under the different inlet operating conditions tested is discussed as well as the basis for setting the operational limit conditions on fan operation. Specific areas discussed are as follows:

- A summary background on the modifications to the fan blades leading to the Mod. II design used for Build No. 3 of the test vehicle.
- An outline of how laboratory test and analytical models were employed in determining the vibratory scope limits to be allowed for the "engine" strain gages.
- A discussion of the aeromechanical response characteristics of the fan blades due to various stimuli with a clean inlet.
- A discussion of the aeromechanical response characteristics of the fan rotor with distorted inlet flow. The distortion patterns tested were a tip radial, a crosswind takeoff pattern and a one-per-rev pattern.

### A. BACKGROUND

The original Fan C blades were designed with a part-span shroud when it was determined that without the shroud the blades might not have sufficient margin between the operating line and the throttled condition where self-excited vibration of the blades would occur. This rotor was tested in the Lynn Component Test Facility between February 22 and March 5, 1971. The shock pattern in the blade passage of this rotor was not "swallowed" as expected below 103% fan speed. At this speed, the shock would abruptly become "started" with a resultant jump in fan efficiency. Below this speed, the fan efficiency failed to reach the desired levels.

In an attempt to improve the design point efficiency, the blades were modified for Build No. 2. The blade camber was changed in an attempt to induce the shock to become "started" at a lower speed. Since the blades were made of a high strength titanium with limited ductility, recambering had to be accomplished by hot forming the blades in a closed die. To ensure the forming process would not degrade the blade material properties, sections of a spare blade were subjected to forming conditions similar to those planned for the fan blades. These tests indicated that the forming would cause only a slight loss (5.6%) in the average longitudinal ultimate strength, but resulted in a considerable improvement in the elongation (51%) and in the reduction in area (8%) of the titanium. This was considered a desirable trade in material properties. This blade (Mod. I) was tested in Build No. 2 of the Fan C vehicle between April 26 and April 28, 1971. The modification did not produce the desired results. Little change in the design point efficiency was noted. Testing of this build was terminated to prepare the blades for a second modification.

It was determined that the blade shrouds could be removed if the blades were twisted closed sufficiently in the outer span. This overtwist would provide the desired margin between the operating line and the throttled condition where self-excited vibration of the blades might be expected to occur. This increased twist is in addition to that necessary to compensate for the additional elastic untwist which would occur due to the removal of the shrouds. Removing the shrouds was expected to improve the cascade "starting" capability and eliminate the efficiency loss caused by the shrouds. Over twisting the outer span also appeared attractive since the energy input at the blade tip was greater than the original design intent. The fan blades were removed and this modification was made. The twisting was done by a hot forming procedure so that the material properties information gained during the first modification of the blade would remain valid.

The Mod. II blade for Build No. 3 of the test vehicle did improve the fan design point efficiency by about 5 points. The cascade became "started" continuously between 90 and 95% speeds along the operating line. The overtwist provided the desired margin between the operating line and the more throttled condition where self-excited blade vibration was encountered between 60 and 90% speeds.

## B. RESULTS AND DISCUSSION

### 1. Scope Limits

It is practical to install and monitor only a limited number of strain gages on the blades during a compressor test. Using these engine gages, it is necessary to ensure the safety of the compressor against excessive vibration in any of a number of possible blade vibratory modes. This is done by establishing scope limits for the gages for each of these possible

modes. This scope limit conservatively represents the maximum vibratory stress that can be permitted in a given mode without incurring fatigue damage somewhere on the airfoil. The mode of vibration is easily determined by measuring the frequency of the vibratory stress signal.

In determining scope limits, the steady-state stress distribution is first determined. Then, by "overlaying" the vibratory stress distribution for a mode, it is possible to determine the location where a fatigue crack would first be initiated for a sufficiently high vibratory amplitude. This location is known as the critical point. If the vibratory stress at this point is not allowed to exceed the endurance limit at this location, the blade can be protected from fatigue damage in this vibratory mode.

It is not practical to locate a strain gage at each of the critical points for every possible vibratory mode. Instead, only a few engine gage locations are selected and use is made of the known ratios of vibratory stress levels between these locations and the critical points to monitor the stress levels at these latter points. Engine gage locations are selected with the idea that at least one of the locations should be sensitive to each of the possible vibratory modes. The engine gage locations for the Mod. II Fan C blades are shown in Figure 73.

The steady-state stress distribution is determined by combining analytical and experimental means. For the outer  $3/4$  span of the blade, the stress pattern is determined using computer programs which have been shown to provide good correlation with test results in this region. This stress pattern near the blade root is determined by first analytically determining the various components of moments and forces near the blade root under operating conditions. The stress influence coefficients (i.e., stress per unit moment or force) due to these various components are experimentally determined in the laboratory for many points in and around the blade root. Multiplying these stress influence coefficients by the appropriate components of the loads and summing the results determines the blade root stress pattern. The steady-state stress distribution patterns for the Mod. II fan blade at 100% design speed (5200 rpm) as determined by this method are shown on Figures 74 and 75.

Determining the vibratory stress distribution for the high blade mode is done experimentally. A blade is instrumented with many strain gages around the blade root and over the airfoil and vibrated in the laboratory at each of its natural frequencies. For the lower modes, a more sophisticated method is necessary because the frequency of these modes and the associated stress pattern change markedly with engine speed. This is best demonstrated by the first flexural frequency which increases 300% from 38 cps with the rotor at rest to 115 cps at 5200 rpm. The vibratory stress pattern at 5200 rpm in this mode has little resemblance to that measured in the laboratory. The stress pattern for these modes is determined in a manner very similar to that used to calculate the steady-state stresses. The pattern in the outer  $3/4$  blade span is determined with the aid of a computer program which gives

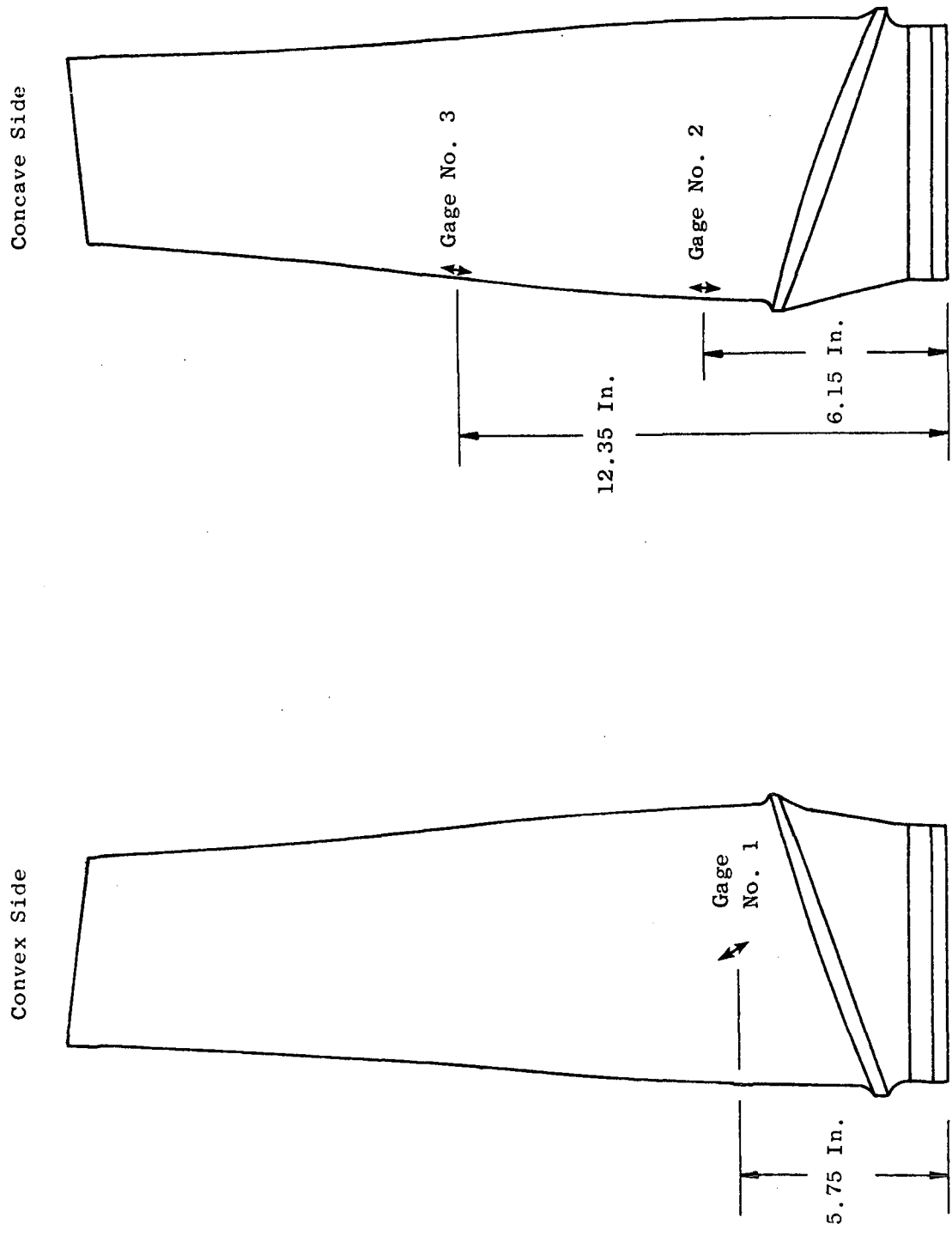


Figure 73. Engine Gage Locations.

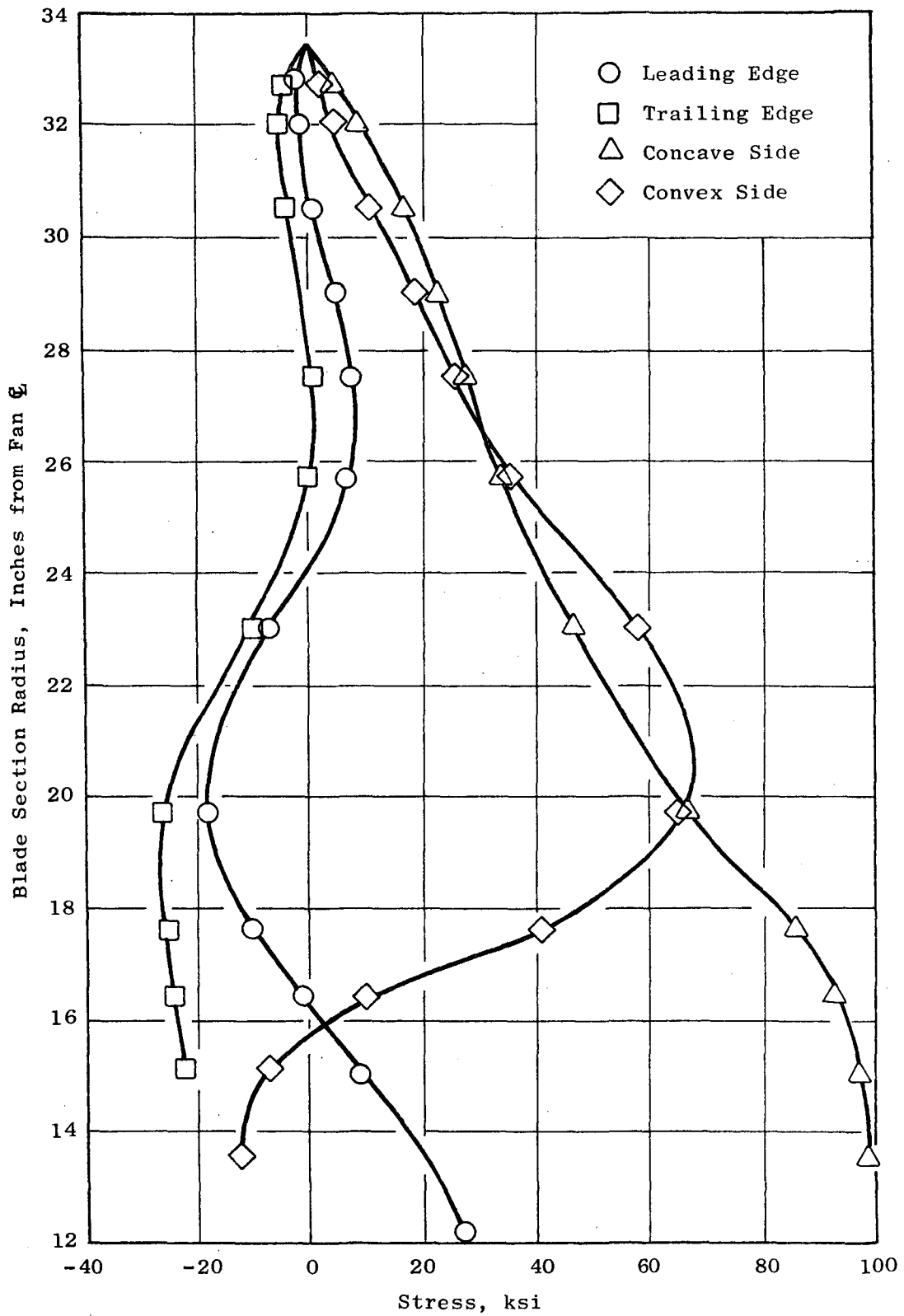


Figure 74. Mod. II Steady-State Stress Distribution at 5200 rpm.

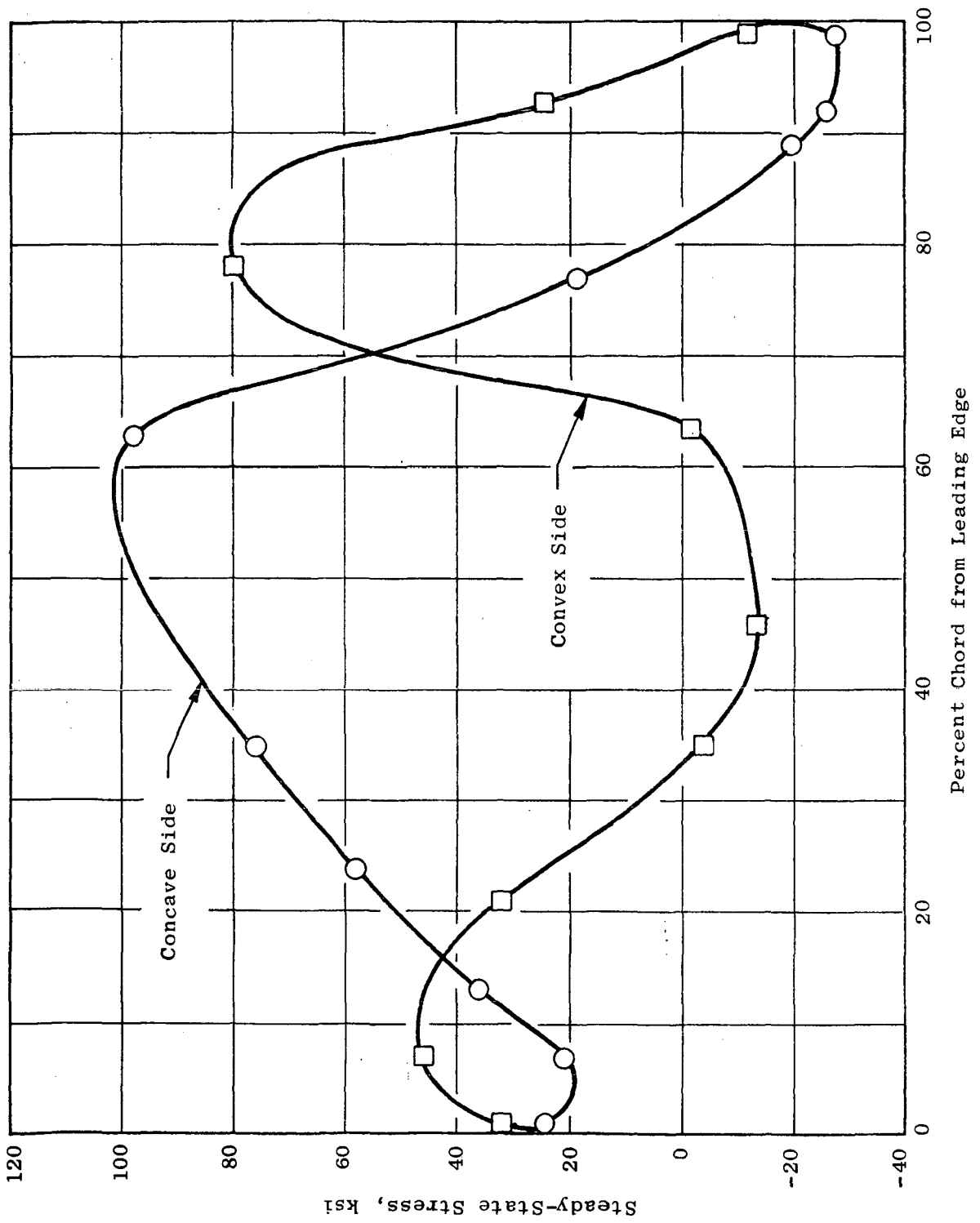


Figure 75. Mod. II Blade Root Stress Distribution at 5200 rpm.

very good results for the lower modes. The blade root stress pattern is calculated using the vibratory moments and the experimentally measured stress influence coefficients.

With both the steady-state stress pattern and the vibratory stress patterns known, it is possible to determine the critical points for vibratory modes. The critical point is that location on the blade where the following ratio (R) is a maximum.

$$R = \frac{\sigma_v}{\sigma_e}$$

Where:  $\sigma_v$  = The vibratory stress at the point relative to any consistent base.

$\sigma_e$  = The endurance limit at that point

The endurance limit at a point can be determined from a fatigue limit diagram when the steady state-stress at the point is known. The fatigue limit diagram which is used lies three standard deviations below the mean curve to ensure that only the minimum expected material properties are used for determining the scope limits.

The following relationship can now be used to determine the scope limits for all pertinent modes of blade vibrations:

$$\sigma_{\text{Scope}} = \frac{(2) (\sigma_{\text{gage}} / \sigma_{\text{critical point}}) \sigma_e}{K_v K_e K_c}$$

Where:  $\sigma_e$  = The single-amplitude endurance limit at the critical point on the blade

$(\sigma_{\text{gage}} / \sigma_{\text{critical point}})$  = The ratio of the vibratory stress at the location of the strain gage to the vibratory stress at the critical point on the blade for the vibratory mode being considered.

$K_v$  = An allowance for blade-to-blade vibratory response variation (usually 1.3 based on past experience).

$K_e$  = A factor to allow for the tolerance in the strain gage electronics circuits (usually 1.05).

$K_c$  = A factor to allow for unmeasured stress concentration around the critical point. This factor depends upon the geometry,

surface finish and stress gradient near the critical point.

It is easier in practice to read a vibratory stress signal on an oscilloscope from the peak-to-peak of the wave rather than its amplitude. Scope limits are, therefore, normally calculated in this manner. This peak-to-peak or double amplitude method of presenting scope limits is the reason behind the (2) in the numerator of the scope limit equation.

The scope limits for the first three modes for the Mod. II Fan C blade are shown as a function of rpm on Figure 76. The scope limits for the higher modes are beside the corresponding modes on the Campbell Diagram (Figure 78).

## 2. Clean Inlet Aeromechanical Response

With a clean inlet, the fan blade vibratory stresses are very low along the operating line. Typical blade stress as percent of scope limits are shown on Figure 77. Only a modest increase in the vibratory stresses occurs when the fan is throttled close to the operational limit line as defined on the fan compressor map. This operational limit line is where the fan either enters rotating stall or a high vibratory level of self-excited vibration is encountered. This stress condition and various other aeromechanical characteristics of the fan blades with a clean inlet are discussed in the following sections.

### a. Separated Flow Response

Separated flow response is a term to describe the vibratory response of a blade to cascade turbulent flow separation or free-stream turbulence. It usually involves the lower modes and is characterized by random vibratory amplitude with time.

Along the nominal operating line, blade vibration due to separated flow response was minimal and did not exceed about eight percent of scope limits as can be seen on Figure 77. The peaks in this curve are due to the integral per-rev response of the blades due to a modest amount of distortion found in even clean inlets.

Excluding these peaks, the remaining blade stress may be attributed to the separated flow response. Separated flow response normally increases when a fan is throttled and provides warning of impending stall. On this fan, however, the increase in the vibratory level was so slight in the low-to-medium speed range as to be a poor indication of the throttled condition. Above 85% speed, throttling did cause an increase in separated flow response, but under no circumstances did it exceed about 25% of scope limits.

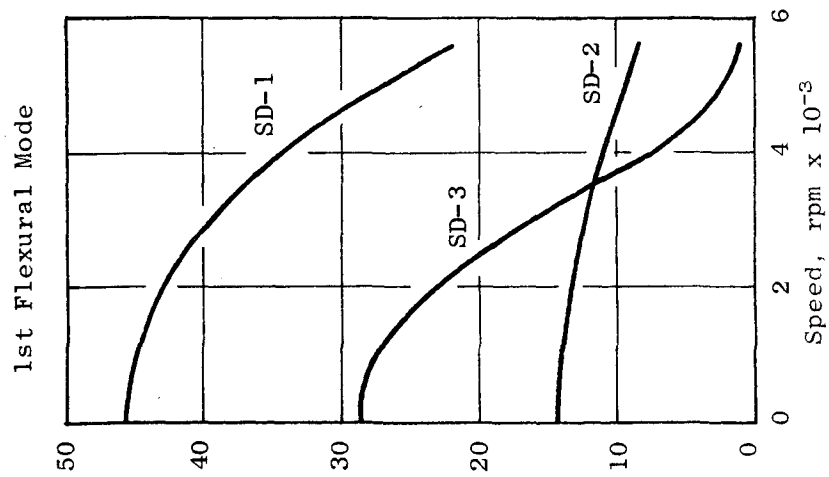
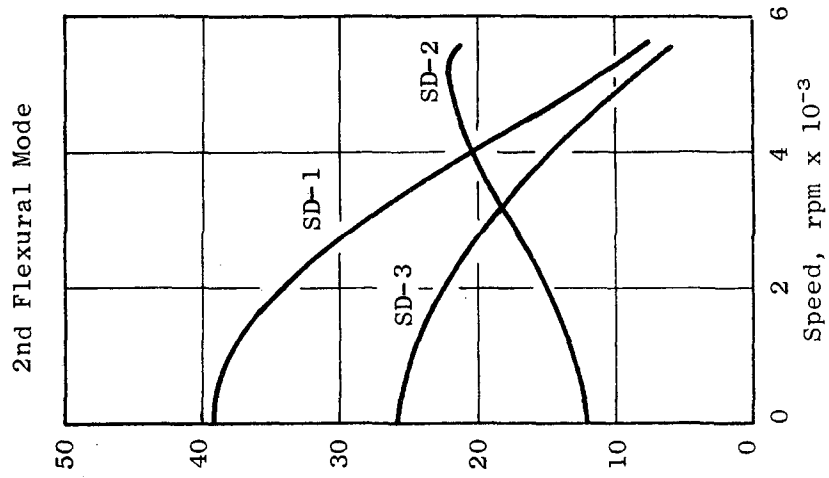
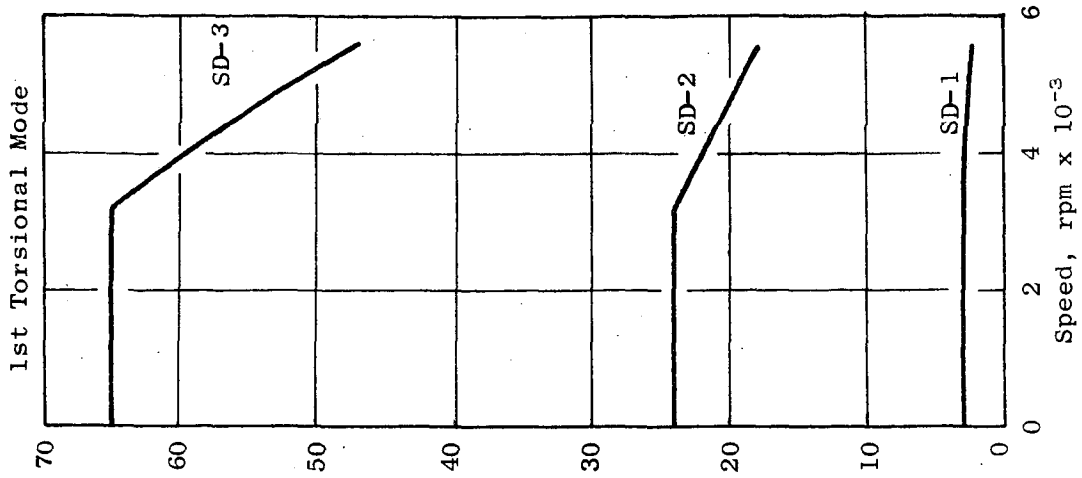


Figure 76. Mod. II Blade Scope Limits as a Function of Speed (First Three Modes).

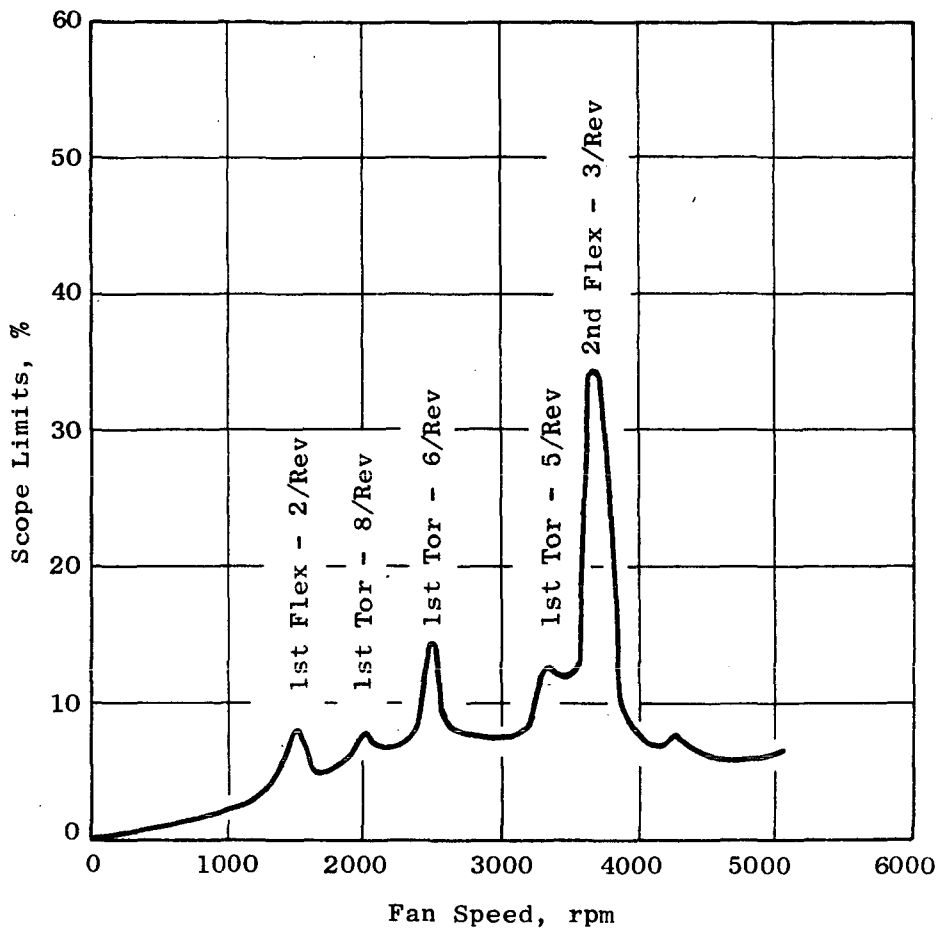


Figure 77. Mod. II Typical Vibratory Response on the Operating Line with a Clean Inlet.

b. Integral-Order Blade Response

Integral order blade response exist when a natural frequency or mode of vibration is induced to respond at an integral multiple of the rotor speed. These multiples are referred to as "per-revs" and can be predicted from the Campbell Diagram (Figure 78) where a blade natural frequency crosses each per-rev line. It is this type of blade response that produces the peaks of stress versus rotor speed as shown on Figure 77.

With a clean inlet, and in the absence of inlet guide vanes, integral order blade response never caused the rotor stresses to exceed 35% of limits. This level was approached around 3650 rpm where the second flexural blade mode is resonant with the 3 per rev. At 2600 rpm, the blade response in first torsion to 6 per rev caused stresses to reach 15% of limits. These and other lesser resonance points are labeled on the Blade Vibratory Response curve (Figure 77).

There is some evidence to suggest that the Lynn Component Test Facility, where the fan was tested, tends to induce blade response to 3 per rev and higher harmonics of this frequency. For this reason, it would not be surprising if in outdoor tests of this fan with a bellmouth inlet the blades would not reach even the modest resonance levels seen in this test.

c. Stall Response

Rotating stall was the limiting condition upon throttling up to 60% speed. It would probably be the limiting condition from 95% speed up, but the drive system of the test facility lacked sufficient power to drive the fan to stall in this high speed range. In this speed range, the fan was throttled beyond the projected stall line as far as was possible, and these power limiting points are shown on the operational limit line. Below 60% speed, the rotating stalls were very mild with stall stresses remaining below 40% of limits.

d. Self-Excited Vibration

Between 60 and 90% speed, a self-excited vibratory condition on the fan blades was the limiting condition on throttling the fan. This condition was encountered near the objective stall line of the fan. This vibration occurred at a nonintegral multiple of the rotational frequency. Between 60 and 70% speeds, this vibration occurred in the first torsional mode. It occurred in the first flexural mode between 75 and 90% speeds. Upon throttling, this vibration appeared on all the instrumented blades, at about the same time and at roughly the same maximum amplitude. Stresses would initially be low, but would increase with additional throttling. This rate of increase depended upon the speed. It was a maximum at 70% speed where with very little additional throttling after the first approach, this condition would cause the blades to approach 100% of scope limits. Since

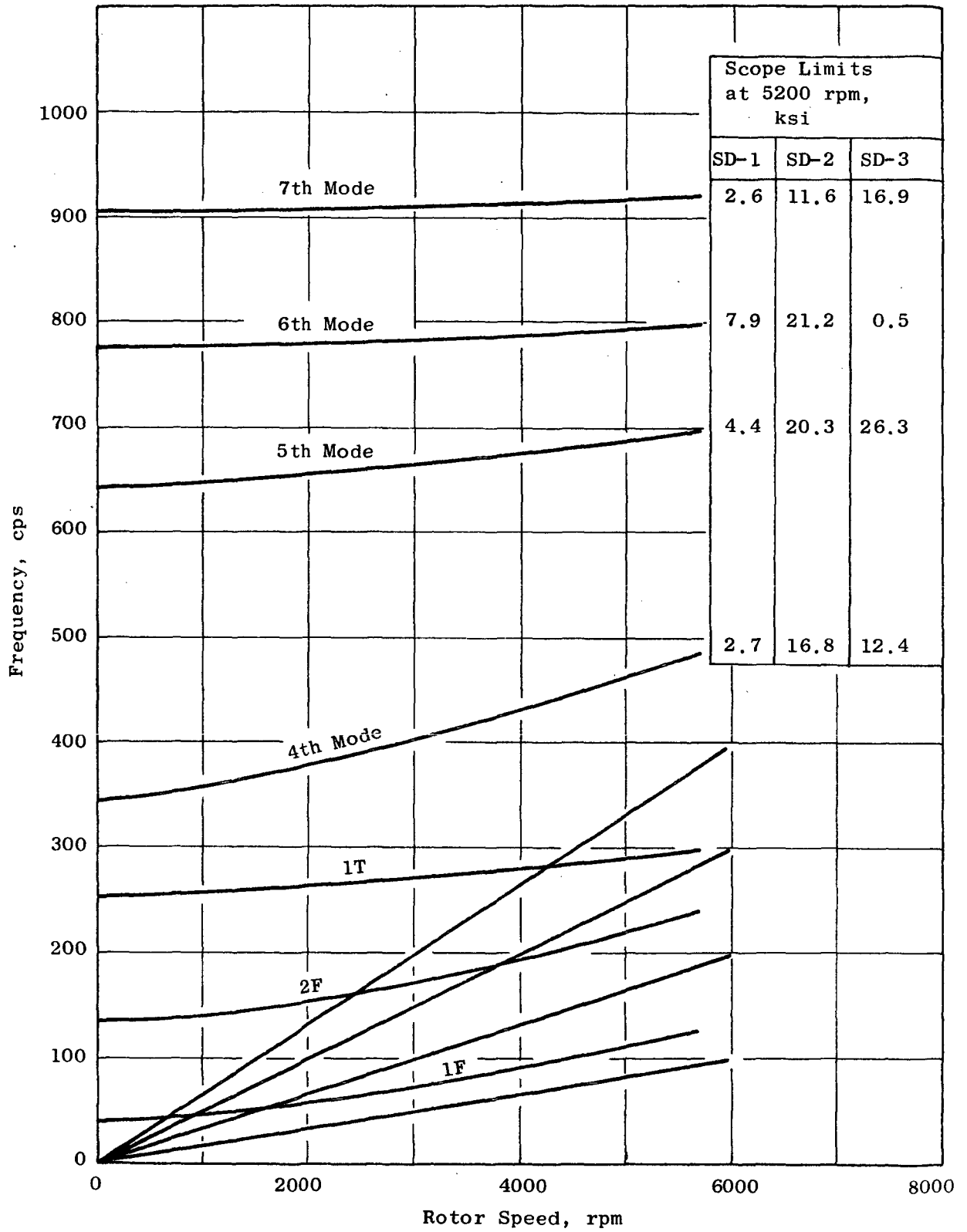


Figure 78. Mod. II Campbell Diagram.

the stress amplitude in these self-excited modes was repeatable and well behaved, the operational limit line and fan performance was mapped in this region without exceeding the blade scope limits.

### 3. Distorted Inlet Aeromechanical Response

Three distortion patterns were tested to 90% speed on Build No. 3 of the Fan C vehicle. These were a tip radial, a crosswind takeoff pattern and a one-per-rev pattern. All three patterns were design to have  $\Delta P/P_{\max}$  of about 15 % at 90% fan speed. This distortion screen for the tip radial pattern covered the outer 40% of the annulus area. The one-per-rev screen completely covered 180 degrees of the annulus area. The crosswind pattern combined many of the characteristics of the one-per-rev and the tip radial pattern. It spanned 160 degrees of the inlet, but only covered 30% of the annulus area. A solid metal plate is used in the center 45 degrees of the pattern. The screen patterns with the corresponding  $\Delta P/P_{\max}$  versus the fan weight flow are shown on Figure 79.

Only modest changes in the fan blade vibratory response due to these patterns were noted along the operating line. Specific response characteristics with these patterns are covered in the following sections:

#### a. Separated Flow Response

Along the operating line up to 90 percent speed (takeoff speed and the maximum test speed with the distortion patterns), the separated flow response increased only slightly from that noted with the clean inlet. The largest increase occurred with the one-per-rev pattern where separated flow blade response reached 12% of limits. With additional throttling even this variation from the clean inlet response lessened. Near stall, none of the patterns induced separated flow response above 25% of limits.

#### b. Integral-Order Blade Response

One would normally expect the one-per-rev and crosswind patterns to appreciably raise the integral-order vibratory response of the blades. This was not the case for this fan. Only a modest increase in resonance response was noted with any of the patterns tested. In fact, the rise in the overall blade stress level due to separated flow response made some of these resonances more difficult to detect. The maximum blade stress along the operating line was still due to the second flexural blade resonance with 3 per rev around 3650 rpm. This resonance did not exceed 50 percent of scope limits with any of the patterns.

#### c. Stall and Self-Excited Vibratory Response

The main effect of the tip radial and crosswind distortion patterns was to modify the limiting blade stress condition on throttling in the medium to

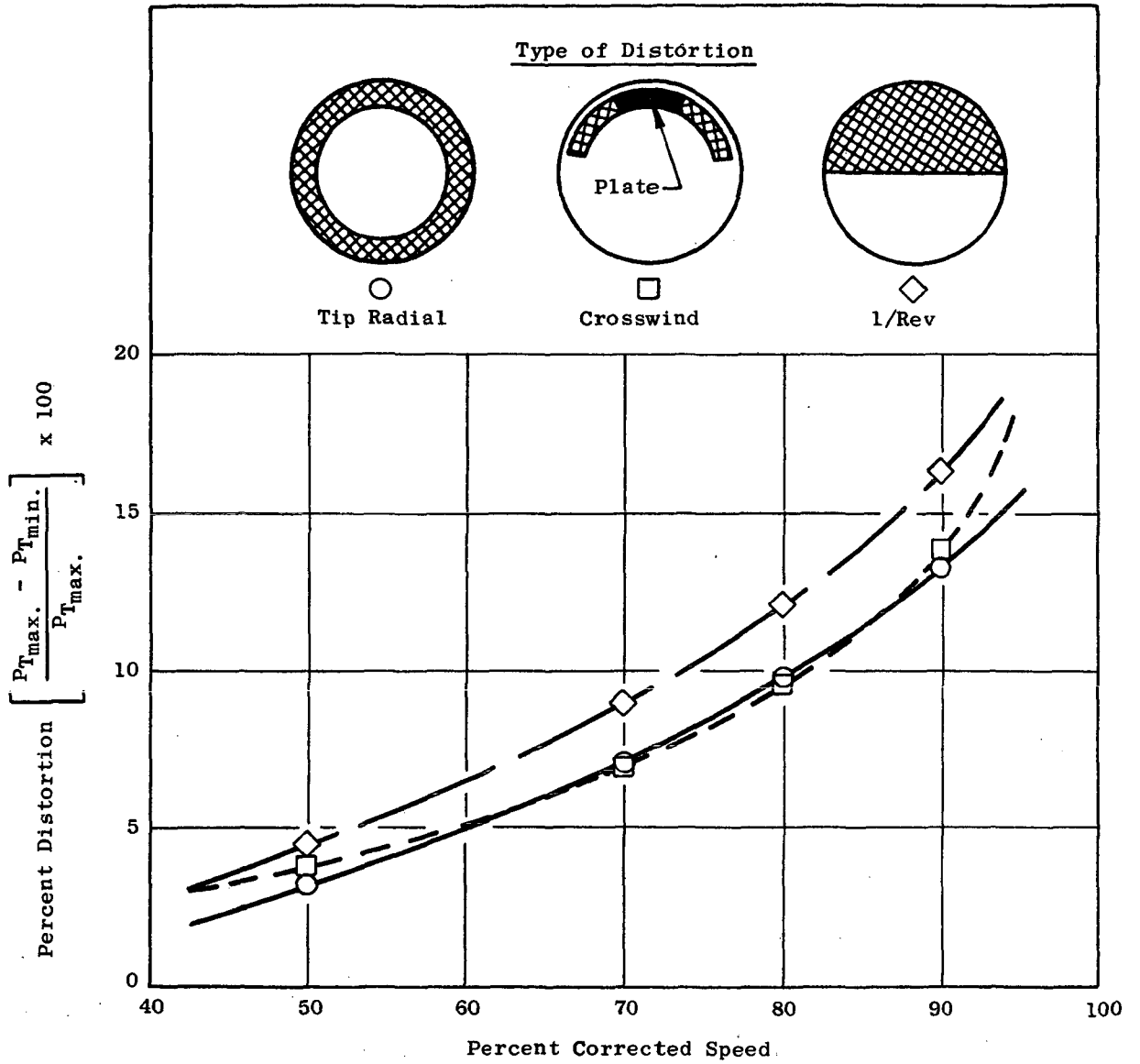


Figure 79. Inlet Distortion Magnitudes.

high speed range. With these patterns, the fan could be throttled into rotating stall at 90% speeds without being limited by self-excited vibration on the fan blades. The maximum stress the fan encountered during a rotating stall occurred at 90% speed with the tip radial distortion pattern. In this stall, the blade stress reached 94% of limits. Between 65 and 80% speeds, self-excited vibration of the blades was the limiting condition encountered upon throttling the fan with all of the inlet distortion patterns tested. Between 70 and 80% speeds, this condition was encountered in the first torsional mode. As with the clean inlet, the amplitude of the blade stress in this condition depended upon how far the fan was throttled, but would approach 100% with sufficient throttling. No problems were encountered in mapping a repeatable operational limit line for the fan map without exceeding the scope limits for the blade. A summary of the limiting condition encountered upon throttling the fan is given in Table I.

### C. CONCLUSIONS

The performance maps for the NASA Quiet Engine Mod. II Fan C were determined with a clean inlet and with three distortion patterns. An operational limit line was determined for each inlet condition. Within this limit line the fan may be successfully operated without encountering stall or excessive fan blade vibration. Specifically:

- With a clean inlet the fan blade stresses along the operating line are very low. A peak stress of 35% of limits in the second flexural mode may be expected near 3650 rpm, but the nominal blade stress is about 8% of limits.
- The fan was aeromechanically very tolerant to the types of inlet distortion patterns tested. Along the operating line, these patterns caused only a modest increase in the vibratory response of the blades. The maximum blade stress continued to occur around 3650 rpm and never exceeded 50% of limits.
- The limiting condition encountered upon throttling the fan is either rotating stall or self-excited blade vibration, depending on the fan speed and inlet condition (See Table I). When self-excited vibration occurs, it appears in the first torsion mode at low speed and in the first flexural mode at higher speeds. The limiting condition with all of the distortion patterns at "takeoff" speed (90%) was rotating stall. The fan blade stresses never exceeded 100% of limits in either a stall or in self-excited vibration.

### AEROMECHANICAL CHARACTERISTICS OF FAN C STATOR

This portion of the Appendix covers the aeromechanical characteristics of the Fan C stator vanes.

Table I. Limiting Condition Encountered Upon Throttling.

Fan Inlet Distortion Pattern	Percent Fan Speed									
	50	60	65	70	75	80	90	95		
Clean	Stall	SV-IT	---	SV-IT	SV-1F	SV-1F	SV-1F	Stall		
Tip Radial	Stall	Stall	SV-IT	SV-1F	SV-1F	SV-1F	Stall	---		
Cross Wind	Stall	---	SV-IT	SV-1F	SV-1F	SV-1F	Stall	---		
I/Rev	Stall	SV-IT	---	SV-1F	---	SV-1F	Stall	---		

SV-IT Self-Excited Blade Vibration - 1st Torsional Mode  
 SV-1F Self-Excited Blade Vibration - 1st Flexural Mode

## A. SCOPE LIMITS

### I. General Procedure

Only a limited number of so-called "engine" gage locations are utilized in monitoring the vibration characteristics of the blading in a given stage. Accordingly, it is necessary to ascertain the limiting vibratory stress (scope limit), as seen by each "engine" gage/location, for all pertinent modes of blade vibration. For this purpose, the following relation is used:

$$\sigma_{\text{scope}} = \frac{2\sigma_e (\sigma_g / \sigma_{cp})}{K_v K_e K_c}$$

where  $\sigma_{\text{scope}}$  = scope limit, Kpsi-da\*

$\sigma_e$  = endurance limit, corresponding to the steady stress, at the critical point (defined below), taken from the Goodman diagram for the proper blading material and temperature (must include three sigma reduction of average endurance limit to represent minimum material properties).

$\sigma_g / \sigma_{cp}$  = ratio of vibratory stress indicated by the "engine" gage to that at the critical point for the vibration mode under consideration.

$K_v$  = blade-to-blade response variation during vehicle operation (1.3 is normally used).

$K_e$  = electronics variation allowance (1.05 is normally used).

$K_c$  = concentration factor at the critical point (varies with local geometry).

Critical Point: Point on the blade at which initial fatigue cracks would be incurred for the vibration mode in question. Selection of the critical point for scope limit calculations is defined by the following equation:

$$\left( \frac{K_{cL}}{K_{c \max}} \right) \left( \frac{\sigma_{vL}}{\sigma_{v \max}} \right) \left( \frac{\sigma_{e \max}}{\sigma_{eL}} \right) = \text{maximum}$$

where,  $K_{cL}$  = concentration factor at location being considered on the blade.

$K_{c \max}$  = concentration factor at maximum vibratory stress point.

\* "da" is double amplitude, also referred to as peak-to-peak amplitude.

- $\sigma_{vL} / \sigma_{v \max}$  = ratio of the local vibratory stress to that at the maximum vibratory stress point on the blade in the vibration mode under consideration.
- $\sigma_{eL}$  = endurance limit at the location being considered on the blade, for the steady-state stress existing at the location, using the applicable Goodman diagram.
- $\sigma_{e \max}$  = endurance limit at the location of maximum vibratory stress on the blade for the vibration mode under consideration, using the applicable Goodman diagram.

Identification of the critical point, as well as the scope limit itself, therefore, requires a knowledge of the steady stress distribution over the entire blade/vane structure at the applicable operating conditions. Steady stress calculations utilize the General Electric "Twisted Blade" and MASS computer programs, and, for complex geometries in the vicinity of the built-in end(s) of the airfoil, stress levels are modified by the introduction of "end-effects" corrections.\* These corrections involve, first, the acquisition of measured local steady stresses throughout the critical airfoil root (and shroud,) for shrouded blades) area for known magnitudes of torsional moment, radial pull (rotor blades), and bending moment about both the tangential and axial planes. By multiplying these values of local stress per unit load (or moment) by the corresponding computed load and moments present at the airfoil root, much more accurate steady stresses are obtained in these regions.

The process of defining vibratory stress distributions for use in the derivation of scope limits is discussed separately in the scope limit section, which follows:

## 2. Frequency and Vibratory Stress Distribution

In the absence of a centrifugal field, the vane natural frequencies, and associated vibratory stress distributions, for this vehicle are essentially unaffected by operating conditions. Although it is possible to compute vane natural frequencies with reasonable accuracy for these vanes having airfoil leading and trailing edges over-hanging the round vane base, it is acknowledged that bench test vibratory stress distribution data, using a large number of miniature strain gages applied to the vane, provides the most accurate information on which to base scope limits. For these vanes, which are held at one trunnion end, the other being inserted into a hole, the degree of restraint in the engine/vehicle environment is not known exactly. Thus, vibratory stress distribution bench testing was done with the trunnion of the vane-actuation end clamped tightly, but with each of three restraint conditions for the trunnion at the other end; fixed, free, and restrained (inserted into a hole with a slightly loose fit). Testing of the fan component revealed that the vanes

---

\*Geometries requiring end-effects correction include airfoils with high airfoil twist and/or camber gradient near the root, airfoil root skew, and nonrigid or nonuniform airfoil root support.

responded as if fixed at both ends, so natural frequencies for fan bypass and core (inner) OGV's are presented in Figures 80, 81, and 82 for this trunnion fixity condition.

### 3. "Engine" Gage Selection and Scope Limits

Study of the bench vibratory stress distribution data indicated that only one engine gage location on both the bypass and core OGV's was required in order to provide adequate sensitivity to all vibration modes which could be excited up to fan blade-passing per-rev excitation at top speed. These gage locations are shown in Figures 83, 84, and 85. Limits were calculated at design speed conditions per the approach described in Section IIIA, utilizing the Goodman diagram information shown in Figure 86. These limits are inserted in Figures 80, 81, and 82 opposite the plotted natural frequencies.

## B. DISCUSSION

### 1. General Comments

This fan vehicle was tested with two basic rotor geometries, initially with mid-span shrouds, and finally as cantilevered blades. Primary emphasis with regard to stator vane aeromechanical characteristics is applied to the final configuration, although limited comparisons of stator stress with the initial fan blade geometry are included. Discussion of specific variables, which affect stator vane aeromechanics, includes:

- With clean inlet, the effect of operation along operating lines representing engine operation with each of the three fan nozzle areas ( $A_{28} = 1385, 1539, \text{ and } 1695 \text{ in.}^2$ ).
- The effect of operation with the three inlet distortion screen patterns on the nominal operating line ( $A_{28} = 1539 \text{ in.}^2$ ).
- Fan stall.

### 2. Aeromechanical Characteristics with Clean Inlet

#### a. Fan Bypass OGV's (Figure 87)

Primary response of these vanes was in the first flexural mode, mostly separated flow vibration but with modest additions of 4 and 5 per rev excitation. Response with the final fan geometry did not exceed 30% scope limits, which is considered a safe condition for endured engine operation. The influence of operation at higher pressure ratios (small fan exhaust nozzle) on vane stress was found to be modest. As indicated by the data points in Figure 87, stator vane vibratory response was very similar with

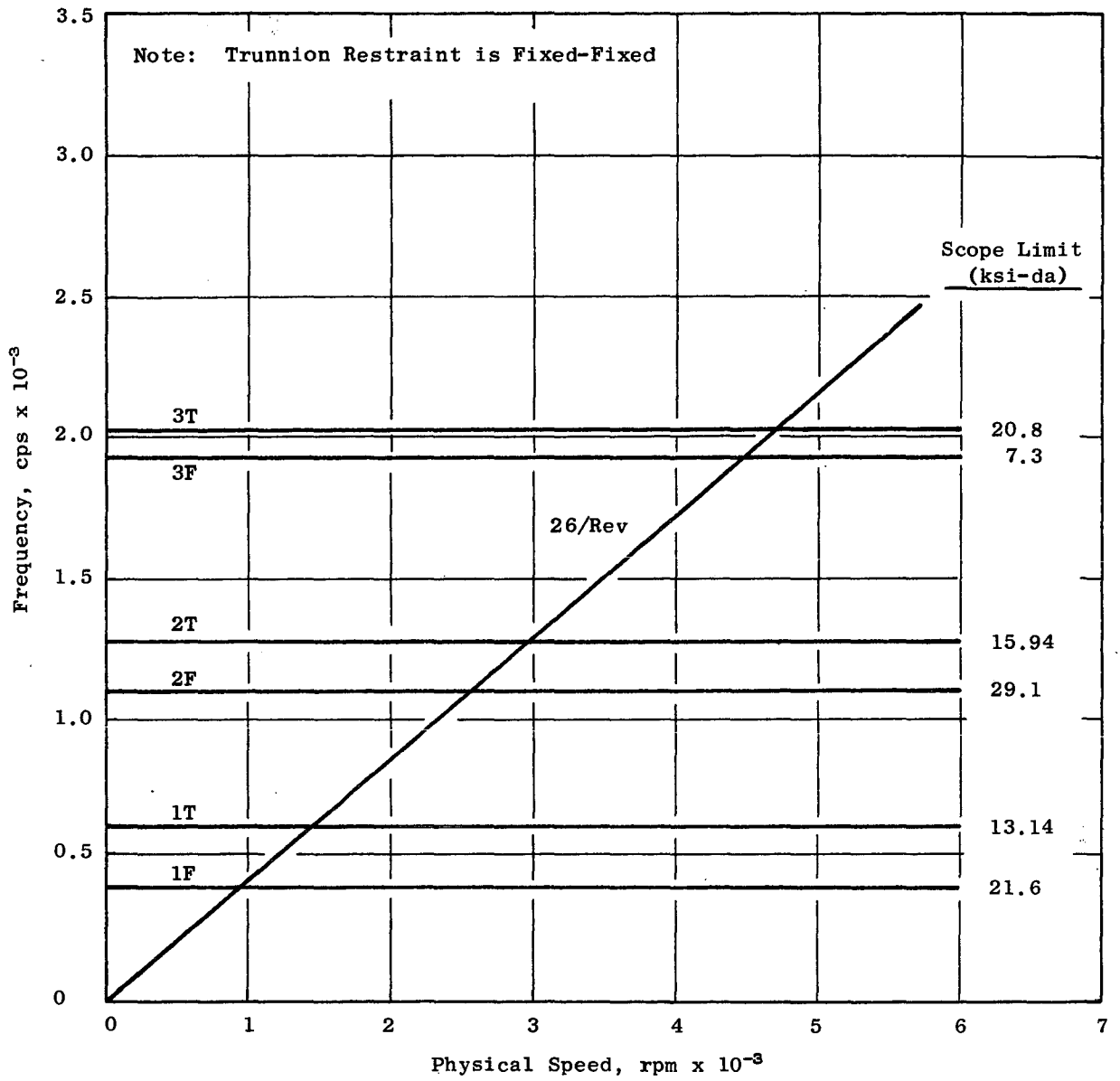


Figure 80. Campbell Diagram and Scope Limits, Bypass OGV.

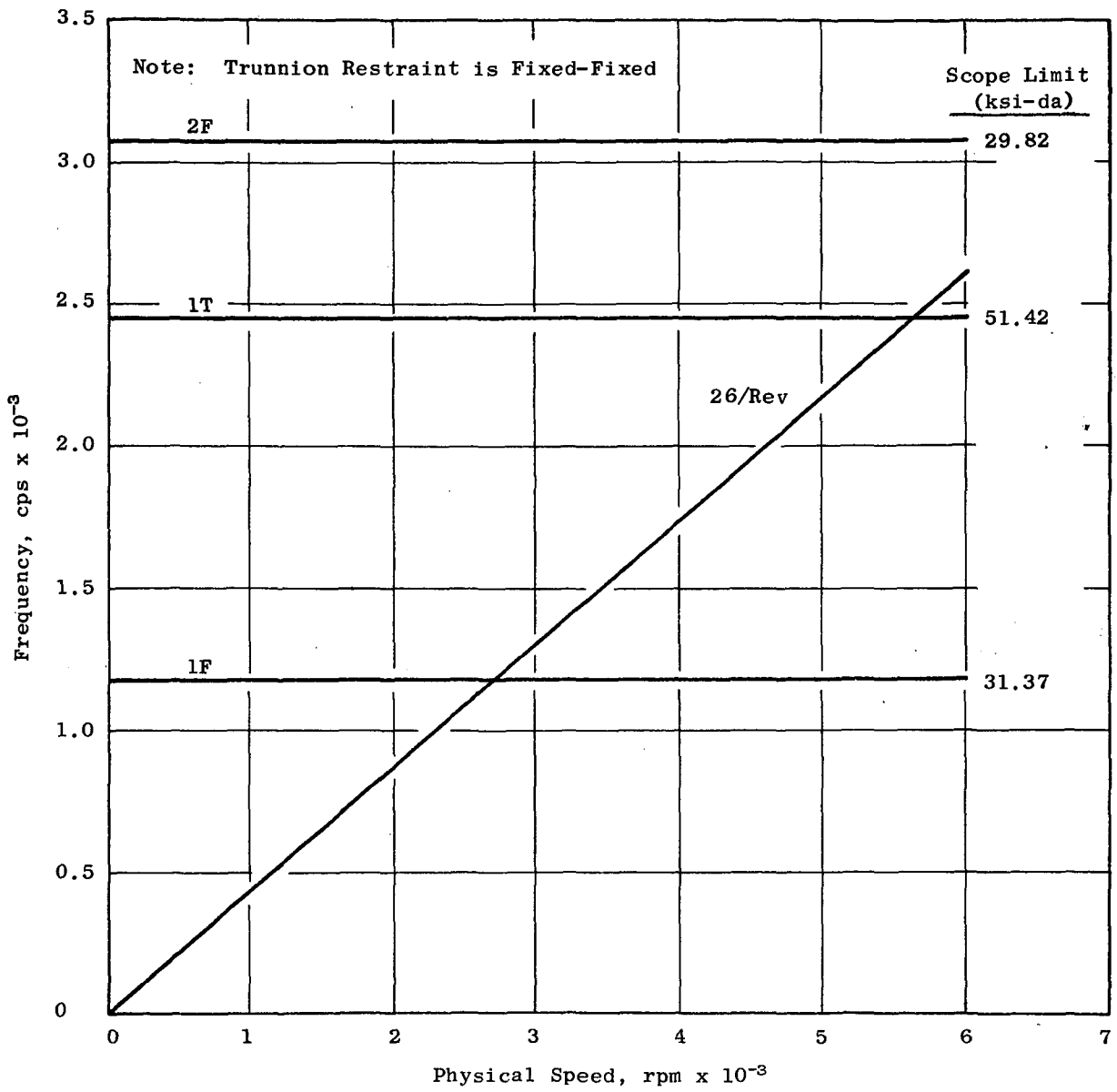


Figure 81. Campbell Diagram and Scope Limits, Forward Inner OGV.

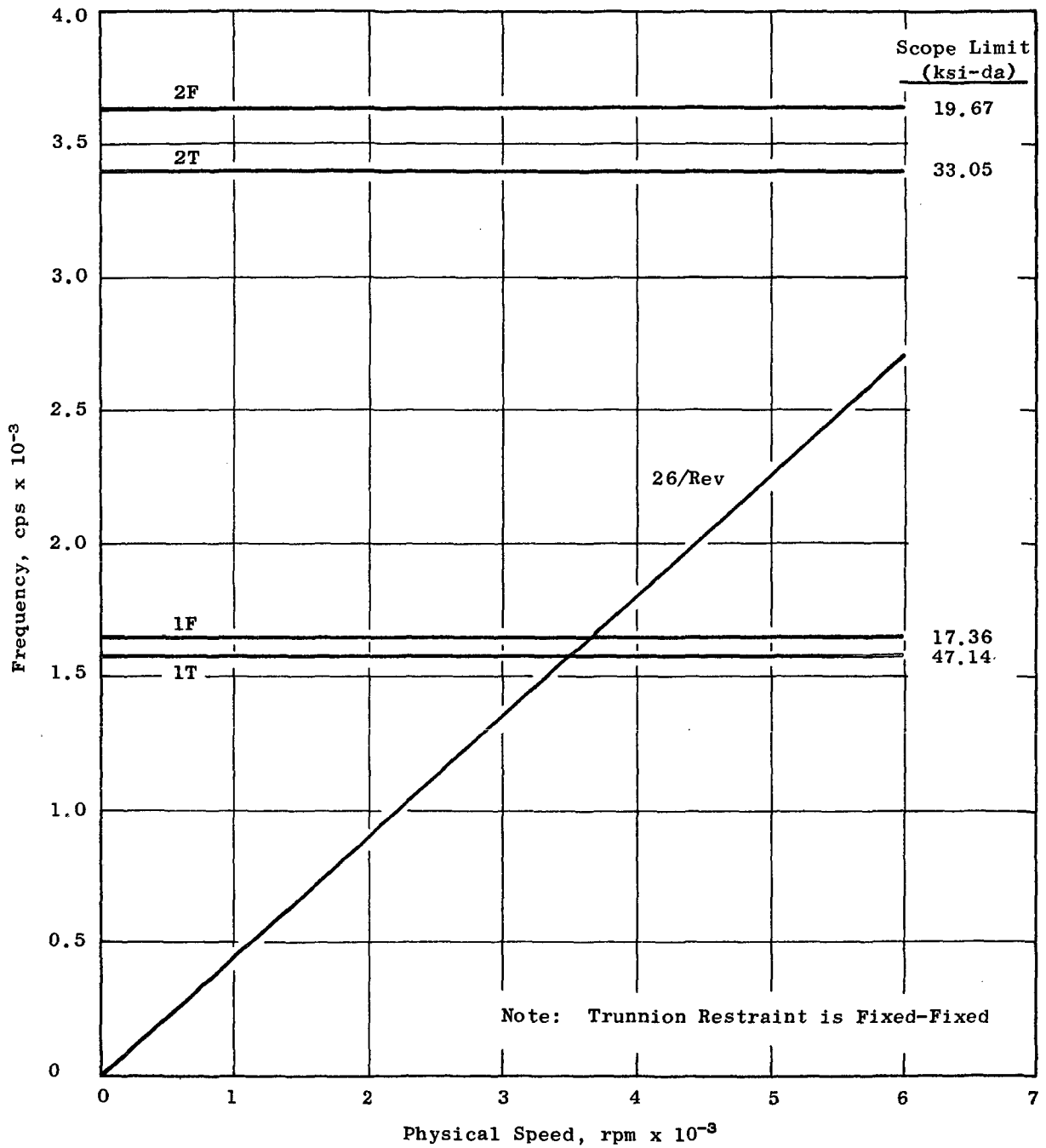


Figure 82. Campbell Diagram and Scope Limits, Aft Inner OGV.

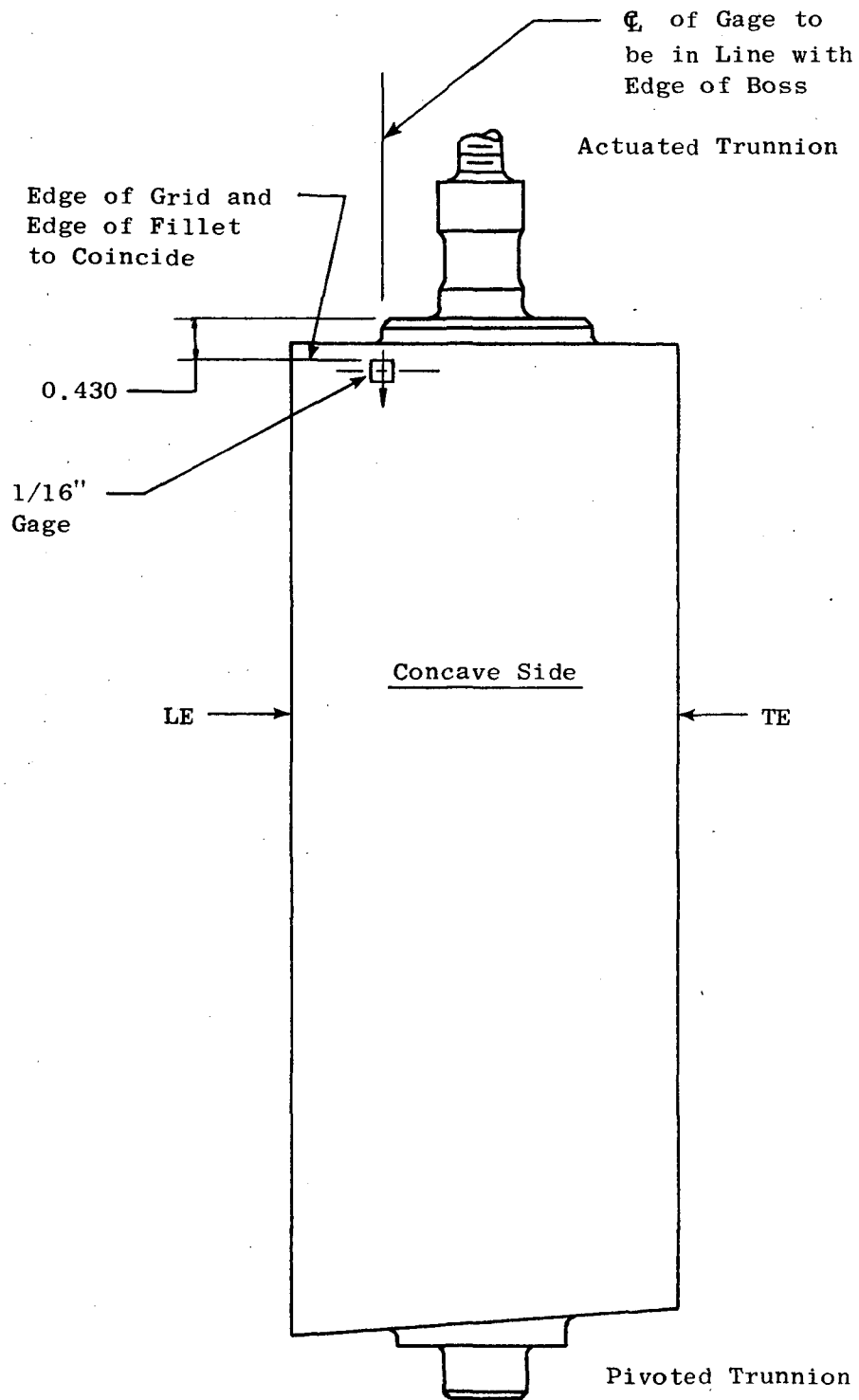


Figure 83. Bypass OGV Strain Gage Location.

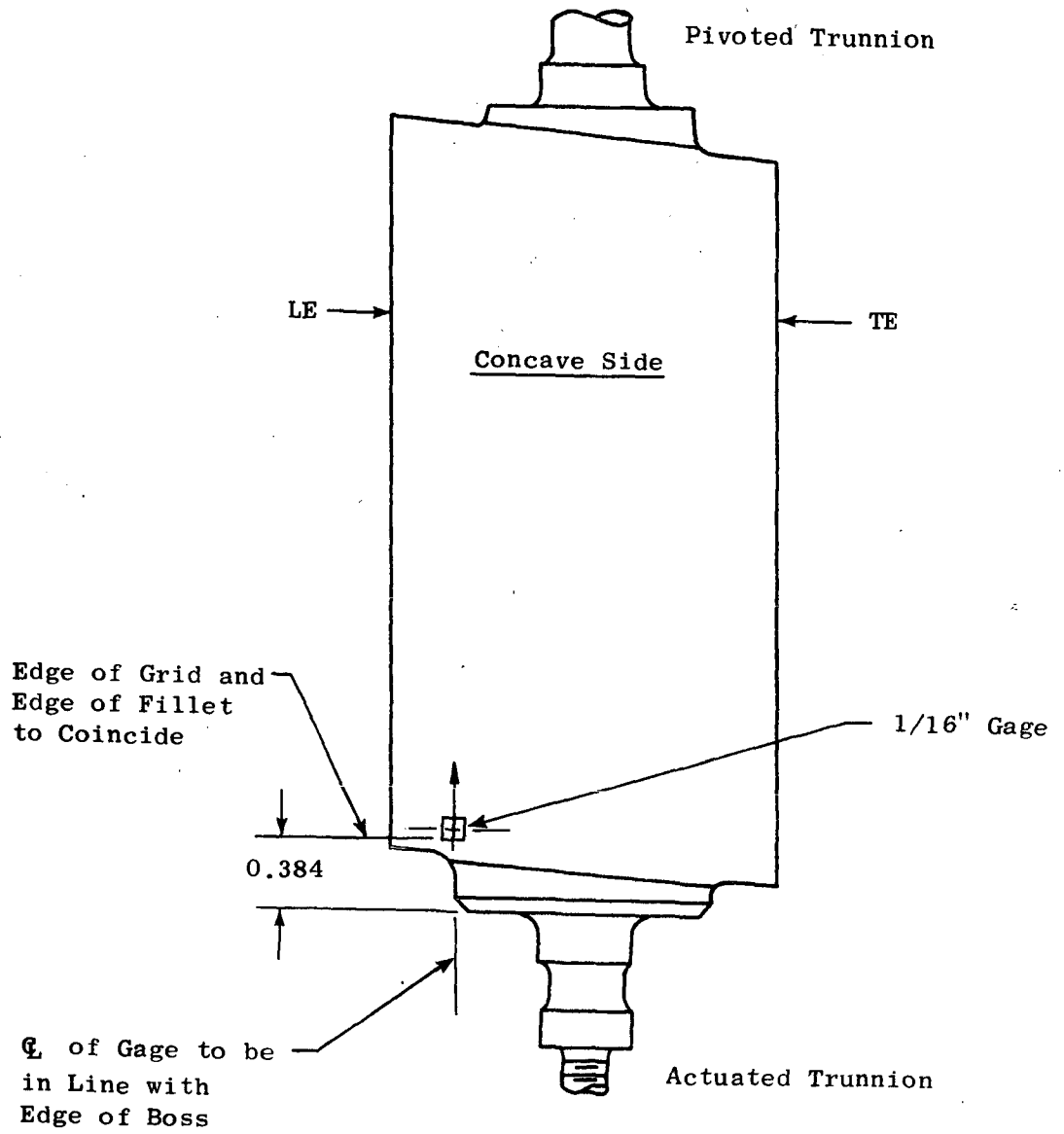


Figure 84. Forward Inner OGV Strain Gage Location.

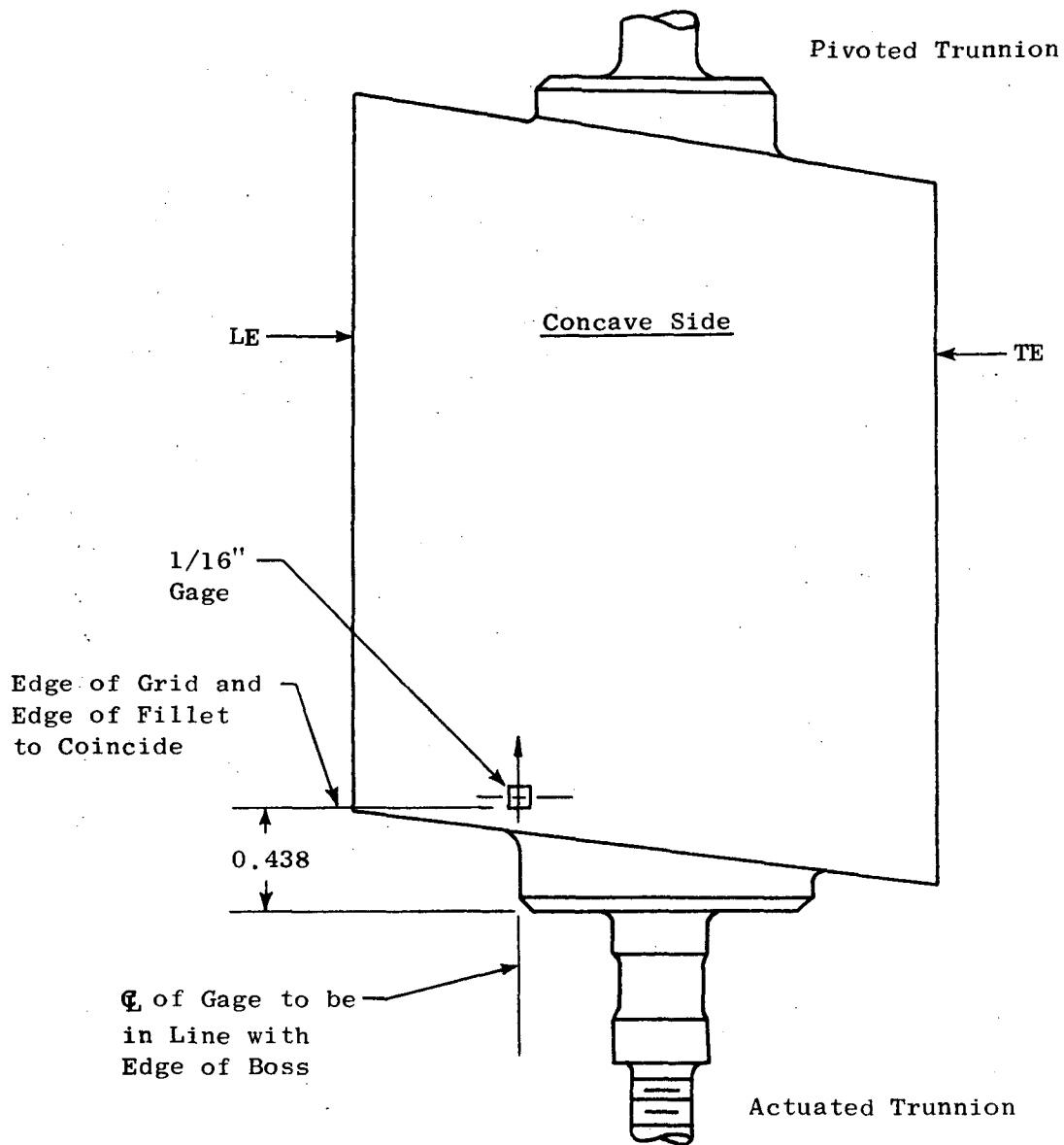


Figure 85. Aft Inner OGV Strain Gage Location.

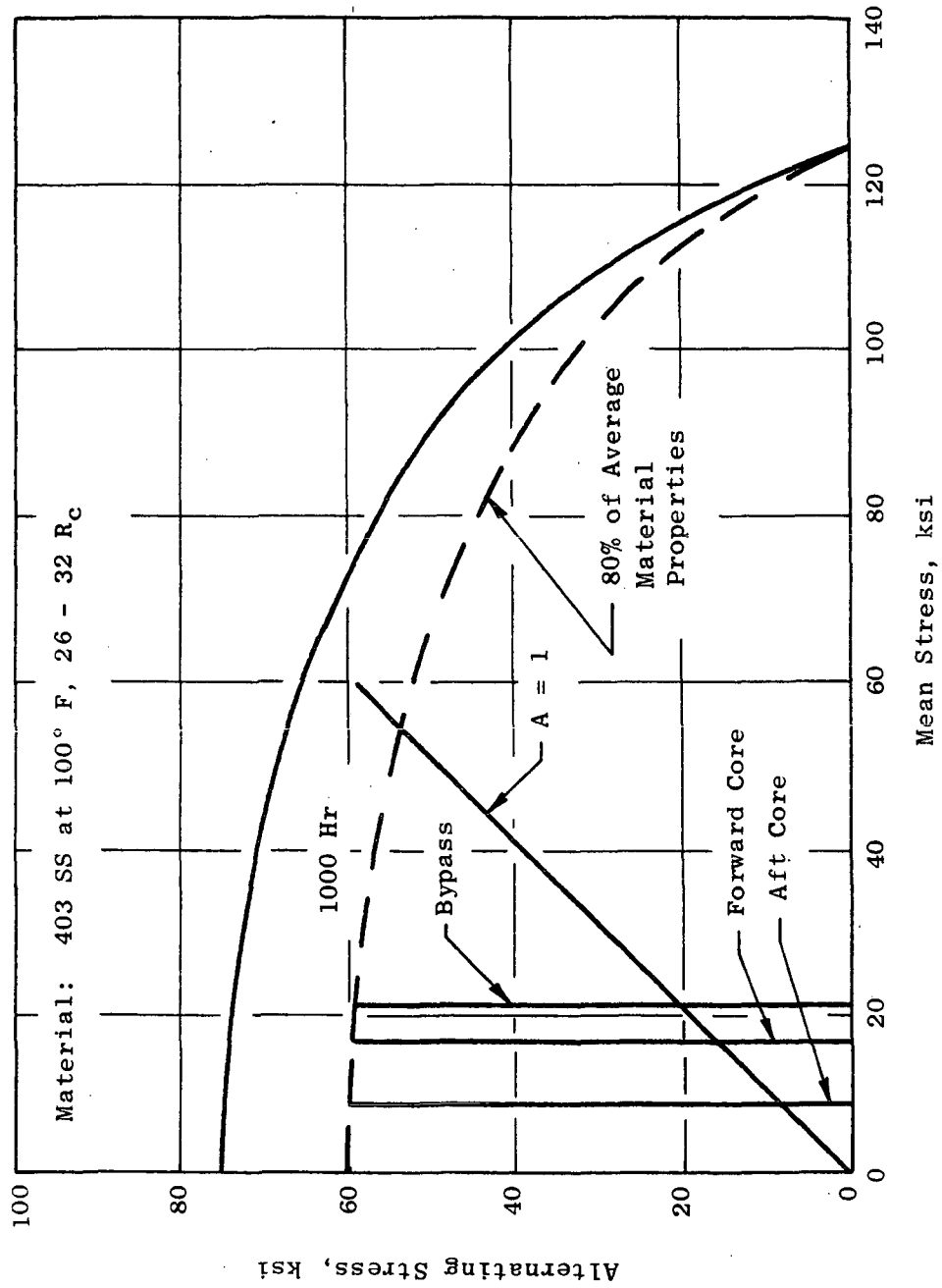


Figure 86. Goodman Diagram for Scope Limit Calculations.

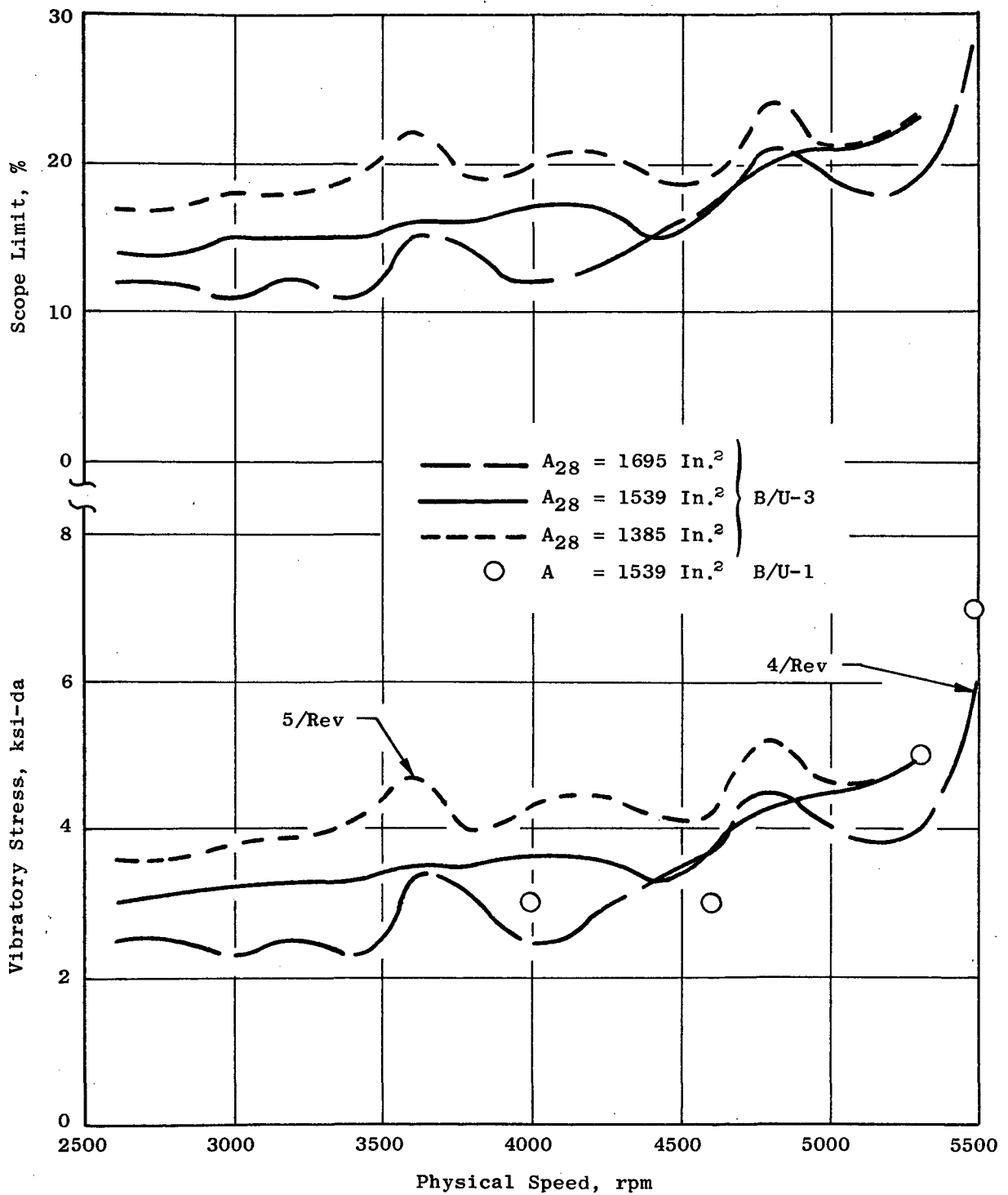


Figure 87. Bypass Stator Vane Vibration Summary with Clean Inlet.

the original midspan shrouded fan blades. These vanes are sufficiently far downstream of the fan that resonant response to blade-passing excitation of the fifth and sixth modes in the midspeed range (see Figure 80) was practically nonexistent.

The only area of severe bypass OGV vibration was experienced with higher-than-design bypass flow ratios while setting new discharge valve positions. The source of this strong separated flow vibration was probably flow separation from the core/bypass splitter lip as bypass flow was allowed to increase. This condition was carefully monitored, and stress levels were not allowed to exceed scope limits.

b. Forward Inner Stator Vanes (Figure 88)

Maximum response of these vanes did not exceed 30% scope limit, which is considered to be an adequately safe level. Primary response over most of the speed range was in separated flow vibration, involving primarily the first flexural mode, but with some contributions from first torsion in the high speed range. The absence of any significant effect of increased pressure ratio on stress levels implies that much of the turbulent excitation was from the free stream. Resonant response of these vanes to blade-passing excitation was experienced in the first torsional mode at overspeed conditions, but, as indicated above, peak stress levels remained below 30% scope limit. During testing with the original midspan shrouded blades, vane response was similar to that described above, except that 26/Rev resonance at high speeds was somewhat stronger. The reasons for this difference are not immediately apparent, but stress levels are sufficiently low to make the question academic.

c. Aft Inner Stator Vanes (Figure 89)

Maximum response of these vanes barely exceeded 20% scope limits, thus making them even safer than the forward inner stator vanes. As with the forward vanes, primary excitation was from turbulence, with separated flow vibratory response occurring mostly in the first torsional mode. However, some contributions from second torsion were also present in the high speed range. Peak stress occurred at about 3600 rpm due to the first torsional mode 26/Rev resonance (fan blade wakes). As with the other vane rows, similar vibratory stresses were obtained over the low to midspeed range with the original midspan shrouded fan blades installed. However, additional turbulent excitation of first torsional mode separated flow vibration was experienced at high speeds, reaching about 28% scope limit; still a safe operating condition, however.

3. Effect of Inlet Distortion on Aeromechanical Characteristics

a. General Comments

Inlet distortion conditions, for investigations of aerodynamic sensitivity, were simulated by inserting predetermined screen and solid plate (where necessary) segments into the inlet flow field to produce both the desired

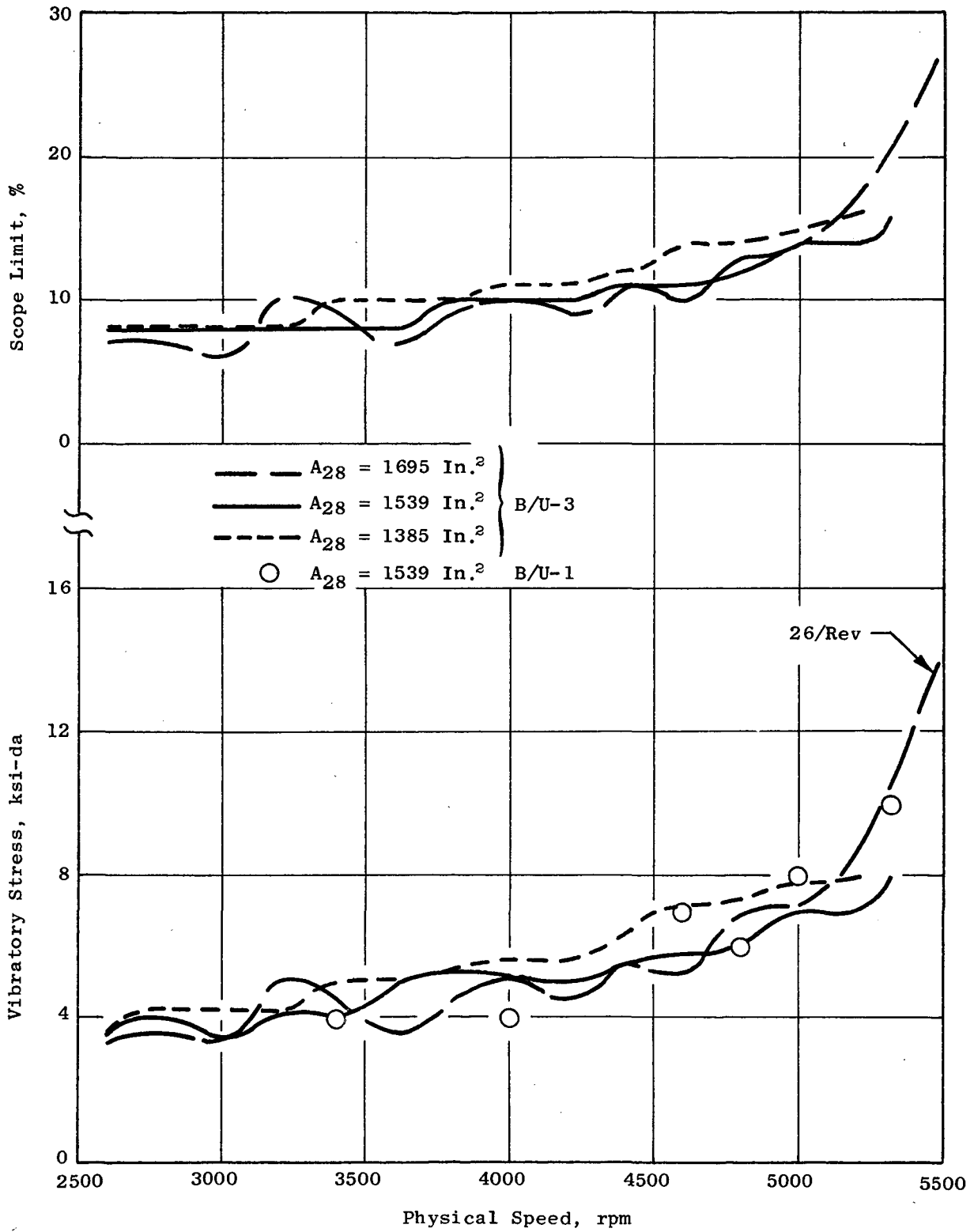


Figure 88. Forward Inner Stator Vane Vibration Summary with Clean Inlet.

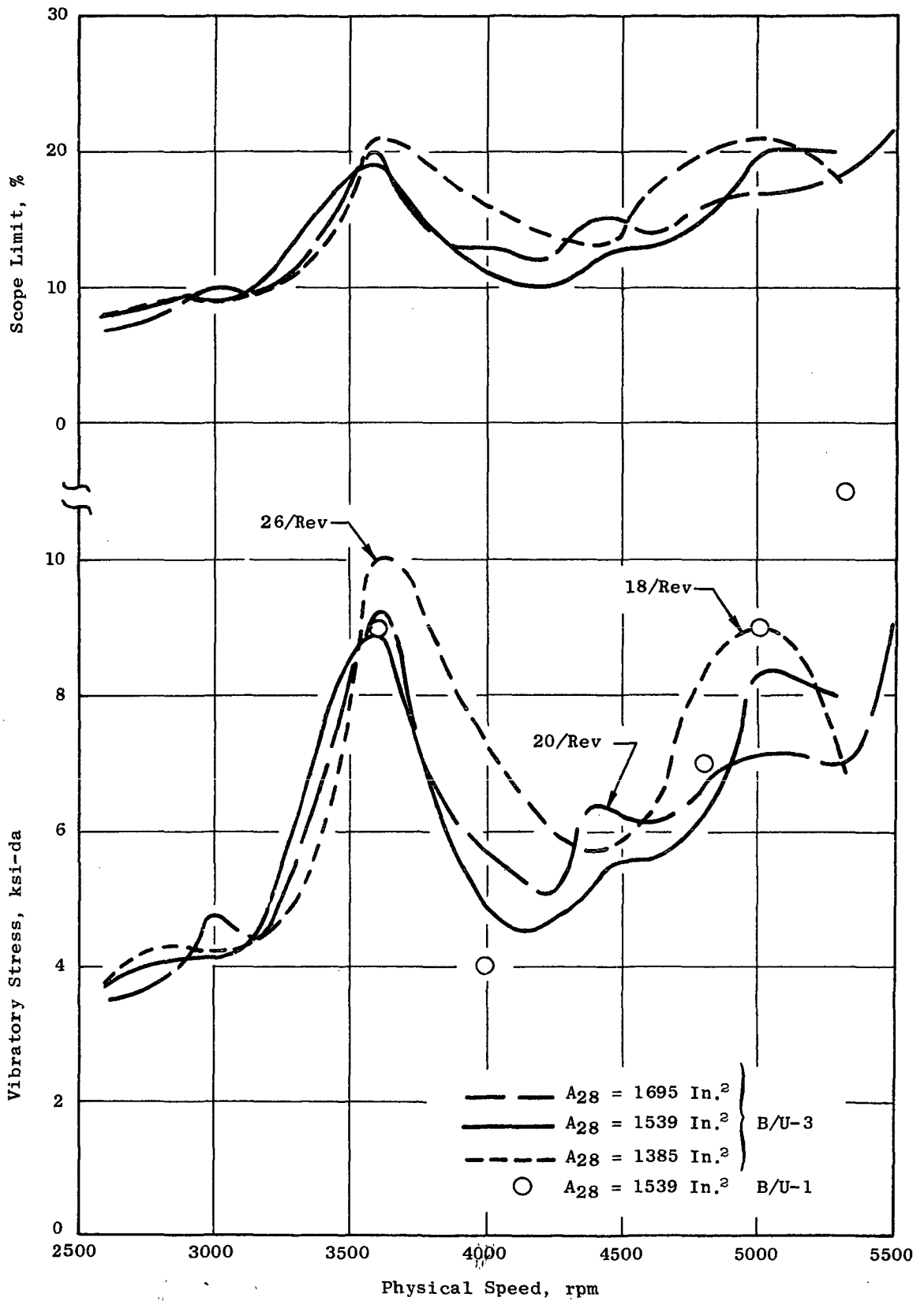


Figure 89. Aft Inner Stator Vane Vibration Summary with Clean Inlet.

patterns and magnitudes of total pressure variation entering the fan. The screen/plate patterns are shown in Figure 79, along with distortion magnitudes produced by them. From the aeromechanical standpoint, the only "real engine" excitations that are reasonably reproduced by screens are the lower-order harmonics of circumferential distortion patterns. Local velocities, vorticity levels and content are likely to deviate considerably from conditions produced by actual crosswinds with inlet lip separation, blow-in door airflow, re-ingestion during reversed thrust operation, etc. Accordingly, blade and vane aeromechanical characteristics obtained with artificially produced inlet distortion do not provide a valid indication of response magnitudes to be expected in "real life". Of course, it is necessary to monitor (and record) stresses during distortion testing as a safety precaution. The aeromechanical results of this portion of the program are discussed in the following paragraphs.

Vibratory stress information with inlet distortion is compared with corresponding data with clean inlet conditions in Table II. These stresses were recorded at constant percent corrected speeds, and thus are subject to slight inconsistencies as different physical speeds were set on different days (inlet temperature differences).

b. Fan Bypass OGV's

Increased vibratory stresses with distortion were experienced by vanes only when they were in the flow field influenced by the distortion screen segments. Highly modulated separated flow vibration was induced, with peak response reaching 74% scope limit, this with crosswind distortion. It is unlikely that actual crosswinds would generate stress levels nearly this high.

c. Forward Inner Stator Vanes

As with the bypass OGV's, only vanes located behind the inlet distortion screens were significantly affected. Separated flow vibration in combined first flexural and first torsional modes was increased markedly, but there was little increase in blade-passing excitation influencing the first torsional mode 26/Rev resonance in the 5500 rpm range (Figure 88). Excitation was not sufficiently strong to induce dangerous stress levels, the strongest being about 25% on the nominal operating line. In Table I, stress levels in the 50-80% speed range for vanes behind the distortion screen are estimated since the vanes being monitored were located near the edge of the distorted flow field.

d. Aft Inner Stator Vanes

As with the other vane rows, first torsional mode separated flow vibration of these vanes in the wake of the distortion screens was increased. In contrast to the forward inner vanes, there was a substantial increase in separated flow

Table II. Stator Vane Stress Summary\* with Inlet Distortion Screens.  
 (Nominal Operating Line: A<sub>28</sub> = 1539 In.<sup>2</sup>)

Vane Row	%Nc	Approx. rpm	Clean Inlet Stress (Ksi-da)	Tip Radial Distortion		Crosswind Distortion				1/Rev Distortion		
				ΔP/P**	Vib Stress (Ksi-da)	ΔP/P**	Behind Screen	Undisturbed Locations***	ΔP/P	Behind Screen	Undisturbed Locations***	
Fan Bypass OGV	50	2600	1	0.032	1	0.038	---	---	0.045	3	2	
	60	3100	2	0.050	1	0.050	---	---	0.065	4	2	
	70	3650	2	0.071	3	0.070	---	2	0.090	5	2	
	80	4150	2	0.098	4	0.096	---	3	0.121	7	2	
	90	4700	2	0.133	4	0.138	16	2	0.163	9	2	
Inner OGV Forward	50	2600	3	0.032	3	0.038	---	---	0.045	7(est)	2	
	60	3100	3	0.050	3	0.050	---	---	0.065	9(est)	2	
	70	3650	3	0.071	4	0.070	6	3	0.090	11(est)	2	
	80	4150	4	0.098	4	0.096	7	5	0.121	13(est)	4	
	90	4700	5	0.133	7	0.138	8	3	0.163	12	5	
Inner OGV Aft	50	2600	2	0.032	2	0.038	---	---	0.045	5	2	
	60	3100	3	0.050	3	0.050	---	---	0.065	8	2	
	70	3650	6	0.071	12	0.070	7(?)	4	0.090	17	3	
	80	4150	4	0.098	6	0.096	9	4	0.121	14	3	
	90	4700	5	0.133	10	0.138	10	5	0.163	13	5	

\* Per scope observations

\*\*  $\Delta P/P = \frac{P_{Tmax} - P_{Tmin}}{P_{Tmax}}$

\*\*\* Away from circumferential area influenced by the distortion screen.

vibration levels with tip radial distortion. Possibly the slightly increased core airflow induced by tip radial distortion simply increased the strength of free-stream turbulence to cause increased stator vane excitation. Regardless, the maximum vibratory response with any distortion was only 36% scope limits (Ref. Table II and Figure 89).

### 3. Fan Stall

With both the final cantilevered fan blades and the original midspan shrouded blades, most limiting conditions at high pressure ratios were due to fan blade self-excited vibration. The only cases of stall at high speeds were at  $90\%N/\sqrt{\theta}$ . Stator vane stresses during these stalls increased only slightly from those present during unstalled operation, never exceeding scope limits.

### C. CONCLUSIONS

Stator vane stress levels with clean inlet conditions did not exceed 30% scope limits, a magnitude considered to be adequate for endured engine operation.

During inlet distortion simulation investigations, which used screens and screen/solid plate combinations, stator vane vibration did not exceed 75% scope limits. In the presence of actual inlet distortions encountered in flight and ground crosswind conditions, it is probable that vibratory response would be much less than 75% scope limit.

Stall-induced vane vibration was minor, being excited to only slightly greater stress levels than those present prior to stall. Scope limits were not exceeded during any stall encountered.

The stators from this vehicle did not suffer any fatigue damage during this program.

LIST OF SYMBOLS

$A_t$	throttle area, nozzle throat area required to pass measured weight flow assuming isentropic expansion from measured discharge total pressure and total temperature to ambient static pressure, $ft^2$
BPR	bypass ratio
B/U	build up
$C_p$	static-pressure-rise coefficient, $\Delta p/q^*$
DV	Discharge Valve
N	rotational speed, rpm
$\bar{P}$	total pressure, psia
p	static pressure, psia
$\Delta p$	static pressure rise across OGV, psia
$q^*$	$\bar{P} - p$ , psia
R	radius, in.
$\bar{T}$	total temperature, °R
V	velocity, ft/sec
W	weight flow, lb/sec
$\alpha$	absolute air angle, degrees
$\beta$	relative air angle, degrees
$\delta$	ratio: $1 \frac{\text{total pressure}}{\text{standard pressure}} \frac{\text{psia}}{14.696 \text{ psia}}$
$\eta$	efficiency
$\theta$	ratio: $- \frac{\text{total temperature}}{\text{standard temperature}} \frac{^\circ \text{R}}{518.688^\circ \text{R}}$

$\lambda$  effective-area coefficient  
 $\psi$  stream function, percent flow passing between OD and point  
of interest,  $\psi_{OD} = 0$ ,  $\psi_{ID} = 1$   
 $\bar{\omega}$  total-pressure-loss coefficient

**Subscripts:**

Ad adiabatic  
fs free stream  
OGV outlet guide vane  
2 fan inlet  
2c fan inlet, core portion  
23 fan discharge, bypass portion  
24 fan discharge, core portion